



COOLING REQUIREMENTS
FOR THE ULTRA-COMPACT COMBUSTOR

THESIS

Donald D. Johnson, Captain, USAF

AFIT/GAE/ENY/12-M25

DEPARTMENT OF THE AIR FORCE
AIR UNIVERSITY

AIR FORCE INSTITUTE OF TECHNOLOGY

Wright-Patterson Air Force Base, Ohio

APPROVED FOR PUBLIC RELEASE; DISTRIBUTION UNLIMITED

The views expressed in this thesis are those of the author and do not reflect the official policy or position of the United States Air Force, United States Navy, Department of Defense, or the United States Government. This material is declared a work of the U.S. Government and is not subject to copyright protection in the United States.

AFIT/GAE/ENY/12-M25

COOLING REQUIREMENTS
FOR THE ULTRA-COMPACT COMBUSTOR

THESIS

Presented to the Faculty
Department of Aeronautics and Astronautics
Graduate School of Engineering and Management
Air Force Institute of Technology
Air University
Air Education and Training Command
In Partial Fulfillment of the Requirements for the
Degree of Master of Science in Aeronautical Engineering

Donald D. Johnson, B.S.
Captain, USAF

March 2012

APPROVED FOR PUBLIC RELEASE; DISTRIBUTION UNLIMITED

COOLING REQUIREMENTS
FOR THE ULTRA-COMPACT COMBUSTOR

Donald D. Johnson, B.S.
Captain, USAF

Approved:

Dr. Marc Polanka

Dr. Marc Polanka, PhD (Chairman)

3-8-12

date

Andrew Lofthouse

Maj. Andrew Lofthouse, PhD (Member)

3/8/12

date

Paul King

Dr. Paul King, PhD (Member)

9 Mar 12

date

Abstract

Over the past several years, AFIT and the Air Force Research Laboratory have collaboratively investigated a novel combustor system that is compact in design and could be potentially used as an inter-turbine burner system. The UCC attempts to wrap the combustion section circumferentially around the axial core flow and exploits the use of high-g combustion. As a result, the combustor volume and weight is reduced by integrating of the exit compressor vane and the turbine inlet vane. This creates a new hybrid vane that resides directly below the circumferential combustor. Most recently, a computational effort on understanding the fundamental aspects of the UCC on a fighter-sized scale model reveal that high temperatures are predicted to occur on the hybrid vane. To address this issue, film-cooling application is being explored in the UCC in a computational manner. The application of normal coolant hole, contoured trench, and hybrid normal and contoured trench configurations were investigated for a blowing ratio of $M=1$, 1.5 and 2. Of the blowing ratios studied, secondary reactions form due to the oxygen-rich coolant air reacting with unburned fuel as it exits the circumferential cavity. Although these reactions do occur, a decrease in unburned radicals is noticed at the exit of the UCC due to enhanced completion of reactions upstream.

Acknowledgements

During my time at AFIT, I would like thank my advisor, Dr. Marc Polanka, for his guidance and patience. The expert advice and additional hours spent on how to organize my research were invaluable and greatly appreciated. I would like to thank Dr. Joseph Zelina of AFRL/RZ for sponsoring my research. I am also grateful for the help of Dr. Hugh Thornburg for his helpful advice in running my CFD simulations. I have benefited greatly from the many helpful discussions. In addition, I am very thankful for the technical assistance of Mr. Dave Doak and greatly appreciate his support, which was vital to the success of this work.

I would like to thank my wife who has been the biggest cheerleader every step of the way through AFIT. She has encouraged, motivated and celebrated with me my frustrations and successes. She and my newborn son helped me remain sane throughout this experience and I would like to thank them for helping me always remember that which is most important.

Finally, I would like to thank the Almighty for His many blessings that have allowed me to accomplish this work as well as enjoy my AFIT journey.

Donald D. Johnson

Table of Contents

	Page
Abstract	iv
Acknowledgements	v
List of Figures	viii
List of Tables	xv
I. Introduction	1
1.1 Background	1
1.2 Motivation	2
1.3 Thesis Scope	4
II. Background	5
2.1 Centrifugal Force Combustion	5
2.2 Inter-turbine Burner	7
2.3 Computational Work on Ultra-Compact Combustor	7
2.4 Film-Cooling Background	11
2.4.1 Fluid Mechanics	13
2.4.2 Hole Geometry	16
2.5 Concerns of Heat Release Effects	18
III. Methodology	22
3.1 Research Objectives	22
3.2 Computational Setup	23
3.2.1 Turbulence Comparison Study	23
3.2.2 Chemistry Modeling	25
3.2.3 Solution Starting Sequence	27
3.3 Computational Domain	28
3.3.1 Boundary Conditions	28
3.3.2 Grid Construction	33
3.3.3 Grid Quality	33
3.3.4 Grid Convergence and Independence Analysis	34
3.4 UCC Geometry	36
3.4.1 Film-Cooling Geometry	38
3.5 Coolant Hole Geometry	38
3.6 Test Conditions	43

	Page
IV. Results	45
4.1 Baseline Model	45
4.2 Contoured Trench Results	48
4.2.1 Internal Flow Interactions	48
4.2.2 Temperature Distribution	55
4.2.3 Exit Conditions	65
4.3 Normal Hole Results	73
4.3.1 Internal Flow Interactions	73
4.3.2 Temperature Distribution	78
4.3.3 Exit Conditions	84
4.4 Hybrid Geometry Results	92
4.4.1 Internal Flow Interactions	92
4.4.2 Temperature Distribution	96
4.4.3 Exit Conditions	99
V. Conclusions	107
5.1 Overview	107
5.2 Major Findings	107
5.3 Future Recommended Work	108
Appendix A. Rayleigh Study	110
A.1 Rayleigh Geometry	110
A.2 Computational Setup	112
A.2.1 Numerical Results	113
A.3 Summary	122
Appendix B. Additional Numerical Analysis Results	123
B.1 Coolant, Cavity and Core Flow Interactions	123
Bibliography	128
Vita	131

List of Figures

Figure		Page
1.1.	History of Turbine Inlet Temperature & Material Use In Aircraft Engines [3]	2
2.1.	Flame Propagation where (left) bubble velocity is greater than the turbulent flame speed, and (right) bubble velocity is lower than the turbulent flame speed [20]	6
2.2.	Flame stability range created by Zelina et al for equivalence ratio at blowout with respect to g-loading [31]	6
2.3.	Radial Vane Cavity Configuration Schematic with Vane Cavity (right) and without Vane Cavity (left) [28]	8
2.4.	Two-Dimensional View of Radial Vane Cavity Test Configurations Looking Upstream [28]	9
2.5.	Spanwise Temperature Averages at UCC Exit of Thornburg et al. for Suction-Side Clockwise and Counter-clockwise Rotation (SS-CW and SS-CCW), Pressure-side Clockwise and Counter Clockwise Rotation (PS-CW and PS-CCW) [28]	9
2.6.	UCC geometry studied by Bohan [6] a) annular view of UCC geometry b) 2-D cross-sectional view (cm)	11
2.7.	Predicted Temperature Distribution for 20 Hybrid-Vane UCC Configuration done by Bohan [6]	12
2.8.	Typical schematic of turbine airfoil geometry [5]	12
2.9.	Influence of Blowing Ratios for a Row of Holes [14]	14
2.10.	Standard coolant hole geometries [5]	16
2.11.	Progression of continued heat release within a turbine [18] . . .	19
2.12.	Experimental results of Polanka et al. [24] for an angled hole geometry, $\phi = 1.5$	20
2.13.	Mesh view of circular normal hole, angled circular hole and fan-shaped hole studied by Thornburg et al [29]	21

Figure		Page
2.14.	Computational Results of Heat Release Study by Thornburg et al [29] at midplane: a,c,e) N ₂ Coolant and b, d, f) Air Coolant, $\phi = 1.5$, M=1	21
3.1.	Computational schematic of turbulence test	24
3.2.	Temperature Contours of Turbulence Comparison Study for $\phi = 0.95$, M=1: a) RNG k- ϵ Model, b) SST k- ω Model, and c) Result of Polanka et al [24]	25
3.3.	Temperature contour plots of Baseline geometry with non-extended (top) and extended Domaine (bottom)	30
3.4.	Flow Direction within Circumferential Cavity	31
3.5.	Sectional layout of periodic domain with respect to UCC annulus	32
3.6.	Computational Boundary Conditions for UCC	32
3.7.	Grid independence analysis (total temperature value versus grid size variation)	35
3.8.	Grid independence analysis (total pressure value versus grid size variation)	35
3.9.	Hybrid vane design	37
3.10.	Geometric layout of the Ultra-Compact Combustor in x-y plane	38
3.11.	Schematic of normal hole coolant scheme along suction side surface of vane	39
3.12.	Schematic of contoured trench with discrete hole coolant scheme along suction side surface of vane	41
3.13.	Schematic of hybrid coolant configuration along suction side surface of vane	41
3.14.	Two-dimensional view of coolant hole configurations for a) normal hole, b) contoured trench with discrete holes and c) hybrid geometry	42
4.1.	Total temperature prediction on Hybrid Vane	46
4.2.	Radial temperature distribution through UCC	47
4.3.	Streamline vortices formation from cavity section into core flow	47

Figure		Page
4.4.	Side view of coolant migration out of trench 1 for M=1 (white), M=1.5 (red) and M=2(purple)	49
4.5.	Isometric view of coolant migration out of trench 1 for M=1 (white), M=1.5 (red) and M=2(purple)	50
4.6.	Coolant migration for M=1, M=1.5 and M=2 (isometric view)	51
4.7.	Coolant migration for M=1, M=1.5 and M=2 (side view) . . .	51
4.8.	Streamline patterns of cavity flow (purple) and 2nd row coolant flow (temperature scale)	52
4.9.	Streamline view of cavity and coolant flow interaction for M=1	53
4.10.	Streamline view of core, cavity and coolant fluid interacting as they convect downstream for M=1	54
4.11.	Airfoil temperature distribution for Contoured Trench Design (M=1)	55
4.12.	Airfoil temperature distribution for Contoured Trench Design (M=1.5)	56
4.13.	Airfoil temperature distribution for Contoured Trench Design (M=2)	56
4.14.	Airfoil temperature distribution for Contoured Trench Design (M=2) using N ₂ coolant	57
4.15.	Radial temperature distribution for Contoured Trench Design (M=1)	58
4.16.	Radial temperature distribution for Contoured Trench Design (M=1.5)	59
4.17.	Radial temperature distribution for Contoured Trench Design (M=2)	59
4.18.	Spanwise Temperature of Baseline, 75% Span	60
4.19.	Spanwise Temperature of Baseline, 50% Span	61
4.20.	Spanwise Temperature of Baseline, 30% Span	61
4.21.	Spanwise Temperature of Baseline and Trench Design (M=1 case)	63
4.22.	Spanwise Temperature of Contoured Trench for M=1.5 case (left column) and M=2 (right column)	64

Figure		Page
4.23.	Spanwise-averaged temperature at UCC exit of the contoured trench design	65
4.24.	UCC Exit Temperature Contour M=1	66
4.25.	UCC Exit Temperature Contour M=1.5	66
4.26.	UCC Exit Temperature Contour M=2	67
4.27.	Spanwise average C_3H_8 concentration at location D (150D) . .	68
4.28.	Spanwise average C_3H_8 concentration at location E (200D) . .	69
4.29.	Spanwise average C_3H_8 concentration at UCC exit	69
4.30.	Spanwise average CO concentration at location D (150D) . . .	70
4.31.	Spanwise average CO concentration at location E (200D) . . .	70
4.32.	Spanwise average CO concentration at UCC exit	71
4.33.	Spanwise average CO_2 concentration at location D (150D) . . .	71
4.34.	Spanwise average CO_2 concentration at location E (200D) . . .	72
4.35.	Spanwise average CO_2 concentration at UCC exit	72
4.36.	Coolant migration out of row 1 for M=1 (white), M=1.5 (red) and M=2 (purple), (isometric view)	74
4.37.	Coolant migration out of row 1 for M=1 (white), M=1.5 (red) and M=2 (purple), (side view)	74
4.38.	Normal hole coolant interaction plotted against velocity vectors	75
4.39.	Coolant migration of row 2 for M=1, M=1.5 and M=2 a) iso-metric view b) upstream view	76
4.40.	Cavity and coolant flow interaction for normal hole geometry, M=1.5 case	77
4.41.	Airfoil temperature distribution for normal hole design (M=1) .	78
4.42.	Airfoil temperature distribution for normal hole design (M=1.5)	79
4.43.	Airfoil temperature distribution for normal hole design (M=2) .	79
4.44.	Radial temperature distribution for normal hole design (M=1)	80
4.45.	Radial temperature distribution for normal hole design (M=1.5)	80
4.46.	Radial temperature distribution for normal hole design (M=2)	81

Figure		Page
4.47.	Spanwise temperature of baseline (left column) and normal hole design M=1 case (right column)	82
4.48.	Spanwise temperature of normal hole for M=1.5 case (left column) and M=2 (right column)	83
4.49.	Spanwise averaged temperature distribution at UCC exit . . .	84
4.50.	UCC exit temperature contour M=1	85
4.51.	UCC exit temperature contour M=1.5	86
4.52.	UCC exit temperature contour M=2	87
4.53.	Spanwise-average C_3H_8 concentration at location D (150D) . .	87
4.54.	Spanwise-average C_3H_8 concentration at location E (200D) . .	88
4.55.	Spanwise-average C_3H_8 concentration at UCC exit	88
4.56.	Spanwise-average CO concentration at location D (150D) . . .	89
4.57.	Spanwise-average CO concentration at location E (200D) . . .	89
4.58.	Spanwise-average CO concentration at UCC exit	90
4.59.	Spanwise-average CO_2 concentration at location D (150D) . . .	90
4.60.	Spanwise-average CO_2 concentration at location E (200D) . . .	91
4.61.	Spanwise-average CO_2 concentration at UCC exit	91
4.62.	Hybrid geometry layout set against baseline temperature predictions	92
4.63.	Hybrid geometry trench 1 coolant flow separation (pink) from vane surface, M=2	93
4.64.	Coolant and cavity flow interaction for Hybrid coolant geometry, M=2 Case	94
4.65.	Side profile of cavity vortex forming along the suction side surface for Hybrid coolant geometry, M=2 Case	95
4.66.	Temperature colored streamline out of the cavity interacting with coolant	95
4.67.	Hybrid geometry temperature distribution, M=2	96
4.68.	Hybrid geometry radial temperature distribution, M=2	97

Figure		Page
4.69.	Spanwise temperature of baseline (left column) and Hybrid geometry M=2 case (right column)	98
4.70.	Spanwise-temperature average at UCC exit for Hybrid geometry, M=2	100
4.71.	UCC exit temperature contour for Hybrid geometry, M=2 . . .	101
4.72.	Spanwise-average C_3H_8 concentration at location D (150D) . .	102
4.73.	Spanwise-average C_3H_8 concentration at location E (200D) . .	102
4.74.	Spanwise-average C_3H_8 concentration at UCC exit	103
4.75.	Spanwise-average CO concentration at location D (150D) . . .	103
4.76.	Spanwise-average CO concentration at location E (200D) . . .	104
4.77.	Spanwise-average CO concentration at UCC exit	104
4.78.	Spanwise-average CO_2 concentration at location D (150D) . . .	105
4.79.	Spanwise-average CO_2 concentration at location E (200D) . . .	105
4.80.	Spanwise-average CO_2 concentration at UCC exit	106
A.1.	Endwall dimensions of UCC Rayleigh study	112
A.2.	Schematic layout of Rayleigh geometry	113
A.3.	Velocity vector of leading edge circulation within Rayleigh geometry	114
A.4.	Recirculation formation near lower endwall within Rayleigh geometry	115
A.5.	Streamline view of recirculation formation near lower endwall within Rayleigh geometry	115
A.6.	Streamline view of cavity and core flow interaction	116
A.7.	Temperature contour planes through the UCC for Rayleigh geometry	117
A.8.	Total temperature and total pressure area-average values of Rayleigh geometry study	118
A.9.	Total temperature and total pressure area-average values of Rayleigh geometry only	119
A.10.	Mach distribution for Rayleigh geometry	120

Figure		Page
A.11.	Swirl angle angle value through Rayleigh geometry	121
B.1.	Contoured trench fluid interaction of cavity fluid (red stream- line), coolant fluid (blue streamline) and core fluid (green stream- line) for M=1 test case	123
B.2.	Top down view of fluid interaction of cavity fluid (red streamline), coolant fluid (blue streamline) and core fluid (green streamline) for Contoured Trench design (M=1 test case)	124
B.3.	Top down view of fluid interaction of cavity fluid (red streamline), coolant fluid (blue streamline) and core fluid (green streamline) for normal hole geometry design (M=1 test case)	125
B.4.	Hybrid geometry fluid interaction of cavity fluid (red streamline), coolant fluid (blue streamline) and core fluid (green streamline) for M=2 test case	126
B.5.	Top down view of fluid interaction of cavity fluid (red streamline), coolant fluid (blue streamline) and core fluid (green streamline) for Hybrid geometry design (M=2 test case)	127

List of Tables

Table		Page
2.1.	17 Factors Impacting Film-Cooling Performance [5]	13
3.1.	Fluent [®] turbulence test conditions	24
3.2.	Species Mass Fraction Input Values	24
3.3.	Fluent [®] Boundary Condition Inputs	31
3.4.	Pointwise Grid Quality Scores	34
3.5.	Test Matrix	44
4.1.	Contoured geometry exit conditions	65
4.2.	Normal hole geometry exit conditions	84
4.3.	Exit condition comparison for all geometries	100
A.1.	Total pressure loss results of Rayleigh study	118

COOLING REQUIREMENTS FOR THE ULTRA-COMPACT COMBUSTOR

I. Introduction

1.1 *Background*

After Sir Frank Whittle and Dr. Hans von Ohain introduced the turbojet concept in the 1940's, turbine engines have become an integral part in aviation community and is the major propulsion system in modern aviation. Since the birth of turbine engines, the demand to expand the power output of the turbine engine has increased. Over the past six decades, both civilian and military efforts have been made in achieving higher thrust out of aircraft turbine engines. Increasing the turbine inlet temperature, $T_{t,4}$, is one method to improving the specific thrust output. Figure 1.1 illustrates the rising trend of $T_{t,4}$ and the employment of high-temperature materials to protect the turbine components within the engine [3].

Although great improvements have been made with materials to withstand extreme temperatures, high temperature materials still remain to be a limiting factor as to how much the turbine inlet temperature, $T_{t,4}$, can be increased. To meet the requirements of increasing specific thrust and overall engine efficiency, designers have been forced to come up with innovative ways to increase thrust-to-weight performance of an aircraft. Such ways include methods increasing specific thrust, reducing the engine weight and size, and repacking engine components in order to get a more compact engine.

One thrust-to-weight improvement method currently being investigated is the development of a inter-turbine burner system. Sirignano and Liu [26] introduced the concept of inter-turbine burning and revealed that there is an advantage of burning in the turbine. This concept is similar to an afterburner where more energy is added to the propulsion system by burning fuel in the aft section, but for an inter-turbine

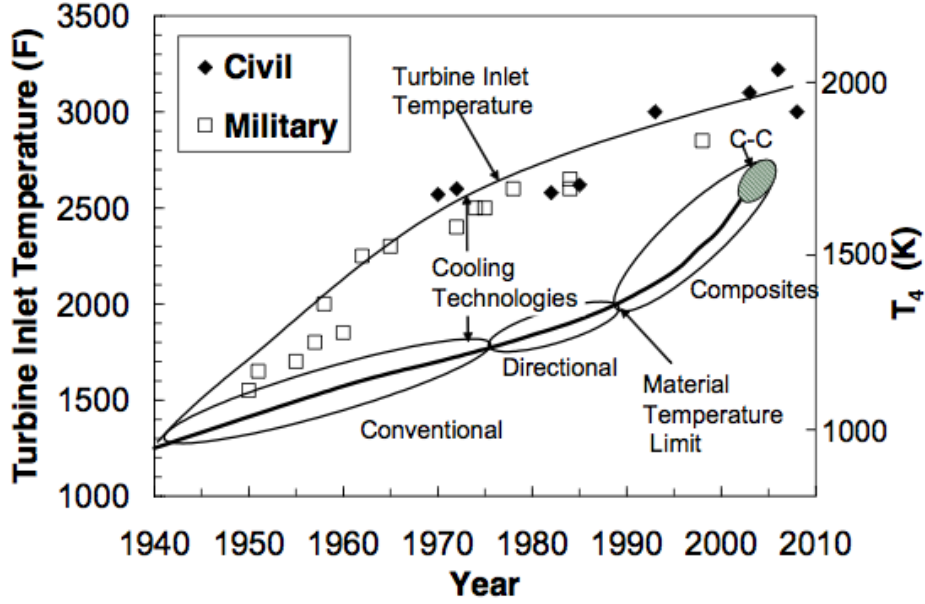


Figure 1.1: History of Turbine Inlet Temperature & Material Use In Aircraft Engines [3]

burner system the additional fuel is burned in the turbine. They point out that the overall efficiency of the engine decreases when using an afterburner because the fuel is burned in a low pressure environment. They argue instead to burn the fuel in the turbine where there are higher pressure levels. From their cycle analysis, a 25% increase in specific thrust can be achieved through turbine burning. For an afterburner to produce the same amount of thrust, a 50% increase in thrust specific fuel consumption (TSFC) is required while a turbine-burner application had a 10% increase in TSFC. This performance gain translates into having a more powerful engine for the same size or a smaller and compact engine for the same performance.

1.2 Motivation

Over the past several years, the Air Force Research Laboratory (AFRL) and the Air Force Institute of Technology (AFIT) have worked on the Ultra-Compact Combustor (UCC). The UCC is a unique combustion system that utilizes a high-g combustion environment during the combustion process of the gaseous fuel. AFRL is

investigating this system as an inter-turbine stage burner application because of its reduced size and volume. Work done by Zelina et al. [31] estimated a 66% reduction in combustor length. Unlike a conventional axial burner, the UCC is able to reduce its size by combining the last compressor exit guide vane, combustor, and the first turbine inlet guide vane. The combination of these components make a hybrid vane which helps to provide the correct flow angle to the turbine rotors.

Most recently, a computational study on the UCC done by Bohan [6] revealed that high temperatures are predicted to occur on the suction side surface of the hybrid vane. Non-uniform temperature profiles were shown for the 20 vane UCC study. This was due to the exhaust gases exiting the circumferential combustor and unburnt fuels interacting with the remaining compressor air. In order for the UCC to be realized in a fighter-sized turbine engine, further understanding is required on how to control the temperature profiles predicted to occur on the hybrid vane.

Since the 1970's, film-cooling schemes have been exploited in order to raise the material capability to withstand extremely high inlet turbine temperatures experienced on the turbine airfoil for traditional turbine engines. In general, film cooling introduces a thin layer of coolant air over a surface of interest to protect against hot freestream gases. This method is applied on the airfoil through use of compressor bled air exhausted through holes drilled in the airfoil surface.

Through the use of film cooling, an attempt will be made to control the temperature profiles predicted to occur on the hybrid vane. One of the issues that arises stems around the fact that the hot gases also contain incomplete combustion products and that secondary reactions are likely to occur in the vicinity of the airfoil surface. This additional heat release has been shown, by Polanka et al. [24] and Evans [11], to be enhanced in the presence of the additional oxygen from film cooling holes.

1.3 Thesis Scope

The primary objective for this thesis was to investigate the use of film-cooling technology within the UCC and better understand how the coolant flow interacts with the cavity and core flow. The first part of this study is to establish a baseline model to better understand where secondary reactions will potentially occur in the UCC. Looking at predicted temperature profiles on the surfaces of the UCC will dictate where the film-cooling holes should be placed. In addition, the concentration of carbon monoxide will be quantified as an indicator of whether incomplete combustion will exist as it exits to the first turbine blade. The next step is to investigate cooling scheme variations and analyze the effects of using such schemes. The end goal of this research is to identify the cooling requirement of the UCC in order for the UCC to be a realizable technology in a fighter engine.

II. Background

2.1 *Centrifugal Force Combustion*

In principle, the Ultra-Compact Combustor (UCC) is based on centrifugal forced combustion. The benefit of centrifugal force combustion was reported by Lewis [20] in 1973 where he studied flame propagation in a centrifuge combustor for a propane-air mixture. The effect of burning fuel under high g-loaded conditions raised the flame speed and reduced the reaction time required for combustion completion, which in turn allows for a shorter combustor length and thus weight savings.

Lewis found that under high g-loading, an increase in flame speed can be achieved beginning at 200 gs. A transition region occurred from 200 to 500 gs, after which a relationship of the flame speed growth proportional to the square-root of the g-loading was established up to a limit of 3500 gs. Between this range of 500 and 3500 gs, flame speeds resulted in values of 35 to 100 m/sec. The driving force behind the increase in flame speed was due the presence of bubbles and eddies in the reaction. Lewis analysis stated that the propagation of a flame was dictated by the bubble velocity when the turbulent flame speed was less than the bubble velocity value.

An illustration of this concept is shown in Figure 2.1. Here the illustration captures the effect of centrifugal forces on flame spreading. In Figure 2.1, the left side depicts the bubble velocity dominating the turbulent flame speed and advances ahead, and on the right side the flame propagates at the turbulent flame speed.

An additional study by Zelina et al. [31] further investigated the stability of a flame under g-loaded combustion. The findings of their results mapped the stability region of a flame under various operating conditions. Through a series of lean blowout (LBO) tests, the maximum g-loading occurred between 7,000 and 8,000 gs. Along with the LBO tests, Zelina et al. [31] conducted a study for a small scale UCC prototype. Under atmospheric conditions for a JP-8 +100 fuel mixture, their experimental results showed combustion efficiencies above 95%. The highest combustion efficiency reached was 98.5% for an equivalence ratio of 1.6 that corresponded to a g-loading value of

1000 to 2000 gs. Figure 2.2 captures the results of Zelina et al. Under g-loaded combustion, a 50% reduction in flame length was also noted.

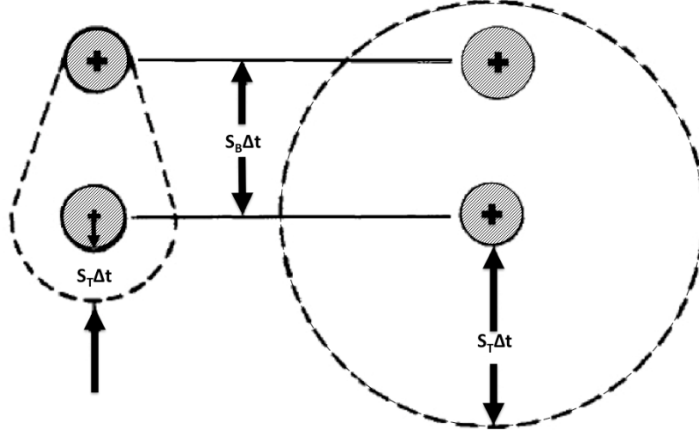


Figure 2.1: Flame Propagation where (left) bubble velocity is greater than the turbulent flame speed, and (right) bubble velocity is lower than the turbulent flame speed [20]

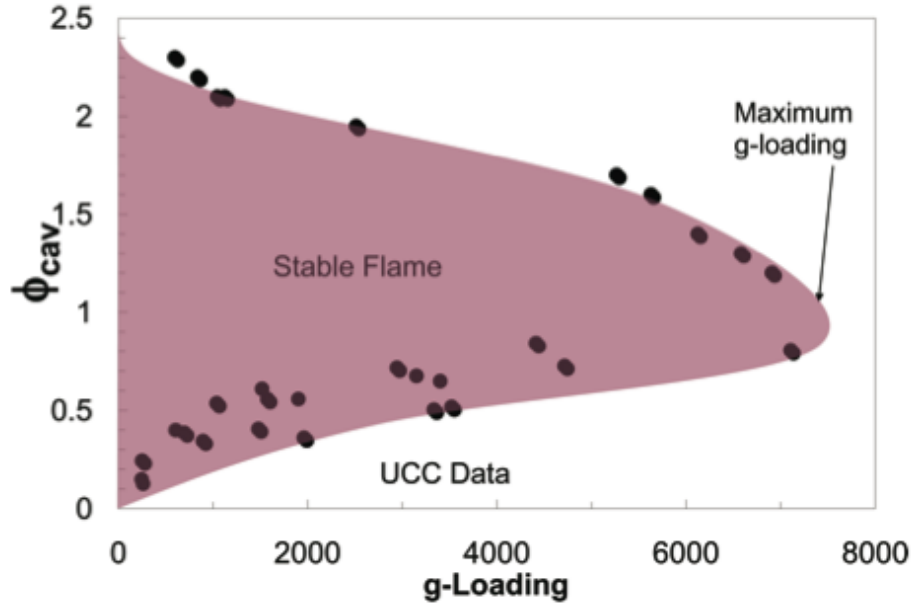


Figure 2.2: Flame stability range created by Zelina et al for equivalence ratio at blowout with respect to g-loading [31]

2.2 Inter-turbine Burner

The idea of inter-turbine burning was first coined by Sirignano et al. [26] and is a concept where fuel is burned inside the turbine purposely. In a thermodynamic cycle analysis, Sirignano showed a 20% increase in specific thrust with only a 10% increase in thrust specific fuel consumption (TSFC) for a turbine-burner configuration. Their analysis also showed that in comparison to an afterburner, a 50% increase in TSFC was required in order to achieve the same amount of thrust. The additional power drawn from the the low pressure turbine could supply a generator to support electronic devices on aircraft. It is also possible to harness the energy to power an ultra-high bypass turbofan [31].

This proof-of-concept study done by Sirignano has gained the attention of the Air Force Research Laboratory (AFRL) Turbine Engine Division and the Air Force Institute of Technology (AFIT), and several initiatives have gone underway in understanding how to make the ultra-compact combustor as an inter-turbine burner application for aircraft turbine engines.

2.3 Computational Work on Ultra-Compact Combustor

From the start of the interest on the Ultra-Compact Combustor by AFRL and AFIT, computational fluid dynamics has played a prominent role in understanding the fluid and thermal behavior in the UCC. Its key role has given insight into the complex flow patterns formed within the UCC as well as backing experimental data collected.

One study done by Thornburg et al. [28] looked at the combustion flow field for a UCC design with curved radial vane cavities recessed on the suction side and pressure side surfaces of the vane. The purpose of this vane cavity was to assist with migrating the gaseous fluid from the circumferential cavity into the core flow. Figure 2.4 shows a solid model of the vane with the radial cavity placed on the suction side surface. For their study, three-dimensional simulations were done using Fluent®

6.3.26 CFD software for a single-step combustion reaction of kerosene under atmospheric conditions. The Realizable $k-\epsilon$ model was employed for turbulence modeling. Boundary layer resolution was created by using an initial distance of 0.9 mm with a growth rate of 1.1 to yield a Y^+ range of 50-300.

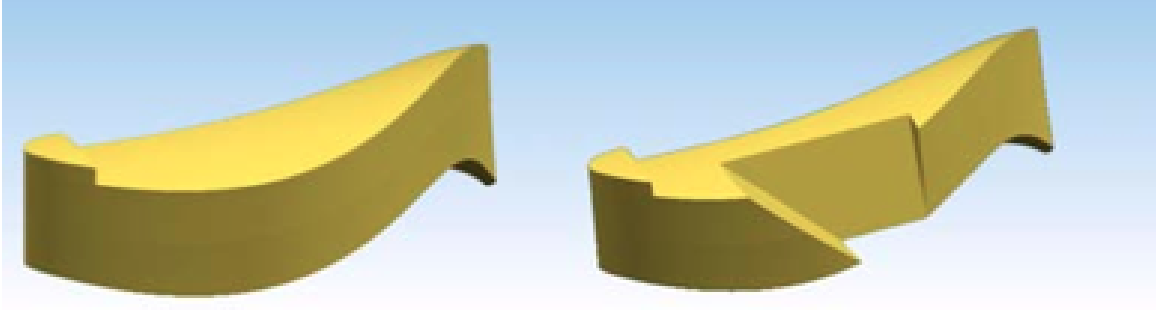


Figure 2.3: Radial Vane Cavity Configuration Schematic with Vane Cavity (right) and without Vane Cavity (left) [28]

For their study, they looked at varying the direction of the circumferential flow in the clockwise and counter-clockwise direction as well as vary the radial vane cavity by placing it on the suction side or pressure side surface of the vane. In Figure 2.4, a two-dimensional cross-sectional view for the the four test configurations is summarized. In Figure 2.5, the spanwise temperature averages at the exit location of the UCC are shown. The results show that the configuration with the radial vane cavity on the suction side surface and a counter-clockwise flow in the circumferential direction resulted in the most desired exit temperature profile with a peak temperature of 950K located mid span.

Anisko [1] conducted computational work on the UCC and looked at the effect of varying the circumferential cavity size from 25.4 mm to 38.1 mm. In his analysis, he looked at the combustion of the kerosene for 11 species model tracking O_2 , N_2 , $C_{12}H_{23}$, CH_4 , CO_2 , CO , H_2 , H_2O , H_2O (liquid), OH and C . Using Fluent[®] 6.2, he found in his investigation that the 25.4 mm circumferential cavity size reduced the harmful emissions exiting the UCC with lesser CO produced at the exit. Consequently

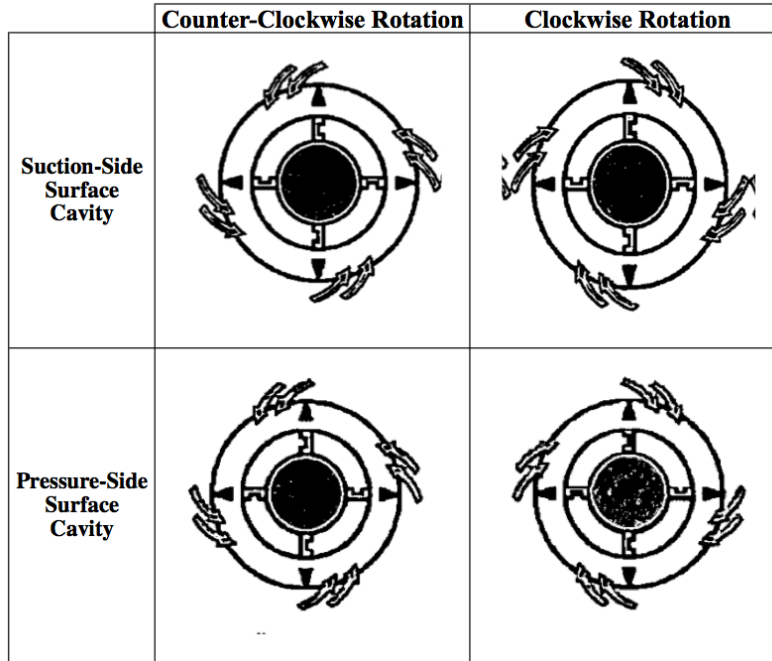


Figure 2.4: Two-Dimensional View of Radial Vane Cavity Test Configurations Looking Upstream [28]

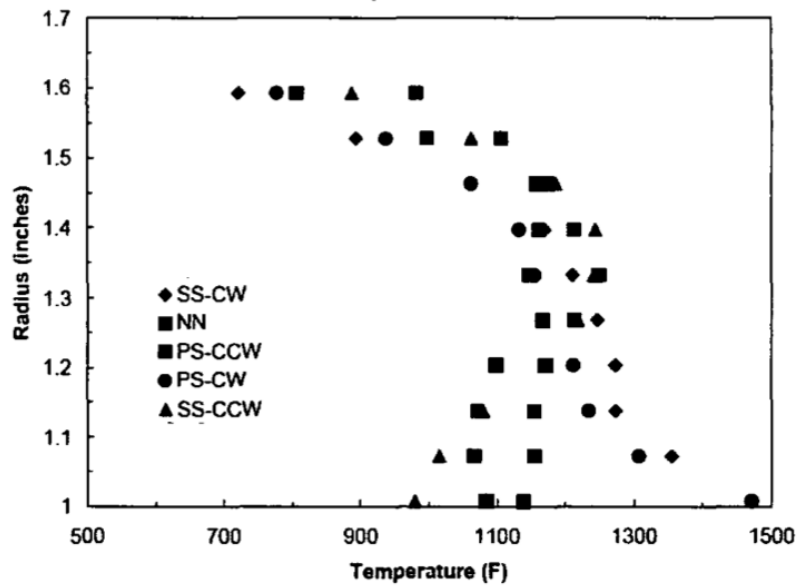


Figure 2.5: Spanwise Temperature Averages at UCC Exit of Thornburg et al. for Suction-Side Clockwise and Counter-clockwise Rotation (SS-CW and SS-CCW), Pressure-side Clockwise and Counter Clockwise Rotation (PS-CW and PS-CCW) [28]

though, the pattern factor and profile factor increased with higher heat loads near the upper endwalls.

The most recent computational UCC study was performed by Bohan [6]. In this study, the flow behavior was interrogated for a UCC sized to the dimensions of a traditional fighter-sized engine. Using Fluent[®] 6.3, Bohan generated a solution model based on a three-dimensional, steady-state, pressure-based solver which included a RANS turbulence model. His study considered operating conditions for pressures at atmospheric and engine representative conditions. Multiple test cases were run for various UCC geometries. Variations such as the cavity size, vane geometry, core mass flow, number of vanes and cavity air inlet sizes were considered. The goal of this effort was to understand how the fluid migrates in the UCC as air and fuel are introduced into the cavity, combusted, then exited and interacted with the core flow air from the compressor. As sectional view of the UCC studied by Bohan [6] is shown in Figure 2.6a. Figure 2.6b shows a two-dimensional layout of the UCC. Here the core fluid flows from left to right.

The findings of his results revealed that as the fluid exits the cavity and into the core flow the momentum from the core flow pushed the hot gases from the cavity along the suction side of the airfoil vane. The hot gases predominantly resided along the suction side and inner diameter endwall surfaces. In Figure 2.7, the temperature profile predicted to occur on the suction side surface of the UCC hybrid vane is shown. Bohan also showed that the exact locations of the hot gases can be altered by changing the mass flux ratio (MFR) of the flow in the circumferential cavity to the core flow. The MFR significantly altered the injection angle that the hot gases followed as they entered the core flow. This variation was also shown experimentally by LeBay et al in a small scale sector model. [17] Controlling the location of the hot gases is essential if the part is to be cooled effectively.

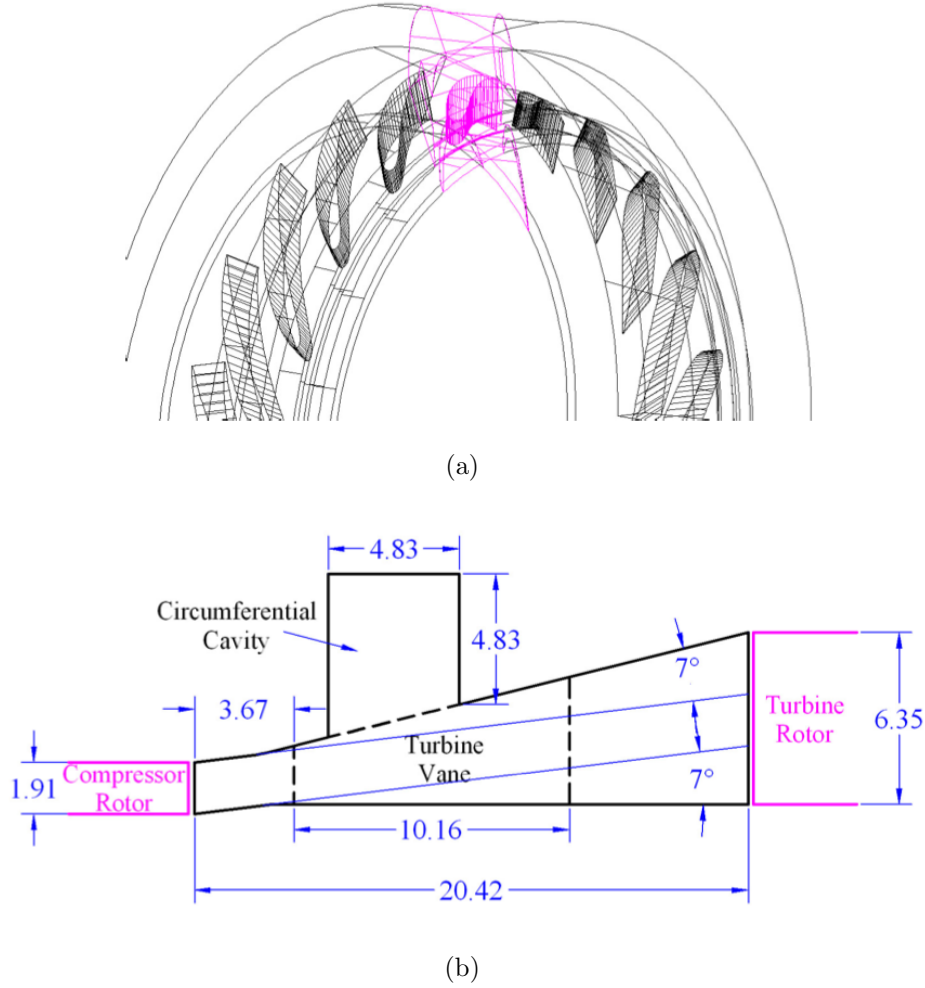


Figure 2.6: UCC geometry studied by Bohan [6] a) annular view of UCC geometry b) 2-D cross-sectional view (cm)

2.4 Film-Cooling Background

While high temperature materials have allowed for higher inlet turbine temperatures within engines, the use of cooling schemes remain to be an integral part of turbine designs preventing material failure and extending the life of a component. Prior to film-cooling, convective cooling was the most traditional and simplest way to cool the turbine. Turbine blades were internally cooled as the bled air from the compressor flowed through serpentine passages within the vane. As the allowable metal temperature required more cooling film-cooling was utilized. Figure 2.8 cap-

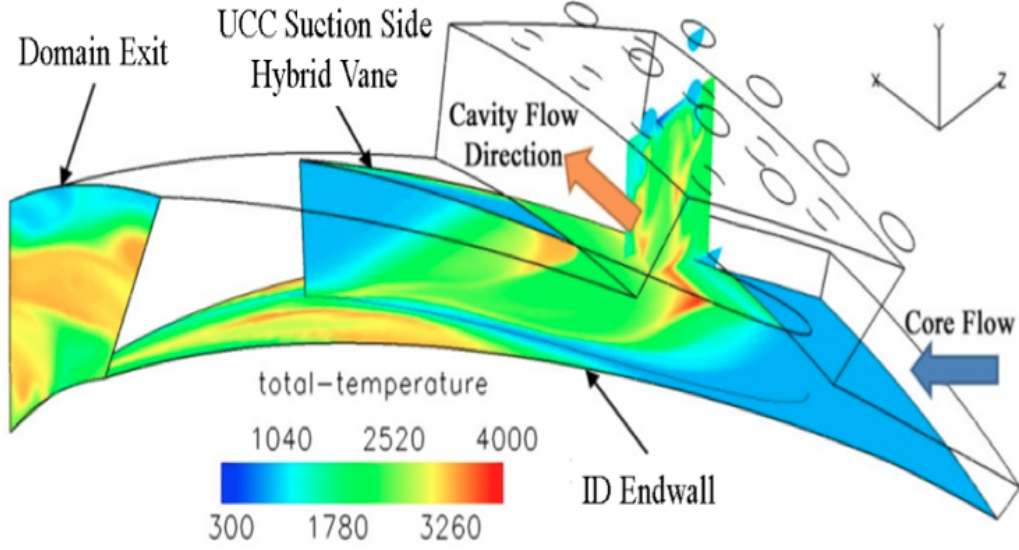


Figure 2.7: Predicted Temperature Distribution for 20 Hybrid-Vane UCC Configuration done by Bohan [6]

tures how the turbine airfoil is cooled and shows where cooler air (red streamlines) is bled from the compressor then exists the holes and flows over the surface of the airfoil [5] .

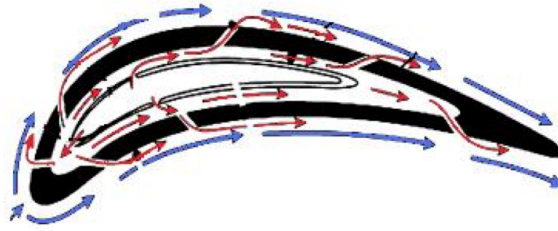


Figure 2.8: Typical schematic of turbine airfoil geometry [5]

A comprehensive report done by Bogard and Thole [5] states that six factors have a significant impact on film-cooling performance. A summary of these factors can be seen in Table 2.1. Because these factors are not independent, various combinations of film-cooling schemes exists and a great amount of research has been done on finding the optimum film-cooling scheme. The following sections describe studies that been done in order to understand the effects of each parameter in a fluidic, geometric and computational point of view.

Table 2.1: 17 Factors Impacting Film-Cooling Performance [5]

Coolant/Freestream Conditions	Airfoil Geometry	Hole Configuration*
Mass flux ratio*	Hole Location:	Shape of Hole
Momentum flux ratio*	- leading edge	Injection Angle
Mainstream turbulence*	- main body	Compound Angle
Density Ratio	- blade tip	Pitch distance
Approach Boundary Layer	- endwall	Length of Hole
Mainstream Mach Number	Curvature*	Number of rows
Unsteady Mainstream Flow	Roughness*	
Rotation		

*Significantly effects the predictability of film-cooling performance

2.4.1 Fluid Mechanics. In designing the cooling system for airfoils, a crucial parameter to be understood is the coolant's flow distribution. One of the flow variables influencing the flow distribution and effectiveness of film-cooling is the mass flux ratio. In equation 2.1, mass flux ratio, often referred to as the "blowing ratio", is defined as the product of the density, ρ_c , and velocity, U_c , of the coolant jet over the product of the density, ρ_∞ , and velocity, U_∞ of the freestream flow.

$$M = \left(\frac{\rho_c U_c}{\rho_\infty U_\infty} \right) \quad (2.1)$$

A study conducted by Goldstein et al. [14] looked at film-cooling performance for a single hole and row of holes spaced three diameters for blowing ratios ranging from 0.1 to 2.0. As expected the row of holes performed better than the single hole at higher blowing ratios due to the row of holes having less penetration strength, and as a result the force from the mainstream flow turns the coolant flow back onto the surface. The single hole configuration on the other hand penetrates through the mainstream flow, if the blowing ratio is too high, and leads to separated coolant flow over the surface. The range of blowing ratios studied by Goldstein et al. [14] showed that the film effectiveness for the row of holes initially increased up to a blowing ratio of 0.5 then decreased after the effects of blowing ratios weakened further downstream. Figure 2.9 illustrates the effect of blowing ratios on the center line value of the film effectiveness from the study of Goldstein et al [14].

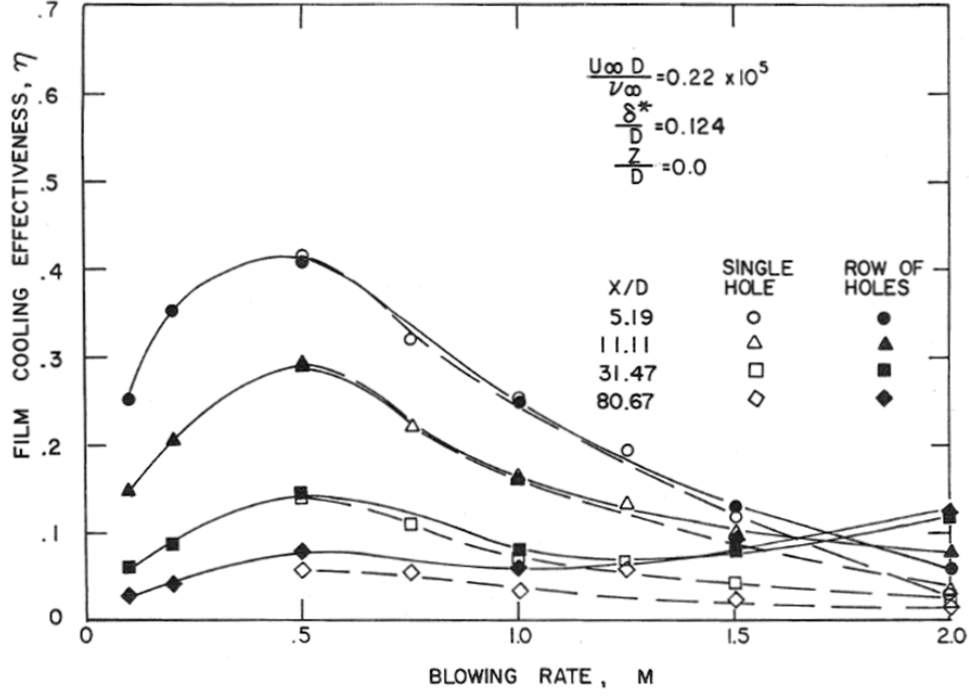


Figure 2.9: Influence of Blowing Ratios for a Row of Holes [14]

Another flow property influencing the distribution of the coolant flow is the density ratio of the coolant to the hot gaseous freestream flow. Pedersen et al. [22] was the first to investigate this variable and studied density ratio effects between the range of 0.2 and 2.0, and they found that as the density ratio decreased the lateral average film effectiveness increased. The reason was because the density ratio is intrinsically defined in the momentum flux ratio where the momentum flux dictates whether separation occurs [5]. Another study completed by Sinha et al. [25] investigated density ratios ranging between 1.2 to 2.0. From their study, they independently varied the density ratio to examine the film effectiveness based on velocity ratio, mass flux ratio and momentum flux ratio. The study revealed that the effect of film effectiveness could not be scaled with mass flux ratio, velocity ratio or momentum flux ratio. The results showed that the centerline effectiveness scaled with mass flux ratio when the jets remained attached (for $M = 0.5$), and when the flow detached, the momentum

flux ratio was the best scaling parameter [25]. The results of Sinha et al. [25] also revealed that there was a dependency of laterally averaged effectiveness with coolant jet spreading. This spreading was found to be dictated by the density ratio and momentum flux ratio where the decrease of density ratio and increase momentum flux ratio significantly degraded the effectiveness as the coolant jet spreading reduced [25].

To further understand what dictated this separation, Thole et al. [27] characterized the coolant jet flow separation for a density ratio range of 1.2 to 2.0 and found that separation was a function of momentum-flux ratio rather than the mass flux ratio and velocity ratio. Through the use of thermal field measurements, Thole et al. identified three distinct ranges of momentum flux ratios dictating flow separation. The first regime where $I < 0.4$ the coolant flow remained attached to the surface. The momentum flux ratio, I , is defined in Equation 2.2. For next regime, the coolant jet detached then reattached between $0.4 < I < 0.8$. Complete detachment was seen for $I > 0.8$.

$$I = \left(\frac{\rho_c U_c^2}{\rho_\infty U_\infty^2} \right) \quad (2.2)$$

The next significant variable influencing the distribution of coolant flow is the freestream turbulence flow that exits the combustor. Traditionally, the turbulence levels are computed in the following manner for turbine aero-engines:

$$Tu = \left(\frac{u_{rms}}{U} \right) \quad (2.3)$$

In Equation 2.3, u_{rms} is the root-mean-square velocity fluctuation and U is the magnitude of the mean velocity. Realistic levels of Tu simulating that of a turbine aero-engine combustor exit is nominally 20% [5]. Bons et al. [7] investigated the effects of high freestream turbulence for a single row of film cooling holes for a range of $Tu = 0.9$ to 17%. In the analysis, they considered a row of five cylindrical holes with a pitch distance of three hole diameters inclined 35° . In their findings, the results show

that high freestream turbulence helps with diffusing the coolant flow back onto the surface for high blowing ratios ($M > 0.95$) [7]. While Bons et al. studied a constant density ratio of 0.95 [7], Schmidt and Bogard [5] investigated a representative density ratio of 2.0 for the coolant. The results agree with Bons et al. and found that the optimum film effectiveness occurred at $I = 1.1$ for high freestream turbulence.

2.4.2 Hole Geometry. Aside from the fluid mechanics of film cooling, the geometry of the coolant hole can impact the cooling effectiveness. Ideally a continuous slot configuration provides a higher film-cooling effectiveness based on Hartnett et al. [16], but the application towards turbine airfoils is structurally unsound. A majority of film cooling configurations applied within turbine engines are based on discrete hole schemes. The three most common coolant hole shapes are: cylindrical, fan-shaped and laidback fan-shaped. Figure 2.10 depicts the typical geometries.

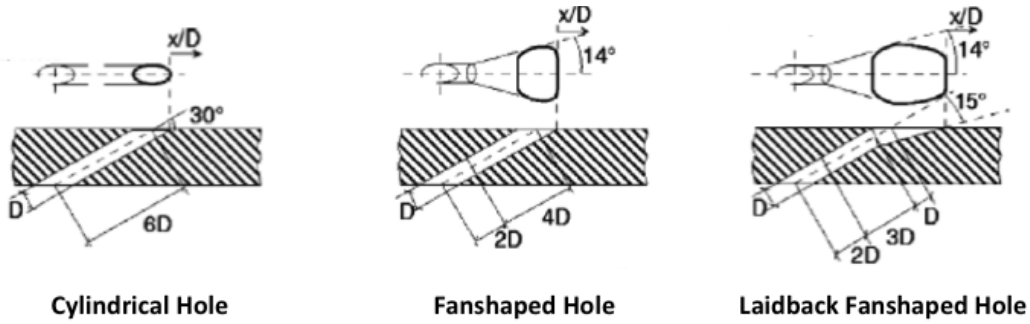


Figure 2.10: Standard coolant hole geometries [5]

Gritsch et al. [15] performed a study on film cooling effectiveness for the hole types mentioned above, and their findings revealed that at higher blowing ratios the shaped holes offered higher cooling performance compared to the cylindrical holes. For their analysis, they studied three blowing ratios ($M = 0.5, 1.0$ and 1.5) and measured the film-cooling effectiveness of each hole geometry. Data measurements were collected using a continuous flow wind tunnel where the plenum of air came from a high pressure, high temperature test facility. From the experiment, they demonstrated that the use of a diffuser shaped expansion hole aided in keeping the

flow attached for higher blowing ratios thus increasing adiabatic effectiveness. The advantage of a laidback shape hole results from an improved lateral spreading of coolant in comparison to the symmetrical cylindrical hole.

As mentioned earlier, a continuous slot is much more desired than a discrete cooling hole configuration because of the higher cooling effectiveness levels. In 2002, a study was completed by Bunker [8] on a traverse slot configuration encompassing a row of discrete holes. This holes-in-slot concept resembles slot cooling while remaining structurally sound. In his study, he investigated the film-cooling adiabatic effectiveness for a blowing ratio range between 0.75 to 4, and his results revealed that trench depth is a primary factor in approaching a 2D-slot film scheme performance. For all the blowing ratios there were no variations in film-cooling performance, but as the trench depth decreased, the film effectiveness modeled that of a normal 2D-slot cooling scheme [8]. Using a holes-in-slot design where trench depth was less than half the hole diameter, film effectiveness improvements of 50 to 75% were achieved [8].

In addition to the coolant hole exit, other geometric parameters influencing the performance of film cooling are the inclination angle of the coolant hole to the surface, pitch-to-diameter ratio and length-to-diameter ratio [5]. Bogard and Thole [5] report that the inclination angle of the coolant impacts the performance of film cooling as the angle is varied between the coolant holes and the surface. Traditionally inclination angles are 25-35° to the surface. According to Kohli et al., Foster et al., and Baldauf et al. [2, 13, 19], using a shallow inclination angle enhances the coolant jet to remain attached to the surface as it exists the coolant hole. The effects of inclination angle on the performance of film cooling effectiveness have been studied. Kohli et al. [19] investigated inclination injection angles of 35 and 55° and the results revealed that the steeper injection angle decreased the film effectiveness by 10 and 30%. Baldauf et al. [2] looked at inclined injection angles of 30, 60 and 90° and found a 30% decrease in the average film effectiveness for a 90° coolant hole injection setup compared to the 30° injection angle setup.

Pitch is the distance between the center of coolant holes and, generally, the values seen are three hole diameters [5]. Dittmar et al. [10] assessed four different film cooling injection geometries on the suction side of an actual turbine guide vane. In this study, they analyzed the film cooling effectiveness and heat transfer coefficient measurements between double row cylindrical holes, double row discrete slots and single row fan-shaped holes. For the cylindrical holes and discrete holes, a pitch of four diameters was used and staggered at a pitch of two diameters. For the single row hole setup, two fanshaped hole configuration were tested: one without a compound angle and one with a compound angle of 35° . All configurations were inclined at 45° and tested for blowing ratios between 0.2 and 3.0 at a freestream turbulence value of 9%. The findings of Dittmar et al. [10] showed that at low blowing ratios minimal differences were seen in film cooling effectiveness for all configurations. At higher blowing ratios the results revealed the fanshaped hole configuration performing the best.

2.5 Concerns of Heat Release Effects

With typical turbine engines operating at higher temperatures and higher fuel-to-air ratios, attention has been placed on preventing secondary reactions to occur in the core flow. The UCC is expected to operate at high fuel-to-air ratios and may have the potential for secondary reactions to form due to unburnt fuel escaping because of less residence time from the shortening of the combustor. Kirk et al. [18] studied the effects of secondary heat release and argued that the driving factors that lead to secondary reactions are mixing and oxygen rich environment that would create an environment of secondary reactions to occur. When applying film-cooling within a turbine engine, an oxygen rich region is created. This region is formed from the air ejected out of the coolant holes that creates the protective layer from hot gases. As hot gases convectively transport across the protected surfaces there is potential to have remaining species, not fully combusted, to travel and mix with the cooling film. These species could further be oxidized from the "oxygen rich" coolant film and secondary

reactions could occur on the surface. Obviously this would deteriorate the film cooling effectiveness and locally heat up the surface that was intended to be protected from hot gases. Figure 2.11 shows a traditional axial combustor and portrays the secondary reactions of fuel with coolant film within a turbine by Kirk [18].

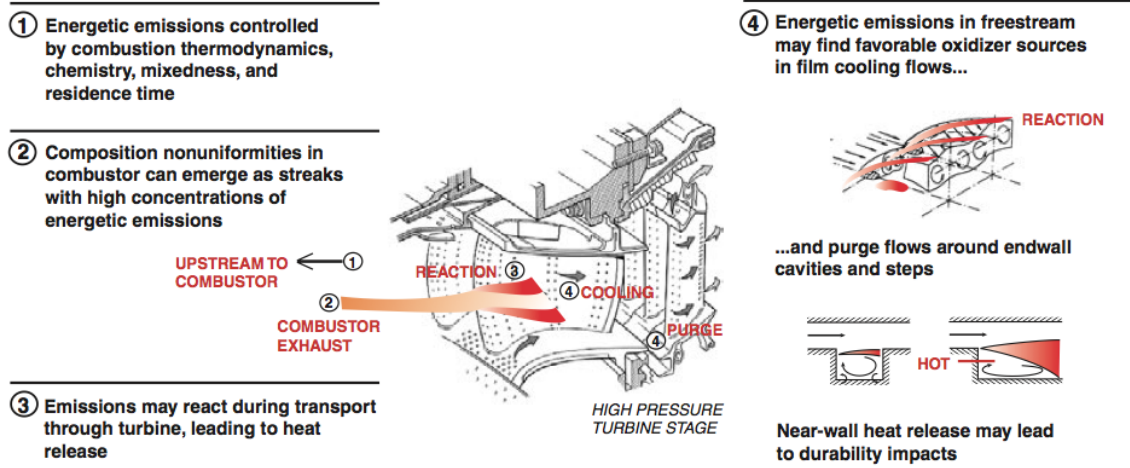


Figure 2.11: Progression of continued heat release within a turbine [18]

Experimental work done by Polanka et al. [24] and Evans [11] investigated the impact of secondary reactions with film cooling. For this study, different coolant hole configurations were analyzed and tested at different equivalence ratios and blowing ratio conditions. The results of from the studies done by Polanka et al. and Evans revealed that the impact of heat release varied as the blowing ratio, equivalence ratio, and coolant hole geometries changed. In their studies, a Well Stirred Reactor (WSR) was utilized to provide the vitiated flow across a flat plate with interchangeable film-cooling test plates. The investigation was performed using nitrogen and air as the coolant supply. The results of the study uncovered that secondary reactions did occur for equivalence ratios less than unity. In Figure 2.12, the still image shows the results of the angled cooling hole configuration at an equivalence ratio of 1.5 for the nitrogen coolant at a blowing ratio of 2, air coolant at also a blowing ratio of 2, and lastly air coolant at a blowing ratio of unity. In Figure 2.12a-b, the images show a non-reacting case and a reacting case for nitrogen and air, respectively. This work

clearly demonstrated the possibility of the reactions to occur with fuel streaks in an exahust when introducing air coolant.

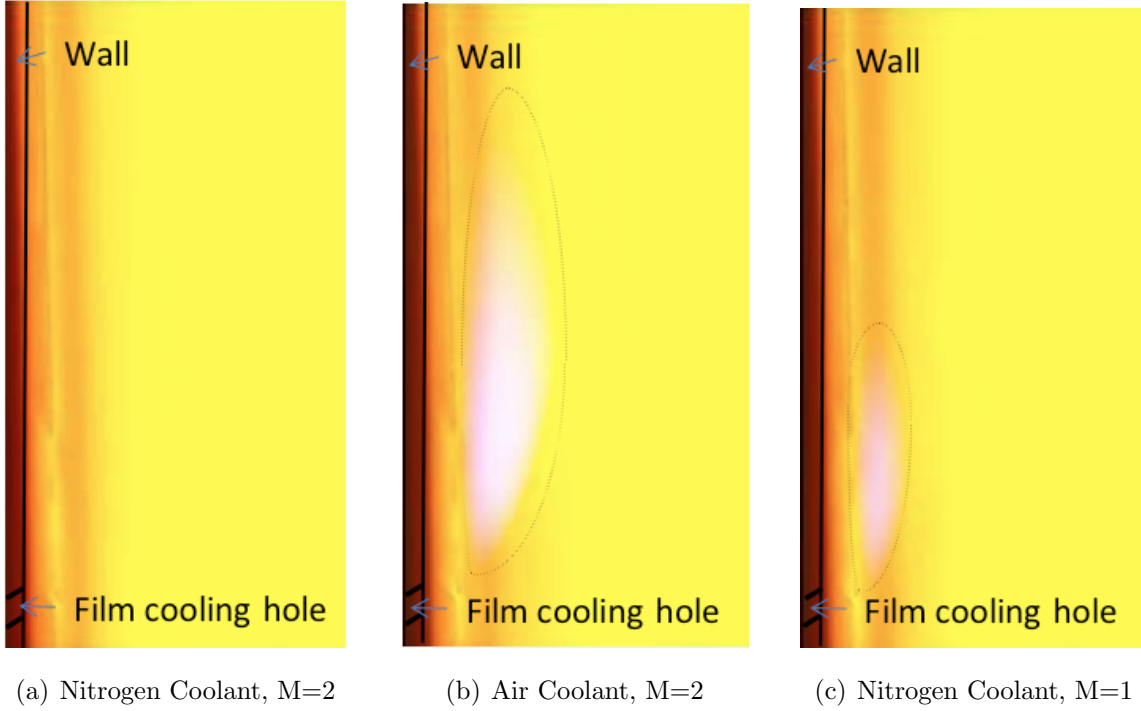


Figure 2.12: Experimental results of Polanka et al. [24] for an angled hole geometry, $\phi = 1.5$

In addition to the experimental work done by Polanka et al., a computational study was conducted Thornburg et al. [29] that validated the experimental data of Polanka et al. For this film-cooling study anlaysis, the study incorporated a widely used Shear-Stress Transport (SST) $k-\omega$ turbulence model to close the Reynolds-Averaged Navier-Stokes (RANS) equations and included a two-step reaction scheme for the combustion of propane. A mesh view of the normal hole, angled hole and fan-shaped hole geometries studied can be seen in 2.13. The numerical results of the study captured the secondary reactions seen by the work of Polanka et al. [24]. In Figure 2.14, the temperature contours show the secondary reactions with air coolant in the right-hand column. In comparison to the N_2 coolant (left-hand column), it is clear that the cooling effectiveness of air is impacted in a fuel rich environment.

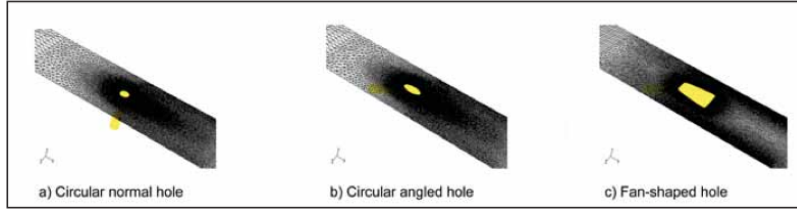


Figure 2.13: Mesh view of circular normal hole, angled circular hole and fan-shaped hole studied by Thornburg et al [29]

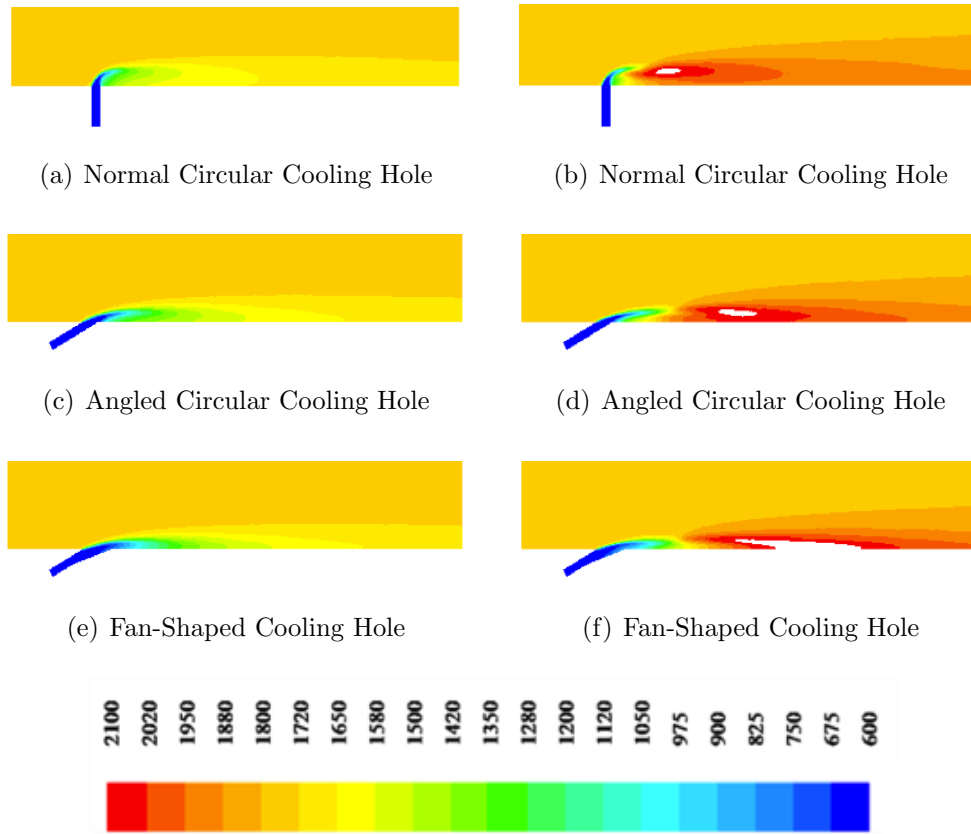


Figure 2.14: Computational Results of Heat Release Study by Thornburg et al [29] at midplane: a,c,e) N_2 Coolant and b, d, f) Air Coolant, $\phi = 1.5$, $M=1$

III. Methodology

The following chapter describes the methodology of the numerical film-cooling analysis within the Ultra-Compact Combustor performed in this investigation. Discussion is made on the test geometries and the numerical procedures for this research effort. The computational analysis is based on a widely used simulation code called ANSYS Fluent®. Fluent® 13.0.0 is commercially available software with the capability to model complex flows such as internal combustion, aerocoustics, turbomachinery and multi-phase flow systems. Numerical computations for this effort were carried out on Cray XE6 system located within the AFRL DoD Supercomputing Resource Center (DSRC).

3.1 Research Objectives

For this research effort, the main objective is to apply film cooling within the UCC to hopefully mitigate the extreme temperatures predicted to occur on the hybrid vane. To accomplish this task, several subobjectives were established. The first task was to establish a baseline model to better understand where to focus for film cooling in the UCC. The second task was to apply film cooling at predefined locations and study the effectiveness of film cooling. In light of secondary reactions occurring due to the film cooling, heat release effects was analyzed. Lastly, the exit condition of the UCC was analyzed to determine whether unreacted species will potentially occur in the turbine section. A summary of these objectives are listed below.

- Establish a baseline model and investigate where reactions will occur
- Apply film-cooling technologies and analyze cooling effectiveness
- Investigate heat release effects in UCC
- Analyze the potential of secondary reactions exiting the UCC

3.2 Computational Setup

For the film-cooling studies, Fluent[®] 13.0.0 computational fluid dynamics software was used to simulate a combustion model of the UCC. The solver settings include a 3-dimensional, node centered, steady state, pressure-based solver with second order accuracy for momentum, density and energy with SIMPLE algorithm used for pressure-velocity coupling. From the results of Bohan [6] as well as Hermanson and Thole [27], the RNG $k-\epsilon$ turbulence model proved to be sufficient in capturing the secondary flows existing in the UCC due to the anticipated vortex shedding on the leading edge of the vane. For the film-cooling analysis, the turbulence model selected for closure of the RANS equations was Shear-stress Transport (SST) $k-\omega$ turbulence model with eddy-dissipation concept employed for the turbulence-chemistry interaction. This version of the $k-\omega$ model was used because of its dual advantage of resolving the flow both in the viscous sublayer region and wake region. This blended feature incorporated both the standard $k-\omega$ model and a modified $k-\epsilon$ model. Near the wall $k-\omega$ equations are utilized to compute the solution, and away from the wall (in the wake region) $k-\epsilon$ equations are used to simulate the turbulent flow.

3.2.1 Turbulence Comparison Study. A simple preliminary film-cooling study was conducted to analyze the difference between the RNG $k-\epsilon$ and SST $k-\omega$ models for a 30° angled, cylindrical film-coolant hole simulation over a flat plate. This configuration was similar to the work done by Polanka et al. which supplemented experimental work done on heat release in turbine cooling [24].

In Figure 3.1, a layout of the test section is shown for the study. Here mass flow inlets were defined for the coolant hole and freestream flow coupled with a pressure outlet as the outflow. For this analysis, only one case was considered from the study of Polanka et al. [24]. The work done by Polanka et al. studied the reactions of air and N_2 coolant subjected to a cross stream flow with unburned fuel. The computational setup used for the study of Polanka et al. included a RANS model with SST $k-\omega$ turbulence modeling.

For the turbulence comparison study, only air coolant was investigated for a blowing ratio of unity. The coolant flow was set to mass flow of $1.35\text{e-}6$ kg/sec at 607 K, and the mainstream flow was set at $5.2\text{e-}4$ kg/sec at 1828 K. A summary of the input values for the test case can be seen in the Table 3.1. In Table 3.2, the species composition of the two flows are shown. The mixture composition corresponds to an equivalence ratio of 0.95.

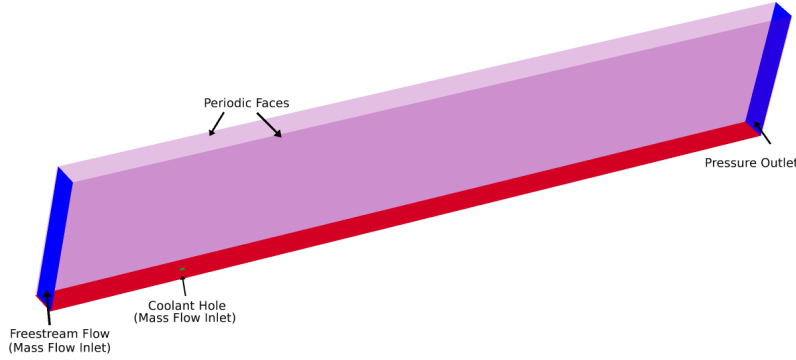


Figure 3.1: Computational schematic of turbulence test

Table 3.1: Fluent[®] turbulence test conditions

Parameter	Flow rate (kg/s)	Temperature (K)	Gauge Pressure (Pa)	Tu (%)
Freestream	$5.20\text{e-}04$	1828	1407	10
Coolant	$1.35\text{e-}06$	607	2169	1

Table 3.2: Species Mass Fraction Input Values

Flow	C ₃ H ₈	O ₂	CO ₂	CO	H ₂ O	N ₂
Freestream	0	1.09e-02	0.171	0	0.0935	0.72
Coolant	0	0.23	0	0	0	0.77

The numerical results from the study had shown reasonable agreement with the experimental data. Comparing the results to the work of Polanka et al. [24], the results are qualitatively comparable with the 30° angled, cylindrical film-coolant hole

simulation. In Figure 3.2, the contour temperature plots are shown from the side and top-down view. By inspection, the $k-\epsilon$ model diffuses the flow much faster than the $k-\omega$ turbulence model. This would be as expected because of the $k-\omega$ model being better near the walls. Thus for the film-cooling study portion, the SST $k-\omega$ turbulence model is used.

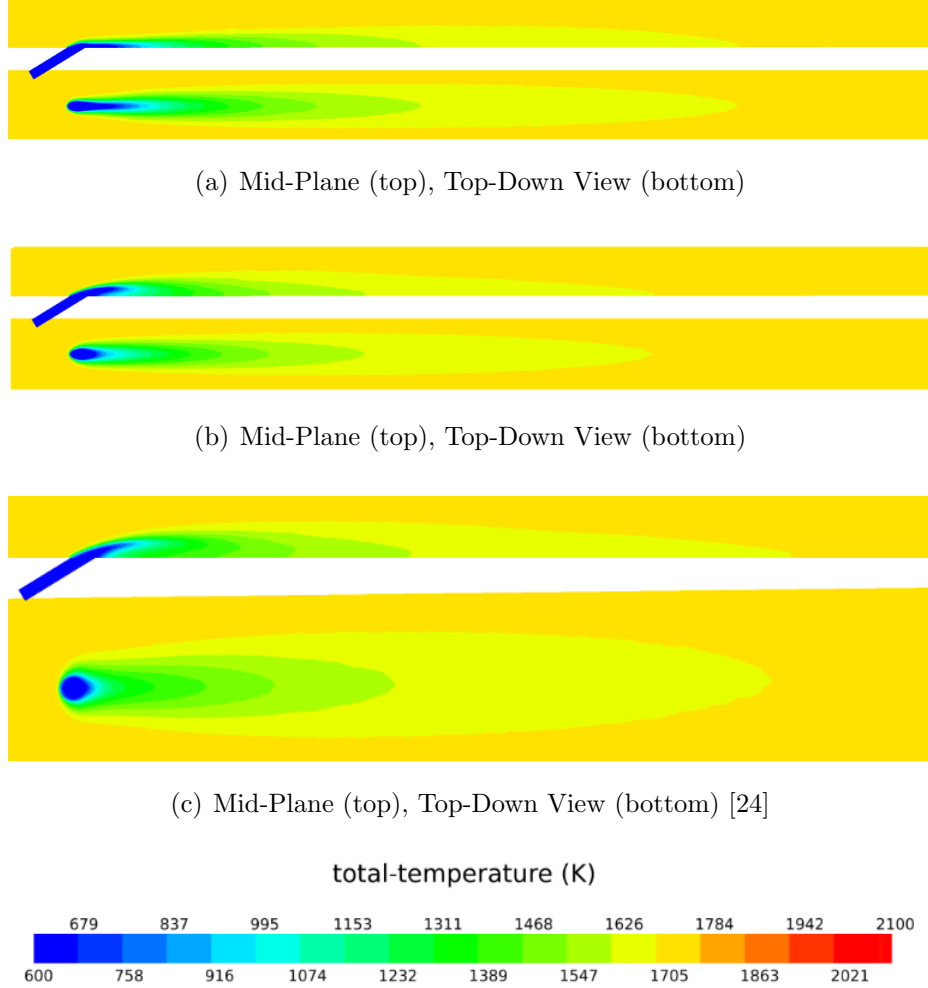


Figure 3.2: Temperature Contours of Turbulence Comparison Study for $\phi = 0.95$, $M=1$: a) RNG $k-\epsilon$ Model, b) SST $k-\omega$ Model, and c) Result of Polanka et al [24]

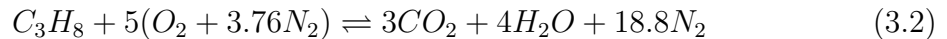
3.2.2 Chemistry Modeling. Within Fluent[®], there are several options available on how to model reacting flows. One model is a species transport model where the mixing and transport model of species are computed by solving the mass fraction

of each species, Y_i . A convection-diffusion equation is used in order to solve the conservation equations for each chemical species and is represented below:

$$\frac{\partial}{\partial t}(\rho Y_i) + \nabla \cdot (\rho \vec{u} Y_i) = -\nabla \cdot \vec{J}_i + R_i + S_i \quad (3.1)$$

The other models available are premixed, non-premixed, and partially premixed combustion models. The premixed combustion model requires the fuel and oxidizer to be intimately mixed together at the molecular level before entering the combustion control volume. Fluent recommends this approach to be best suited for modeling a thin, propagating flame front such as aspirated internal combustion engines and gas-leak explosions [12]. The other approach is non-premixed combustion model. Unlike the premixed model, the fuel and oxidizer enter the combustion volume separately, and the solution is solved based on the mixture fraction defined. For the non-premixed model, the flames are simulated based on the turbulence slowly convecting the fuel and oxidizer into particular reactions zones where they are then burned quickly [12]. For the partially premixed model, it incorporates both of the two previously discussed models. The partially premixed model is used for simulating combustion such as quiescent atmosphere, lean premixed combustors with diffusion pilot flame and imperfectly premixed inlet [12].

For the chemistry portion of the computations, combustion simulation was done using a 6-species transport model to represent the combustion of propane-air. For this model, the combustion process has a two-step reaction scheme. Below the reaction schemes are shown for the combustion of C_3H_8 and CO . For the 6-species transport model, the species solved during the combustion of C_3H_8 are C_3H_8 , CO , CO_2 , H_2O , O_2 and N_2 . For the turbulence-chemistry interactions, eddy-dissipation model was selected. In using the eddy-dissipation model the assumption is that the chemical reactions are burning and controlled by the turbulent mixing.





3.2.3 Solution Starting Sequence. During the preliminary phase of this study, solution instability was encountered given the complexity of the flow structure within the UCC. Based on the instability encountered, the test cases could not be started using the final desired settings and order of accuracy. In order to achieve the final desired settings and order of accuracy, the following changes were made as the solution progressed as shown at the end of this section. The start of each test case began with fuel set as an incompressible ideal gas and the energy equation solver off. Turning off the energy equation decoupled the flow and heat transfer calculations which helped to establish a stable flow field solution.

The starting sequence below is a sequential process where the average number of iterations at each setting are shown in parenthesis. To start the solution, the domain was first initialized to the UCC inlet. After Fluent[®] initialized the flow field of the domain, a tangential velocity value was prescribed by patching cells within the cavity section and setting a single velocity component to the cells. For this analysis, the core is along the Z direction; therefore, the tangential velocity was set by patching a tangential speed in the X direction.

Once a stable first-order reacting solution was reached, the spatially discretized equations were set for second order. The amount of iterations spent on each sequence depended on the how long the scaled residuals took to reach a value of 1e-3. For some cases, more time was required before starting the next sequence. Before starting the second-order solution process, the cavity section was patched with an ignition source by creating a cell register and specifying a temperature source of 2000 K. Patching an ignition source in the cavity allowed the combustion process of propane to begin. Once a second order solution was established for each of the test cases, the solutions were then run to 20,000 iterations for convergence.

- First Order Solution

Initialize Flow (300 iterations)
Second-Order Pressure (200 iterations)
Fuel Mixture to Ideal-Gas (200 iterations)
Energy Equation ON (250 iterations)

- Second Order Solution

Second-Order Species (100 iterations)
Second-Order Turbulence Variables (200 iterations)
Second-Order Momentum (200 iterations)
Second-Order Energy (200 iterations)
Second-Order Density (200 iterations)

3.3 Computational Domain

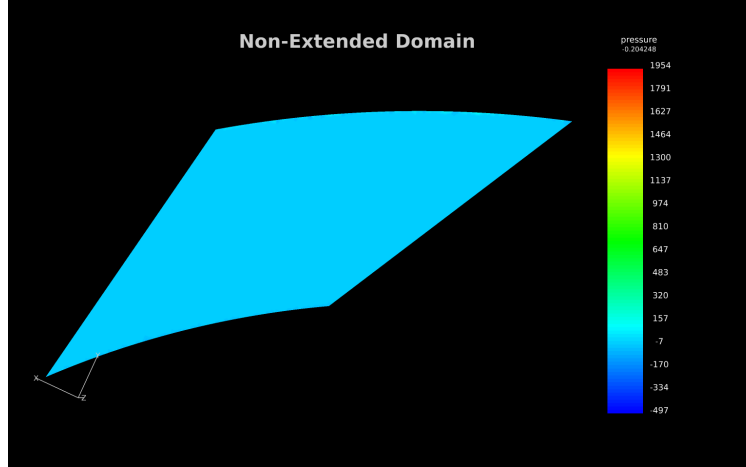
3.3.1 Boundary Conditions. The boundary conditions for a single periodic section included: two rotational periodic boundary faces, a pressure outlet, and four mass flow inlets for the air inlets (8 ports), fuel inlets (2 ports), main core flow inlet and film-cooling inlets along the suction side of the vane (6 holes for the front quarter section and 8 holes for the mid section). Below is a discussion of the application for each face on the computational domain.

3.3.1.1 Inlets. A variety of inlet boundary options are available within Fluent®. To introduce the fuel and air into the UCC, mass flow inlet boundary conditions were specified for the axial core inlet, air ports, fuel ports and coolant holes. The input values for each inlet sources can be seen in Table 3.3. In general, the mass flow inlet input values required the following to be specified: type of reference frame, flow rate, flow direction, static pressure, stagnation temperature, transport turbulence quantities, and chemical species mass or mole fraction. All inlet boundary conditions are set to flow normal to the boundary face except the core inlet source.

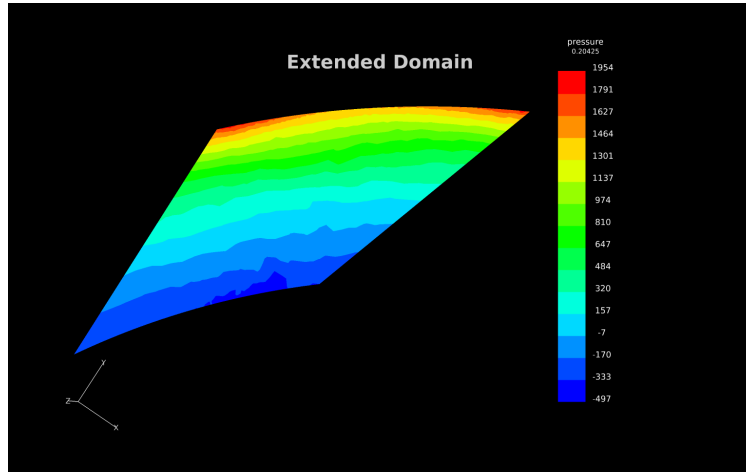
For the core flow, the direction of the flow is explicitly defined to enter the UCC at a 35° angle with respect to the axial axis. This angle is set in order to represent the expected flow direction off the compressor exit rotor.

3.3.1.2 Outlets. For the outflow condition, a pressure outlet boundary face is set for the domain exit downstream. To define the conditions for a pressure outlet, a gauge pressure and temperature must be specified. The gauge pressure, P_{gauge} , is the difference between the operating pressure, P_{OP} , and the atmospheric pressure P_{atm} . The analysis for this research correlates to a laboratory rig environment and so the operating condition is set at 101,325 Pa. A temperature value of 1200 K was also set for the outlet and is used when reversed flow occurs at the combustor exit. In all of the cases, reversed flow was reported by Fluent[®] as the solution was running. To avoid any influences of reversed flow on the solution, the computational domain was extended past the actual UCC exit. In the following section, the details of how much the domain was extended is described.

3.3.1.3 Domain Extension Study. The exit face of the computational domain was extended two inches from that of Bohan [6] in order to avoid disparities in static pressure values near the physical exit of the UCC. During the initial phase of this study, it was noticed that the static pressure at the UCC exit for a non-extended imposed 0 Pa value for the entire face. In Figure 3.3, the contour plot for the non-extended case and extended domain are compared to one another at the same location $Z=20.42$ cm. Here the contours show the non-physical condition at the UCC exit which in turn affected the temperature values. For the remainder of these computations, the domain was extended two inches beyond the plane interrogated as the exit plane.



(a)



(b)

Figure 3.3: Temperature contour plots of Baseline geometry with non-extended (top) and extended Domain (bottom)

3.3.1.4 Periodic Boundaries and Walls. To simplify the computational time, the entire UCC was divided into 20 sections. This was done by applying periodic boundary conditions to the side walls adjoining the combustor. Within Fluent[®], two options are available to create periodic boundary conditions by using conformal or non-conformal faces. For conformal faces, the periodic faces to be defined must have identical meshes. If the mesh nodes are not identical between the two

faces, a non-conformal periodic interface could be created. For this study, conformal meshes were used in defining rotational periodic boundary conditions.

For this study, the air inlet injectors are angled 35° to create the circumferential flow in the UCC cavity. Looking upstream of the UCC the flow occurs in a clockwise direction; therefore, the left periodic boundary face was set as the primary zone while the right periodic boundary face was set as the shadow zone. In Figure 3.4, an illustration is shown of the periodic boundary face definitions. For the remainder of the faces, non-porous wall boundary conditions are applied. For this analysis, adiabatic conditions are applied. Table 3.3 summarizes the input values for each of the boundary conditions. A complete diagram of the computational domain is shown in Figure 3.6.

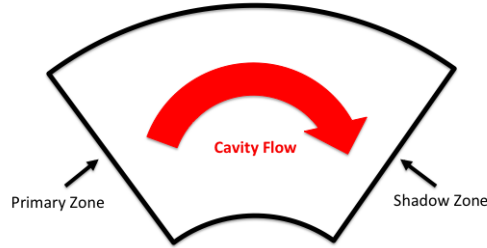


Figure 3.4: Flow Direction within Circumferential Cavity

Table 3.3: Fluent[®] Boundary Condition Inputs

Parameter	Flow rate (kg/s)	Temperature (K)	Gauge Pressure (Pa)	Tu (%)
Core Inlet	0.97	366	-	16
Air Inlet Ports	2.245E-1	366	-	2
Fuel Inlet Ports	3.18E-3	300	-	2
Coolant Injectors	M=1, 1.5, 2	366	-	1
Pressure Outlet	-	1200	0	-

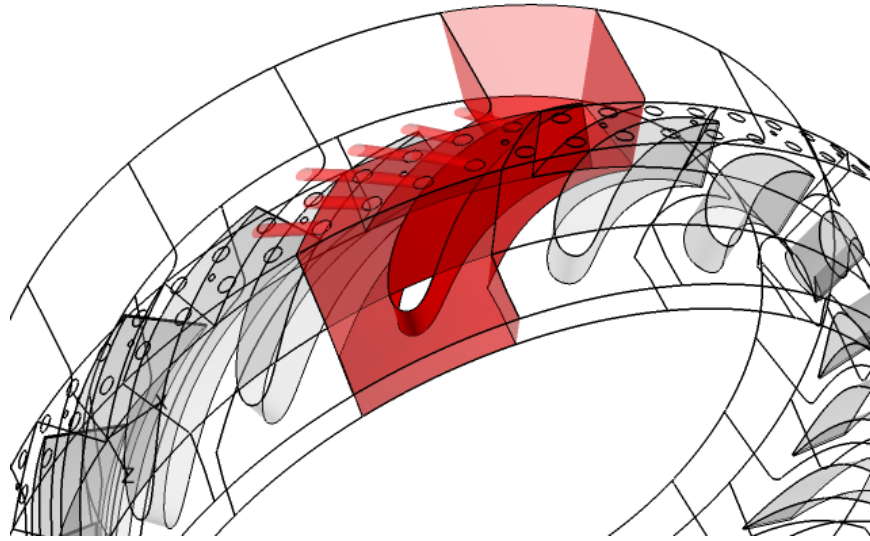


Figure 3.5: Sectional layout of periodic domain with respect to UCC annulus

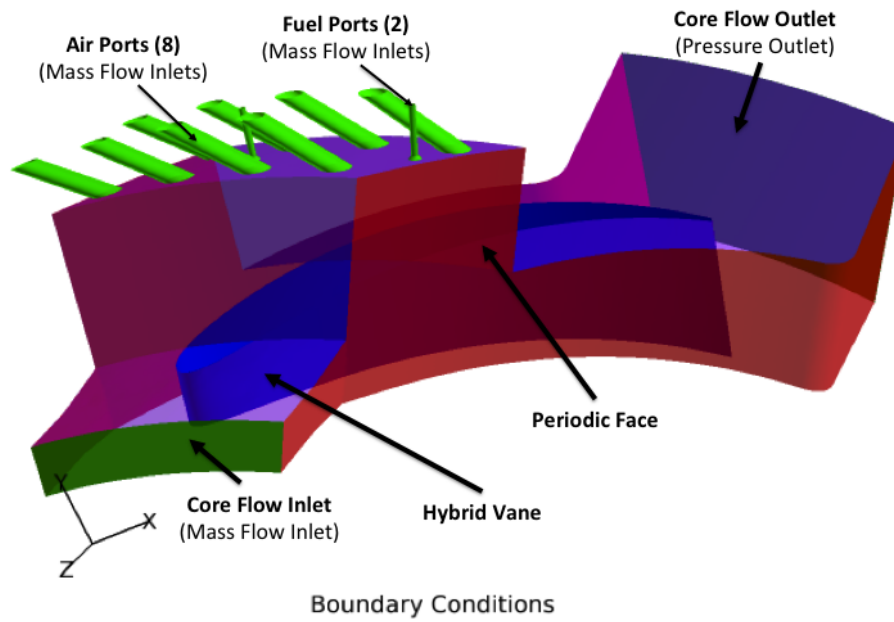


Figure 3.6: Computational Boundary Conditions for UCC

3.3.2 Grid Construction. The ability to simulate and predict the performance of an entire engine or certain engine components prior to building hardware is very cost effective. The reliability and accuracy of the simulation being largely dependent on the quality of the grid. For this analysis, Gridgen[®] software is utilized to construct an unstructured volume mesh of the UCC geometry. Three a priori grid quality metrics were used in constructing a computational domain for this effort: equiangle skewness, equivolume skewness and smoothness of neighboring cells. A two step process was used to maintain a high quality grid. First, for the faces that define the volume of the grid, a minimum equiangle skewness greater than 25° is targeted and monitored by using a histogram method. After ensuring the faces meet the 25° minimum equiangle criteria, the volume mesh is generated. Anisotropic tetrahedral cells with an initial spacing of 0.2 mm at a growth rate of 1.1 were used to capture the flow features in the viscous sublayer which resulted in a Y^+ range of 30 - 100.

3.3.3 Grid Quality. The final step prior to reading the volume grid into Fluent[®] involved checking the volume grid quality. After creating the volume mesh within Gridgen[®], Pointwise was utilized to obtain a grid quality score and visualize regions of poor quality cells. Within Pointwise [23] an average grid quality score was given between a 0 (good) to 1 (bad) scale and is based on Fluent's grid quality metrics. The two a priori grid quality metrics checked for the volume meshes were equivolume skewness and equiangle skewness of each cell. The equivolume skewness calculated within Pointwise[®] represents the ratio of the cell's volume to an optimum equivolume cell. Equation 3.4 shows how the skewness is computed within Pointwise[®]. For grid quality scores closer to unity, the value corresponds to a poor quality grid, and based on Pointwise's recommendation scores were targeted for values below 0.8. [23]. On average, each of the grids scored 0.37 for both the equivolume and equiangle skewness. Obtaining even lower values was difficult because of the amount of faceting at the wall junctions. Table 3.4 summarizes the grid scores for each geometry tested.

$$Score_{equivolume,skew} = \left[\frac{Cell_{optimal} - Cell_{actual}}{Cell_{optimal}} \right] \quad (3.4)$$

Table 3.4: Pointwise Grid Quality Scores

Geometry Model	Equivolume	Equiangle
	Skewness Score	Skewness Score
Baseline	0.499	0.3707
Contoured Trench	0.3715	0.3708
Normal Hole	0.3698	0.3697
Hybrid Configuration	0.3700	0.4980

3.3.4 Grid Convergence and Independence Analysis. For this study, the volume mesh sizes ranged between 10 to 43 million cells. For each numerical analysis, the following convergence criteria is used: 1) all scaled residuals lower than 10e-4, 2) deviations of mass-weighted-averaged total pressure at the UCC exit must be < 1% over 500 iterations, and 3) deviations of mass-weighted-averaged total temperature at the UCC exit must be < 1% over 500 iterations. Initially the study was done on the in-house cluster at AFIT, and as the grids' size continued to grow, the computational time increased. For example, a 24M cell sized grid required 19 hours to complete 500 iterations once the desired solution setting was achieved. After running the test cases on the Raptor Clusters at DSRC, the average computational time for solution convergence ranged between 30 - 48 hours using 256 processing cores. Approximately 24,000 iterations were required in order to achieve the convergence criteria set for this study. At the UCC exit plane (Z=20.45 cm), the mass-weighted total temperature and total pressure values oscillated between 1-2% corresponding to +/- 30 K and +/- 2200 Pa, respectively. The following figures below capture the total temperature and total pressure mass-weighted exit values each of the cases.

For the grid independence study, the adaptation feature within Fluent was used to create a refined grid [12]. The gradient approach used to refine the coarse grid was based on the total temperature gradients for that particular case. For the baseline, normal hole and contoured geometries, the grids started off with roughly 10M cells.

After refining the mesh, the grids resulted in 25M cells. Comparing the total temperature and total pressure values at the exit of the UCC, the solutions varied by 3% and was considered to be grid independent.

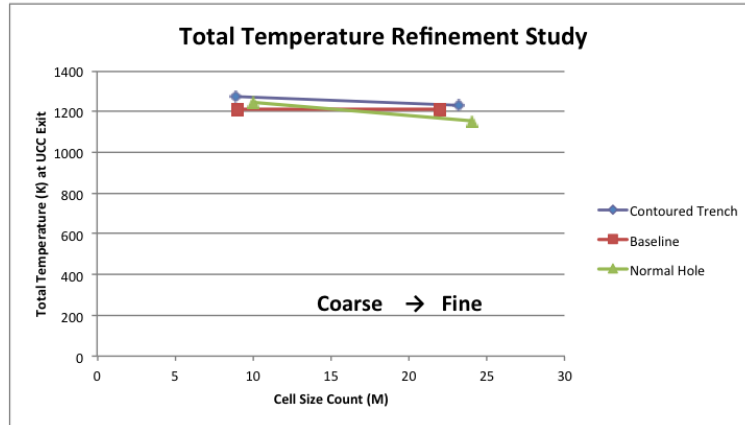


Figure 3.7: Grid independence analysis (total temperature value versus grid size variation)

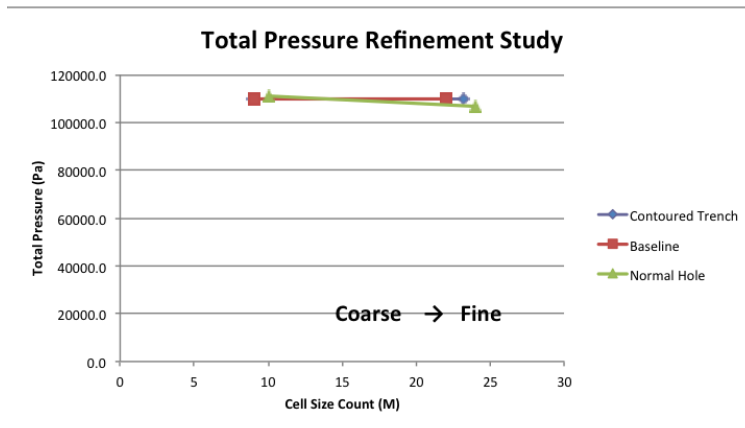


Figure 3.8: Grid independence analysis (total pressure value versus grid size variation)

3.4 UCC Geometry

The UCC geometry utilized for the film-cooling analysis was based on the full-scale model studied by Bohan [6]. The same cavity size and general flow path are the same as Bohan. A circumferential cavity with a 4.83 cm x 4.83 cm dimension wraps around the UCC where air and fuel inlet ports are situated around the circumference of the cavity. Air inlet ports are canted at 35° to establish the high-g combustion environment within the cavity section. A total of 160 air inlet ports are situated around the entire annulus of the UCC. From an anterior perspective of the UCC, the flow within cavity rotates in a clockwise manner. Fuel is radially injected into the cavity via 40 fuel ports positioned around the circumference of the cavity.

The solid model represented in this study includes 20 hybrid vanes situated below the UCC cavity. As mentioned in Section 1.2, the UCC becomes shortened axially from the combination of the combustor, compressor exit guide vane and turbine inlet guide vane. Combining the compressor exit guide vane and turbine inlet guide vane results in a hybrid vane that helps in guiding the exhaust fluid in the correct angle to the first turbine stage. For this analysis, a hybrid vane with an axial chord length of 12.2 cm, an inlet air angle, $\beta_1=35^\circ$, and an exit air angle, $\beta_2=70^\circ$, was considered. Figure 3.9 shows the source and design of the hybrid vane. The leading edge of the vane starts 3.34 cm from the start of the core inlet face. It is anticipated that the fluid exiting the compressor enters the UCC at a swirl angle of 35° . This core flow fluid continues downstream and is turned 35° in order to match a turbine inlet angle of 70° .

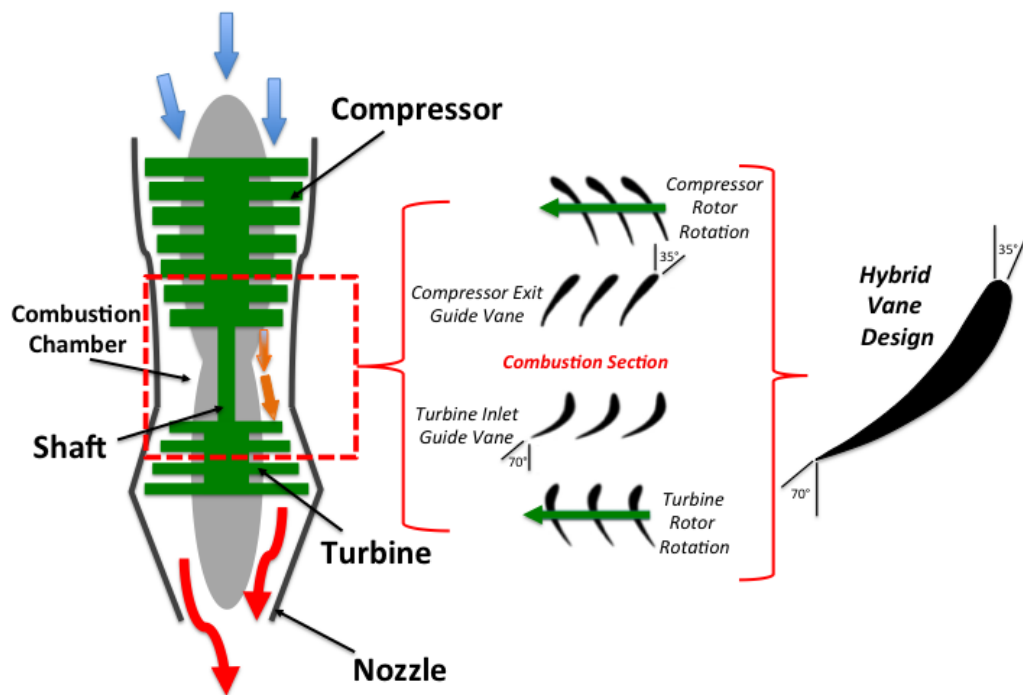


Figure 3.9: Hybrid vane design

3.4.1 Film-Cooling Geometry. As a starting point for the film cooling configuration, it was decided that the full-scale UCC model of Bohan [6] was to be investigated for film-cooling application. Again, this model is scaled to that of a nominal fighter sized engine. Figure 3.10 summarizes the dimensions of the UCC geometry. Here the inlet passage of the UCC begins with an inner radius of 29.9 cm and outer radius of 30.8 cm. The passage is then expanded at an angle of 7° resulting in a radius of 26.9 cm and 33.2 cm for inner and outer endwalls at the UCC exit, respectively.

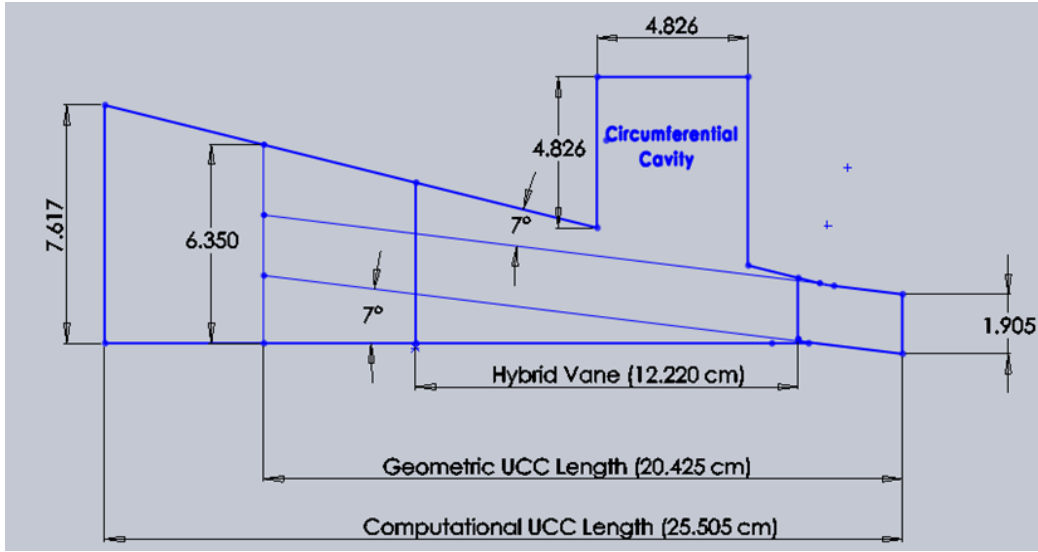


Figure 3.10: Geometric layout of the Ultra-Compact Combustor in x-y plane

3.5 Coolant Hole Geometry

A slotted coolant geometry is the ideal design for film-cooling, but because of its structural integrity in the presence of high thermal stresses it is not often used on turbine blades. The most common method is to use rows of holes in place of slots. One of the film-coolant geometries considered for this analysis was a row of normal holes distributed in the spanwise direction on the suction side surface of the vane. A single row of holes was placed on the suction side surface of the vane to establish a layer of coolant prior to the exhaust exhaust gases exiting out of the circumferential cavity section. In Figure 3.11, a layout of the normal hole configuration can be seen.

Further downstream, $55D$ from the first row of holes, a second row of holes are placed in order to continue the film-coolant distribution along the airfoil. Six holes are used for the first row of coolant holes and 8 holes are used for the second row because of the 7° taper on the airfoil. Holes are distributed with a pitch distance of $7.5D$ in the spanwise direction. Each hole is 0.51 mm in diameter and has a length of $5D$.

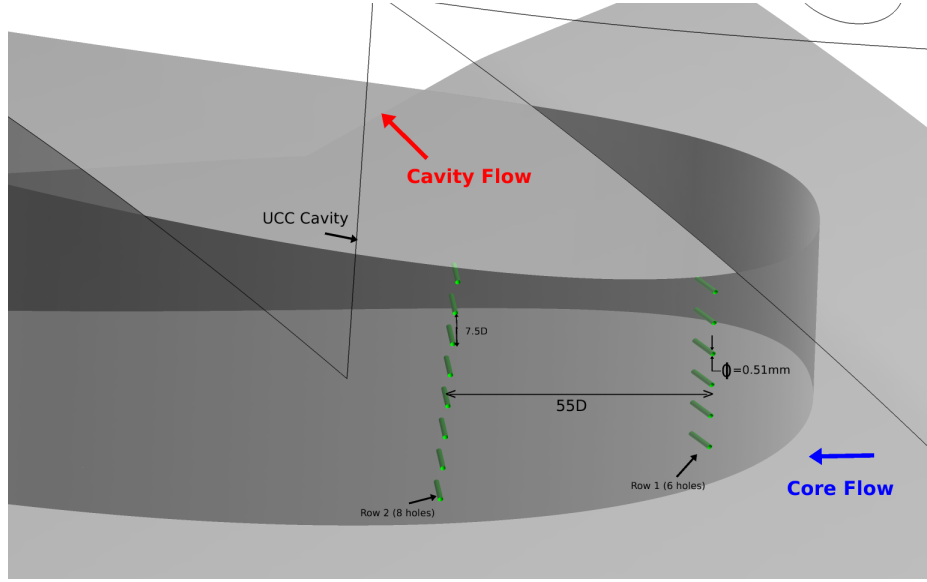


Figure 3.11: Schematic of normal hole coolant scheme along suction side surface of vane

For the second coolant scheme, a contoured-trench with discrete holes angled in the streamwise direction of the axial core flow path was modeled. The motivation behind this design was to create a film-coolant layer similar to a slotted geometry while maintaining structural support from the ribs formed by the coolant holes. This design was inspired by the trench work of Bunker [8]. The aft section of the trench is contoured to further encourage the coolant flow to remain attached to the vane surface. In this analysis, the depth of the trench was set at three diameters with a width of eight diameters. Similar to the normal hole geometry, two trenches were placed 55 diameters apart on the suction side surface of the vane with the first trench starting at the leading edge of the cavity. In Figure 3.12, the schematic shows the placement of the trenches on the suction side surface of the vane.

After analyzing the initial results of the normal hole and contoured trench designs, a final film-cooling design was proposed for the analysis. The final geometry analyzed was a hybrid coolant hole configuration. For this configuration, normal coolant holes and contoured trench holes were used. The trench design follows the reaction line of the baseline geometry. The trench design represents an extension to the ‘tiger claw’ design studied by Parks to effectively spread and migrate the hot gases from the circumferential cavity into the core flow [21]. The goal of this design is to create a film-cooling track for reactions to occur through the trench holes. The purpose of the normal holes is to create more mixing and further encourage the completion of the reactions. In Figure 3.13, the illustration shows a view of the hybrid trench design. Here the trench along the hybrid vane travels downstream and towards the ID endwall. The first trench begins at the leading edge of the cavity section, and the second row starts 44 diameters downstream and travels downstream approximately to the middle of the hybrid vane. The discrete holes within the trench are spaced with a pitch distance of four diameters. These holes are angled normal to the trench except for the last five holes. The last five holes are angled in more of a streamline direction in order to coerce the flow into the axial direction downstream. Outside of the trenches, normal holes are set along the trenches. For the normal holes, the coolant holes are angled 90° to the vane wall surface. The normal holes are spaced at a pitch distance of eight diameters apart from each other. Figure 3.14 illustrates the intended coolant and core flow path interaction.

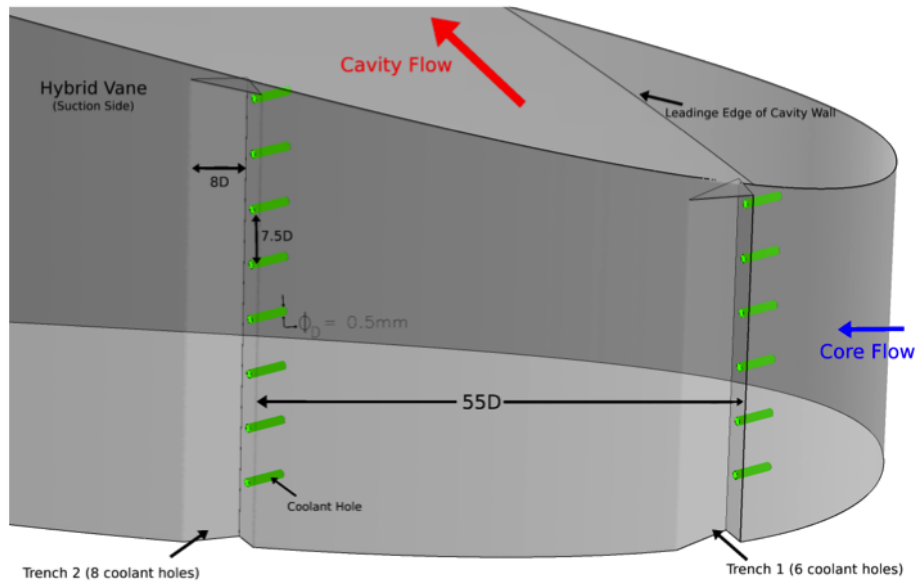


Figure 3.12: Schematic of contoured trench with discrete hole coolant scheme along suction side surface of vane

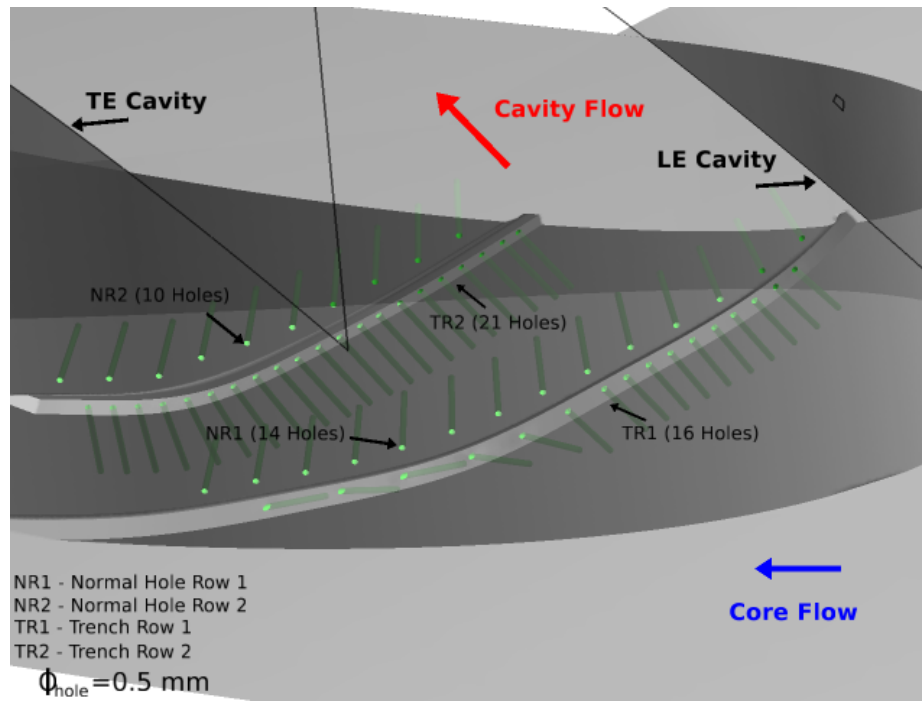
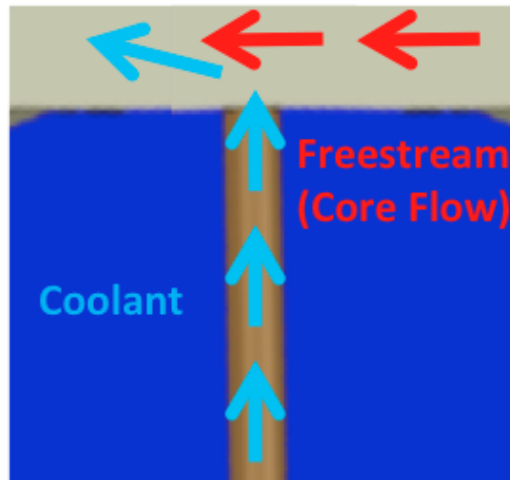
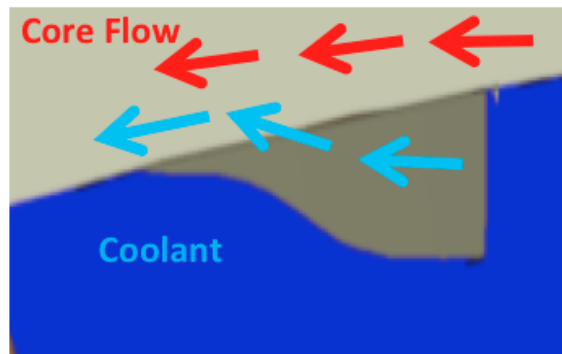


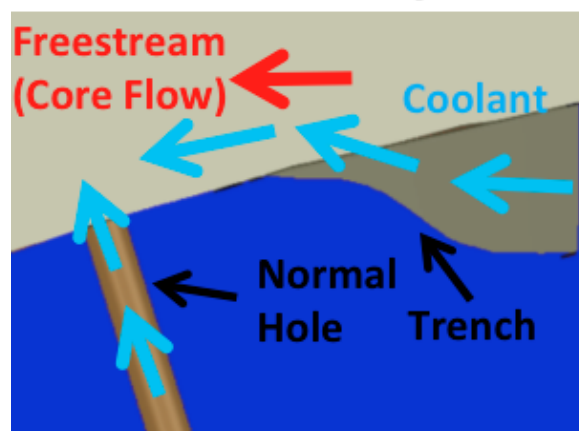
Figure 3.13: Schematic of hybrid coolant configuration along suction side surface of vane



(a) normal hole



(b) contoured trench



(c) hybrid geometry

Figure 3.14: Two-dimensional view of coolant hole configurations for a) normal hole, b) contoured trench with discrete holes and c) hybrid geometry

3.6 Test Conditions

For the film-cooling analysis, three test conditions were analyzed. The analysis consists of studying three blowing ratios for each coolant hole geometry. The blowing ratios ranged from $M=1$, 1.5 and 2. Based on the work of Goldstein et al. [14], their work investigated the effects of blowing ratios and found that for blowing ratios above 1.5 the film effectiveness decreased because of coolant separation. To gain an understanding of the effects on cooling effectiveness in the UCC when coolant separation occurs, a blowing ratio of $M=2$ was considered.

In a simplified film-cooling analysis, the freestream flow is straight forward to measure and set. For the UCC, the design involves two directions: cavity flow and core flow. Quantifying the freestream direction of the UCC application is rather complicated. For this analysis, the freestream is defined by the approach core flow. Knowing the cross-sectional area, mass flow rate and density of the fluid, the core flow velocity prior to the circumferential cavity can be determined. Equation 3.8 was used to compute the coolant mass flow rate for each coolant configuration. To arrive to this equation, the derivation first begins with the definition of blowing ratio in Equation 3.5. Knowing the mass flow rate of the core inlet and the cross-sectional area of the UCC right before the circumferential cavity section, ρ_{core} and U_{core} can be found from Equation 3.7. For this analysis, the mass flow rate per coolant hole was found and set at $6.55e-5$, $9.83e-5$ and $1.31e-4$ kg/sec.

$$M = \left(\frac{\rho_{coolant} \cdot U_{coolant}}{\rho_{core} \cdot U_{core}} \right) \quad (3.5)$$

$$\dot{m}_{core} = \rho_{core} \cdot U_{core} \cdot A_{core} \quad (3.6)$$

$$\dot{m}_{coolant} = \rho_{coolant} \cdot U_{coolant} \cdot A_{coolant} \quad (3.7)$$

$$\dot{m}_{coolant} = \left(\frac{\frac{\dot{m}}{A_{core}}}{M} \right) \cdot A_{coolant} \quad (3.8)$$

Based on the results, discussed later in Section 4.2, the contoured trench showed the highest heat load along the vane surface due to secondary reactions. In order to determine whether the increased heat loads are actually due to secondary reactions, a final test was conducted with N₂ as the coolant for the contoured trench design. Because N₂ is inert secondary reactions will not occur and will isolate regions of secondary reactions for the air coolant case. This last case was tested at a blowing ratio of M=2 and only for the contoured trench design. A summary of the test cases run for this effort is shown in Table 3.5.

Table 3.5: Test Matrix

Model	Run	Coolant
Geo 1	M=1	Air
Geo 1	M=1.5	Air
Geo 1	M=2	Air
Geo 1	M=2	N ₂
Geo 2	M=1	Air
Geo 2	M=1.5	Air
Geo 2	M=2	Air
Geo 3	M=2	Air

IV. Results

For this research effort, film-cooling was applied towards the Ultra-Compact Combustor and investigated. A baseline model with no film-cooling revealed that along the suction side vane surface extreme temperatures are predicted to occur within the UCC. To address this issue, two film-cooling configurations (trench design and normal hole design) were simulated and the effects of film-cooling were analyzed. From the results of these configurations, a hybrid film-cooling scheme was then investigated that includes both the trench and normal hole design aspects. Below are the discussions on the data collected for the film-cooling analysis for this research.

4.1 *Baseline Model*

A baseline model was established in order to have a standard to compare against for the film-cooling and Rayleigh studies. Recall that for the baseline model, a 20 hybrid vane count, fighter-sized UCC model was investigated. The numerical results show that extreme temperatures are predicted to occur on the suction side surface of the hybrid vane consistent with the work done by Bohan [6]. As the exhaust gases exit the circumferential cavity, the hot gaseous fluid rolls along the suction side surface of the vane and exits the UCC. In Figure 4.1, the temperature contour plot illustrates the location where the high heat loads occur for the baseline geometry. Burning at an equivalence ratio of 2.2 in the cavity, the local maximum temperature of 2350 K as shown in Figure 4.1 is expected along the reaction line formed by the cavity and core fluid interaction, and near the trailing edge a high temperature value of 2250 K is expected. The high temperatures indicated near the trailing edge of the airfoil suction side was the result of the incomplete radicals exiting the high fuel-to-air ratio UCC cavity and coming to completion within the core flow. The dividing line created by the hot cavity fluid and cooler core flow begin at the leading edge of the cavity and spans down the suction side surface and downstream of the vane reaching until it reaches the lower endwall. This line ends at approximately 50% of the chord length. Figure 4.2 clearly reveals a non-uniform temperature profile across

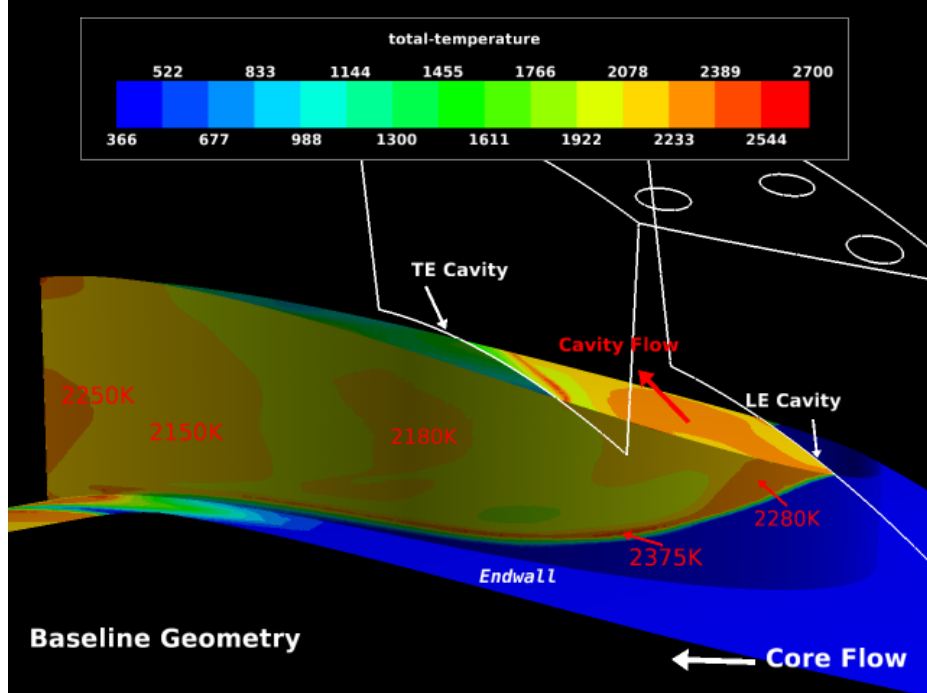


Figure 4.1: Total temperature prediction on Hybrid Vane

the suction side surface of the vane and displays the radial migration of the hot gases as they exit the circumferential cavity. On the pressure side surface, the vane remains cool which has guided this research to focus film cooling on the suction side surface only. In Figure 4.3, streamlines seeded within the cavity are shown and portray how the hot exhaust gases exits out of the cavity section. Here vortices are formed along the suction side surface spanning the vane and goes towards the lower endwall surface. Looking at Figure 4.3 again the local hot spots correspond to where the vortices curl back into the hybrid vane heating the surface to values above 2100 K.

At the exit of the UCC, the simulation predicts the flow to exit with a 0.28 Mach value and an area-averaged temperature value of 1601 K. The pressure loss through the UCC is calculated to be 10.5% with a total pressure value of 106,800 Pa at the exit. After taking the spanwise temperature averages at the exit, the baseline model has a pattern factor of 0.71 and a profile factor of 0.40. These values were calculated using Eq 4.1 and Eq 4.2. The equation represents the temperature spread at the UCC exit. Here $T_{4,max}$ is the maximum outlet temperature, T_{mr} is the

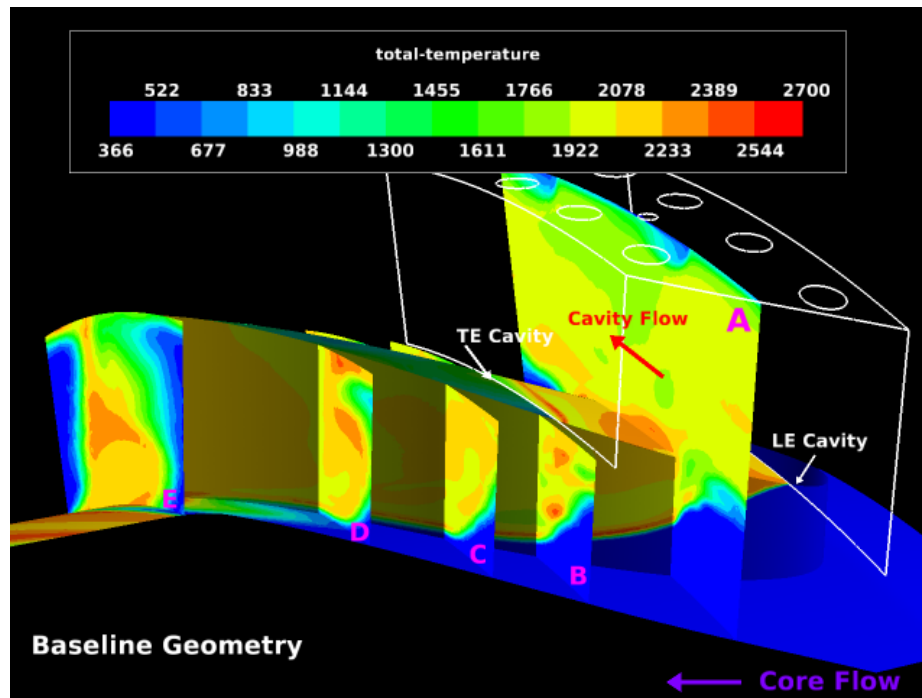


Figure 4.2: Radial temperature distribution through UCC

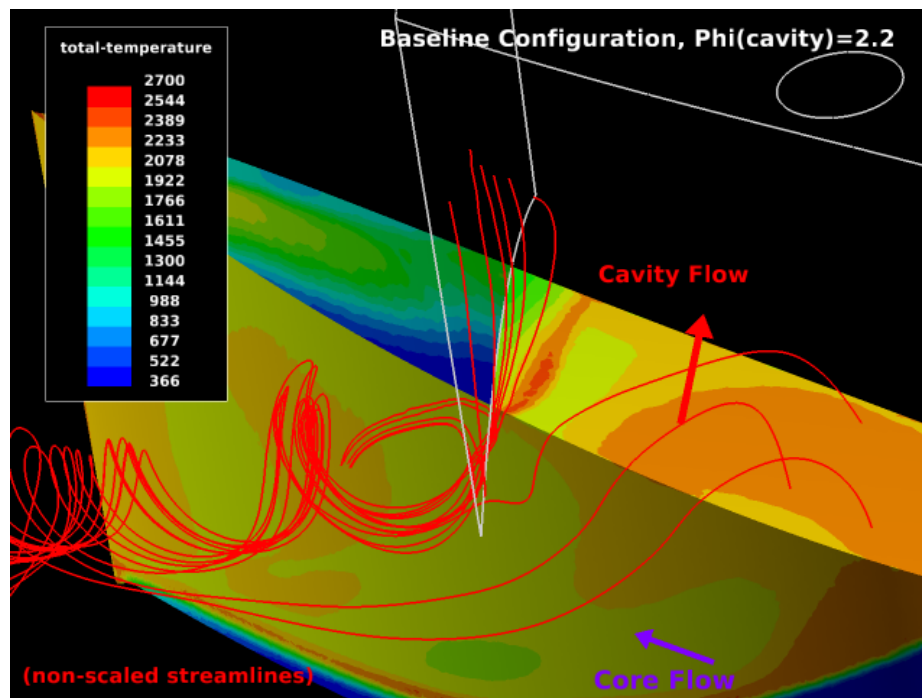


Figure 4.3: Streamline vortices formation from cavity section into core flow

maximum spanwise average temperature, and T_3 and T_4 are the mean inlet and exit temperatures, respectively. The ultimate goal is for T_{mr} and $T_{4,max}$ to be as close as possible to the average temperature at the exit.

$$PF_{pattern} = \frac{T_{4,max} - T_{avg}}{T_{avg} - T_3} \quad (4.1)$$

$$PF_{profile} = \frac{T_{mr} - T_4}{T_4 - T_3} \quad (4.2)$$

Based on the temperature contour plots of the baseline case, it is evident that the UCC requires a cooling scheme along the suction side surface of the hybrid vane. For this study, three film-cooling schemes were applied and the results for each configuration are discussed below. With unburned fuel exiting the circumferential cavity seen from the reactions completing downstream, additional heat release is likely to arise which has shown to be enhanced in the presence of additional oxygen from film-cooling holes [24]. The goal of this film-cooling study focuses on how to cool this new hybrid component in light of this knowledge.

4.2 Contoured Trench Results

For the first study, a cooling scheme consisting of a trench like shape design with axial holes feeding the trench was analyzed. Two rows of holes were positioned ahead of the UCC cavity and nominally at the mid-section of the cavity. An attempt was made to cool the surface by providing a film-cooling layer before the gaseous fluid exits the cavity keeping the vane surface cool.

4.2.1 Internal Flow Interactions. For all of the blowing ratio cases, the coolant ejected out of the trench and separated from the vane surface. For the first trench in each of the cases, the coolant ejecting out of the three coolant holes near the top of the vane traveled down the span of the vane, reaching mid-span before the 2nd trench while the bottom holes remained fairly linear in the streamwise direction shown in Figure 4.4. A slight change in position of the coolant ejecting out of the top

three holes was noticed as the blowing ratio increased. As it increased from $M=1$ to 2, the coolant traveled further away from the vane. Figure 4.5 captures the effect of increasing the blowing ratio and shows how the coolant moves away from the vane and towards the center of the vane passage. In this figure, the streamlines are colored differently for each of the blowing ratio conditions and were created starting within the coolant hole. Figure 4.4 also shows that for lower blowing ratios the coolant is pushed further downward towards the endwall.

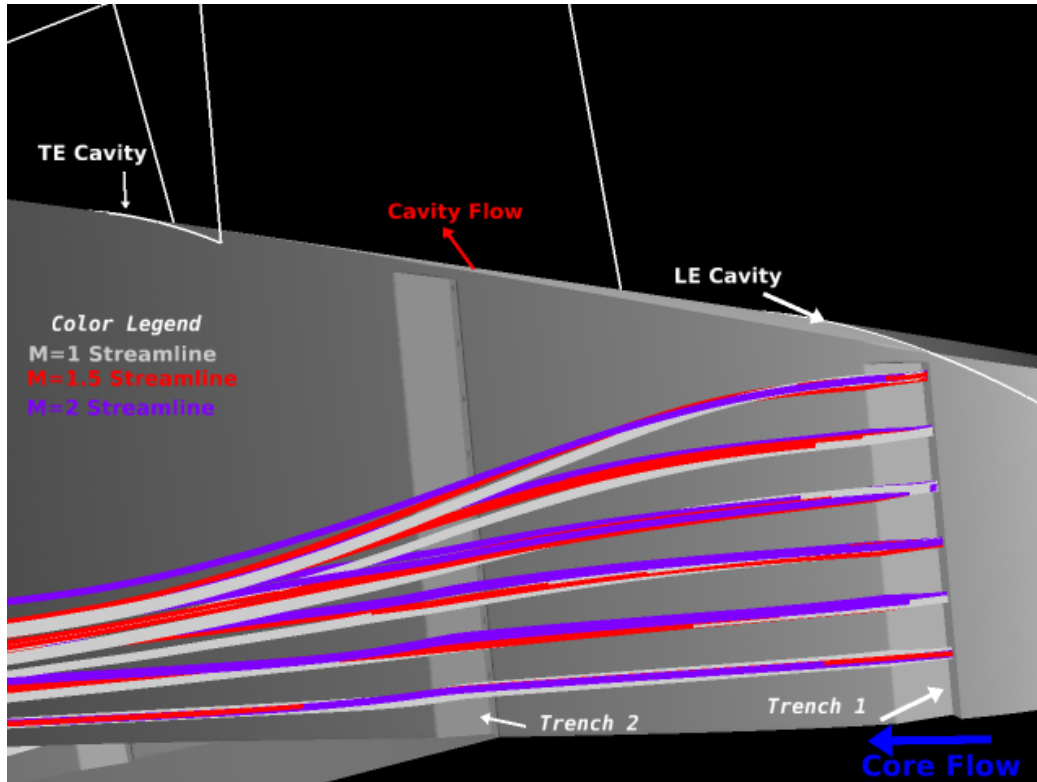


Figure 4.4: Side view of coolant migration out of trench 1 for $M=1$ (white), $M=1.5$ (red) and $M=2$ (purple)

For the second trench, the coolant behaved in a similar manner as the first trench. As the blowing ratio increased, the coolant pushed more towards the center of the vane passage. In Figure 4.6 and 4.7, a closer look of the coolant streamlines are shown depicting this behavior. As the coolant convected downstream, a vortex was formed along the suction side surface. This vortex was created by vortices that are shed out of the circumferential cavity. As an example, the streamline vortices of

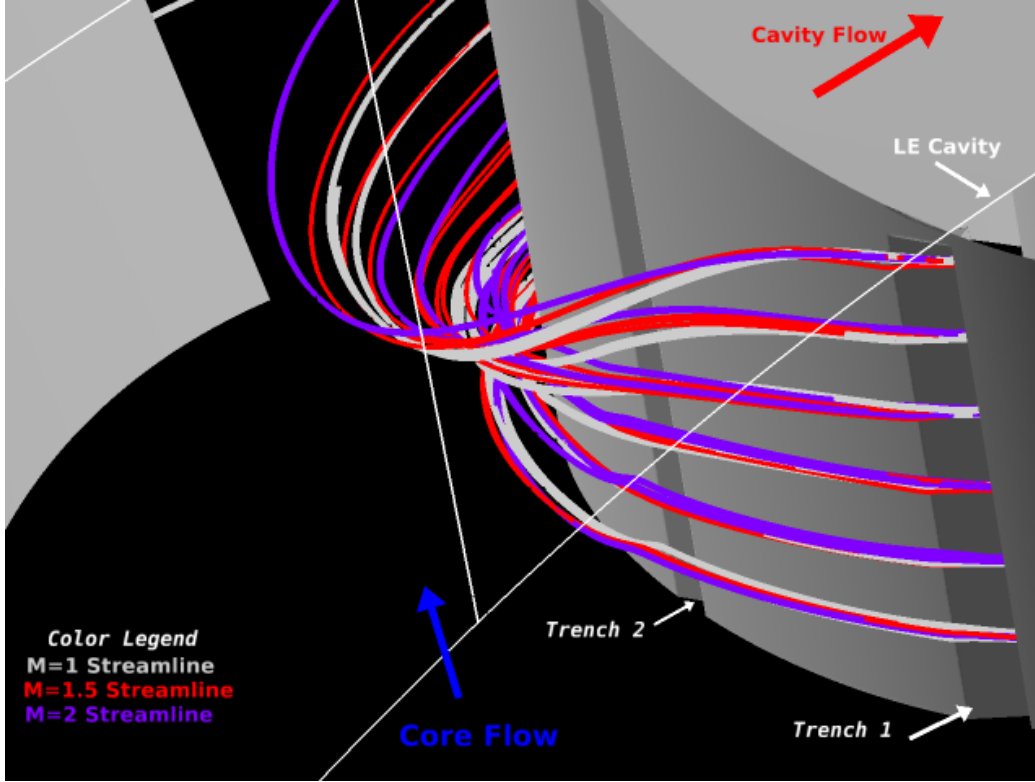


Figure 4.5: Isometric view of coolant migration out of trench 1 for $M=1$ (white), $M=1.5$ (red) and $M=2$ (purple)

the gaseous fluid (purple) exiting the cavity section is shown in Figure 4.8 for a $M=1$ test condition. As the exhaust exits the cavity the coolant fluid was pushed away from the vane surface degrading the effectiveness of film cooling for the contoured trench design. In Figure 4.9, the cavity and coolant streamlines for the second trench are depicted in solid red and blue, respectively, and set against the temperature distribution predicted on the airfoil. The streamlines show that the exhaust gases in the cavity begin to migrate into the core flow starting at the leading edge of the cavity and travels down the span of the vane. The cavity fluid convected downstream towards the endwall reaching 40% of the vane height before the second trench. Past the second trench, vortices began to form close to the upper endwall and continued downstream. Figure 4.10 illustrates the coolant, core and cavity flow taking on the same vortical structure downstream of the UCC.

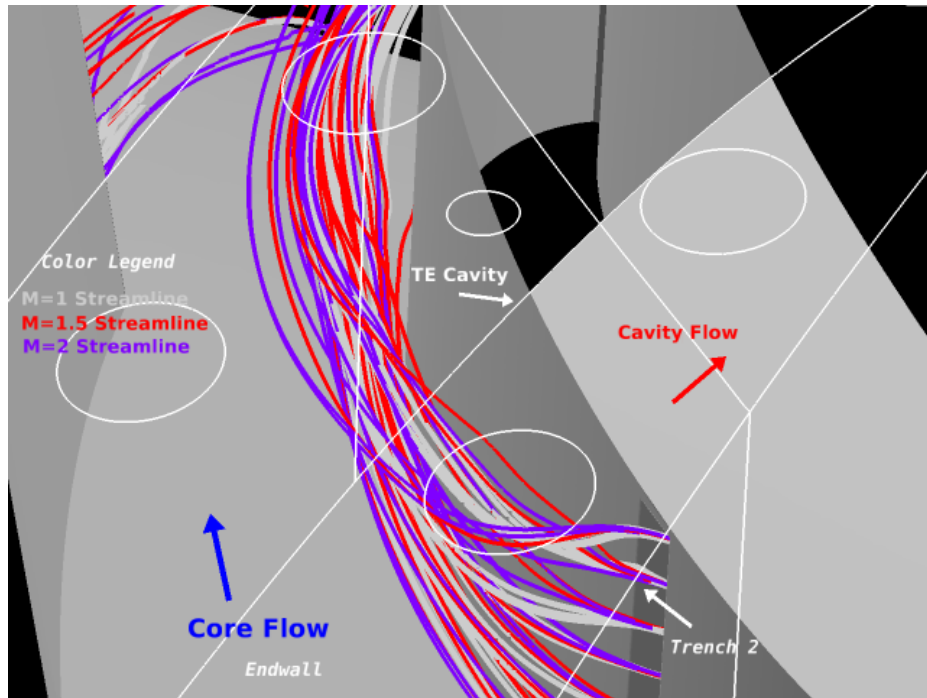


Figure 4.6: Coolant migration for $M=1$, $M=1.5$ and $M=2$ (isometric view)

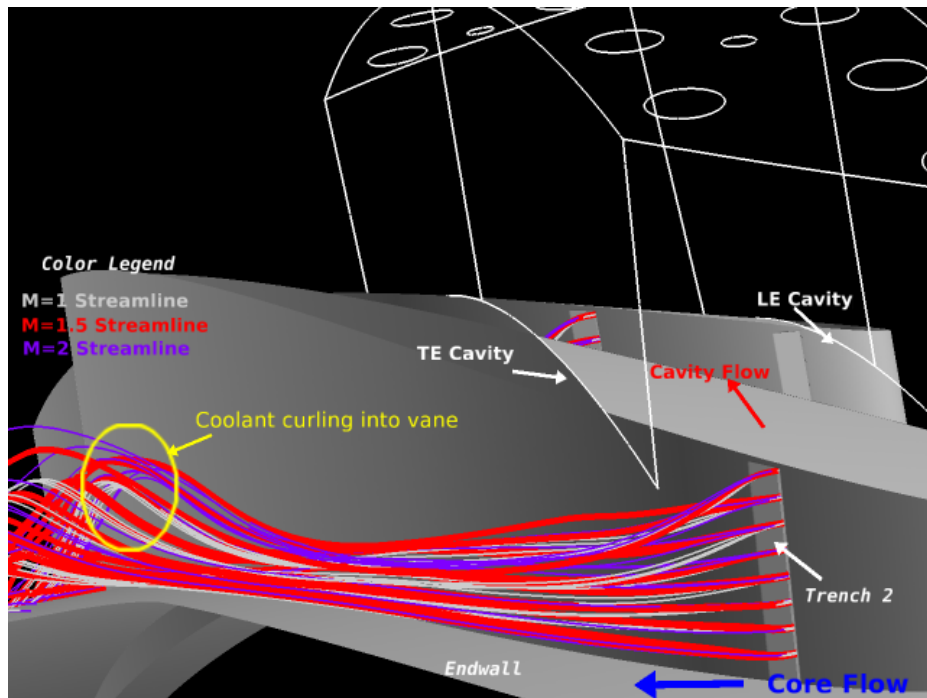
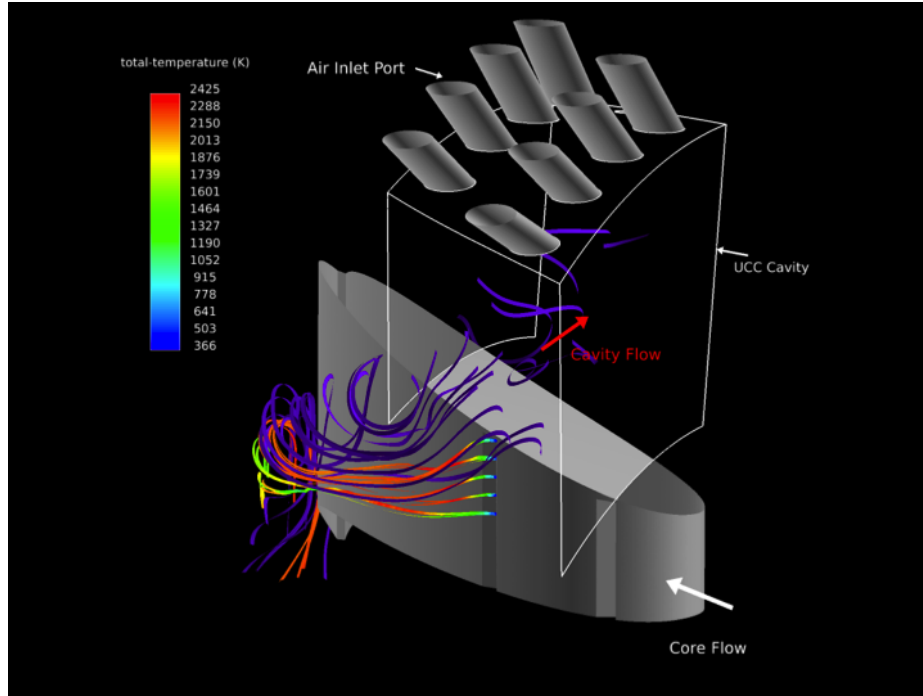
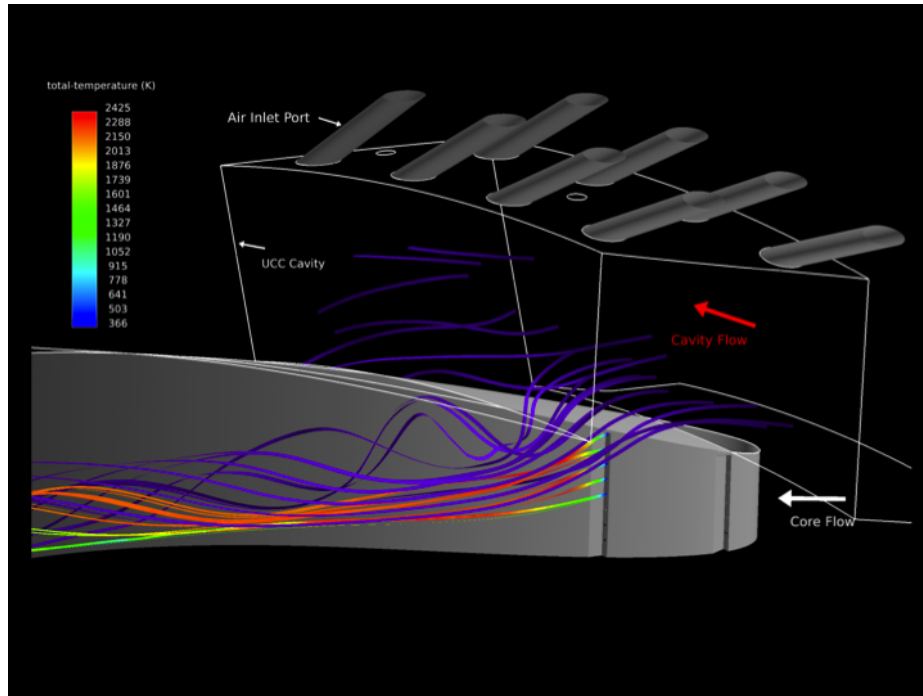


Figure 4.7: Coolant migration for $M=1$, $M=1.5$ and $M=2$ (side view)



(a)



(b)

Figure 4.8: Streamline patterns of cavity flow (purple) and 2nd row coolant flow (temperature scale)

Figure 4.9 is an additional streamline view for $M=1$ case set against the predicted temperature profile of the hybrid vane. From this one can see that the high heat loads corresponded to where the cavity fluid interacted with the coolant ejecting out of the holes. Figure 4.10 illustrates how the core flow interacts with the flow of the cavity fluid and coolant. Here the illustration shows that between the vane surface and the coolant/core fluid is the cavity fluid.

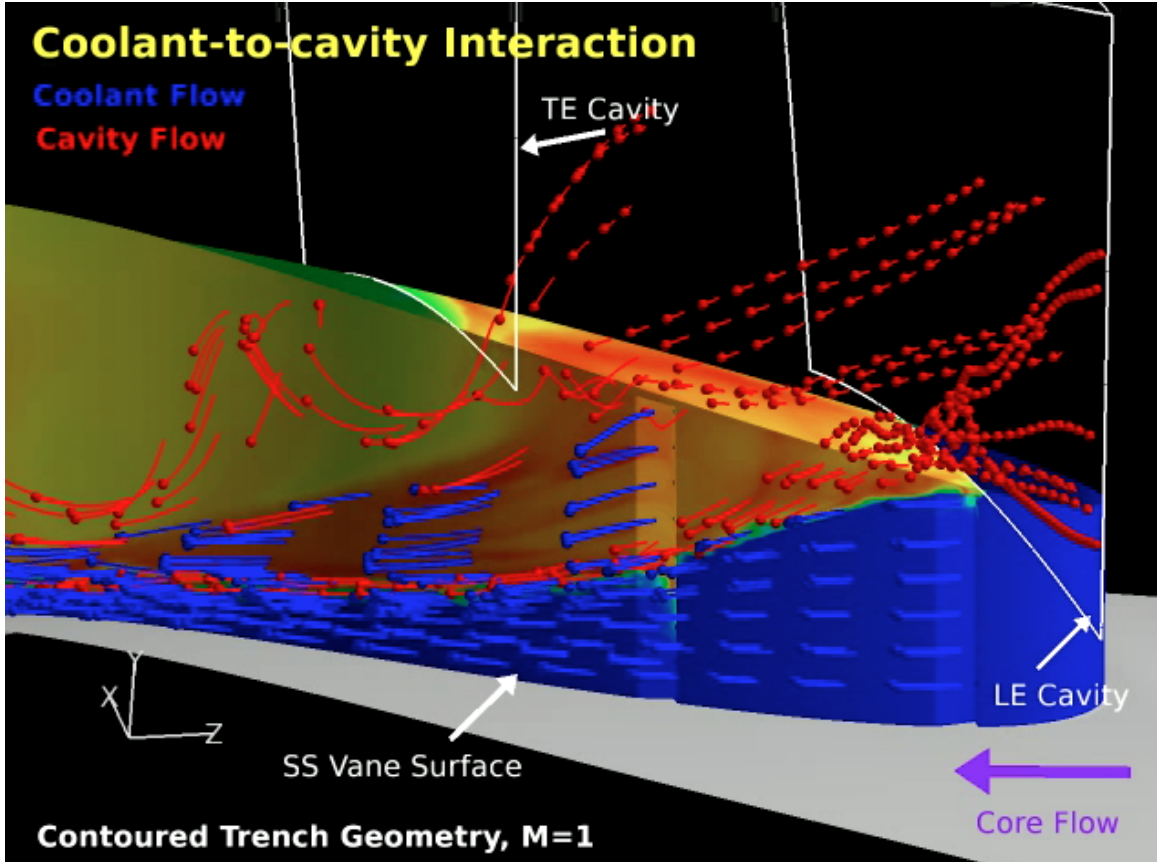


Figure 4.9: Streamline view of cavity and coolant flow interaction for $M=1$

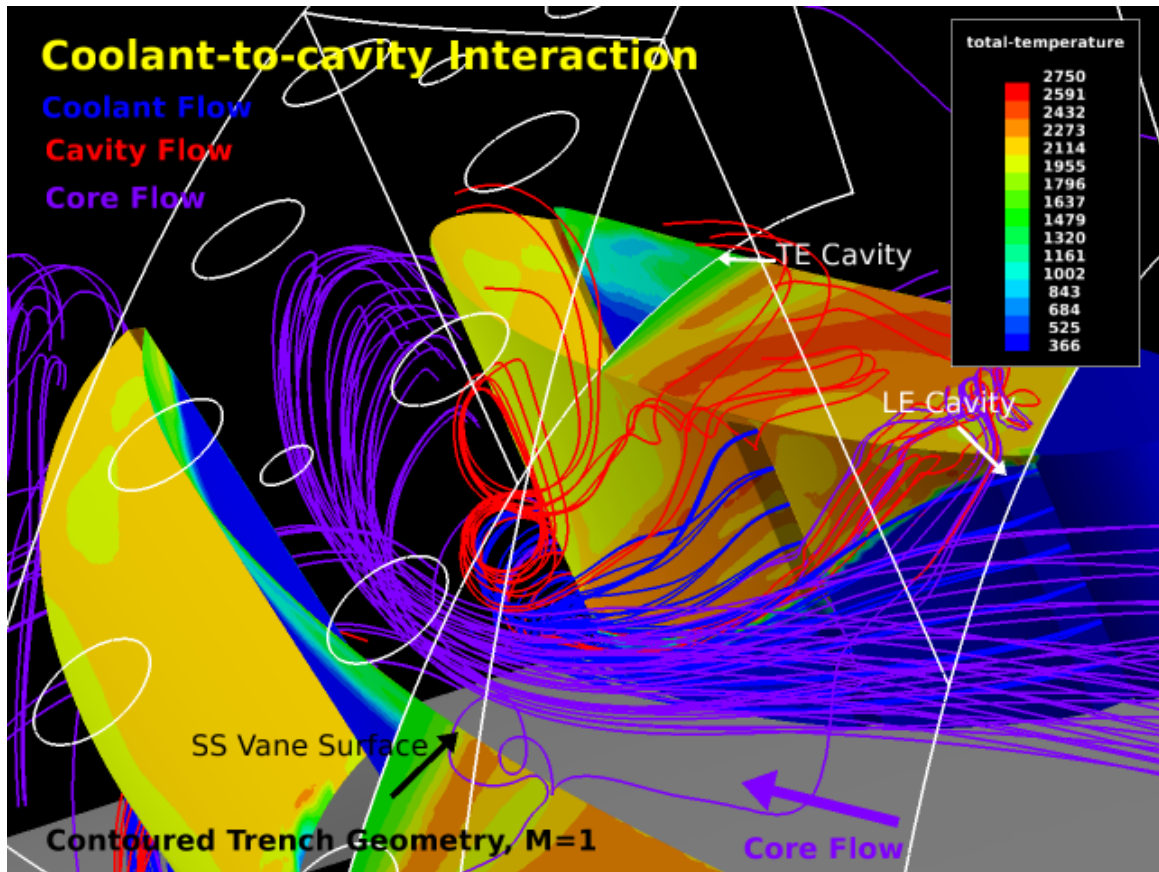


Figure 4.10: Streamline view of core, cavity and coolant fluid interacting as they convect downstream for $M=1$

4.2.2 Temperature Distribution. In the next analysis, the temperature distribution across the vane was investigated. For the first case ($M=1$), Figure 4.11 shows higher heat loads 20-30% of the chord along the suction surface of the vane as compared to the baseline model in Figure 4.1. The values for contoured trench design were near 2500 K and imply that secondary reactions have occurred further upstream. Towards the 80% of the chord the temperature value decreases from 2150 K to 2100 K, showing a 2% improvement in temperature reduction.

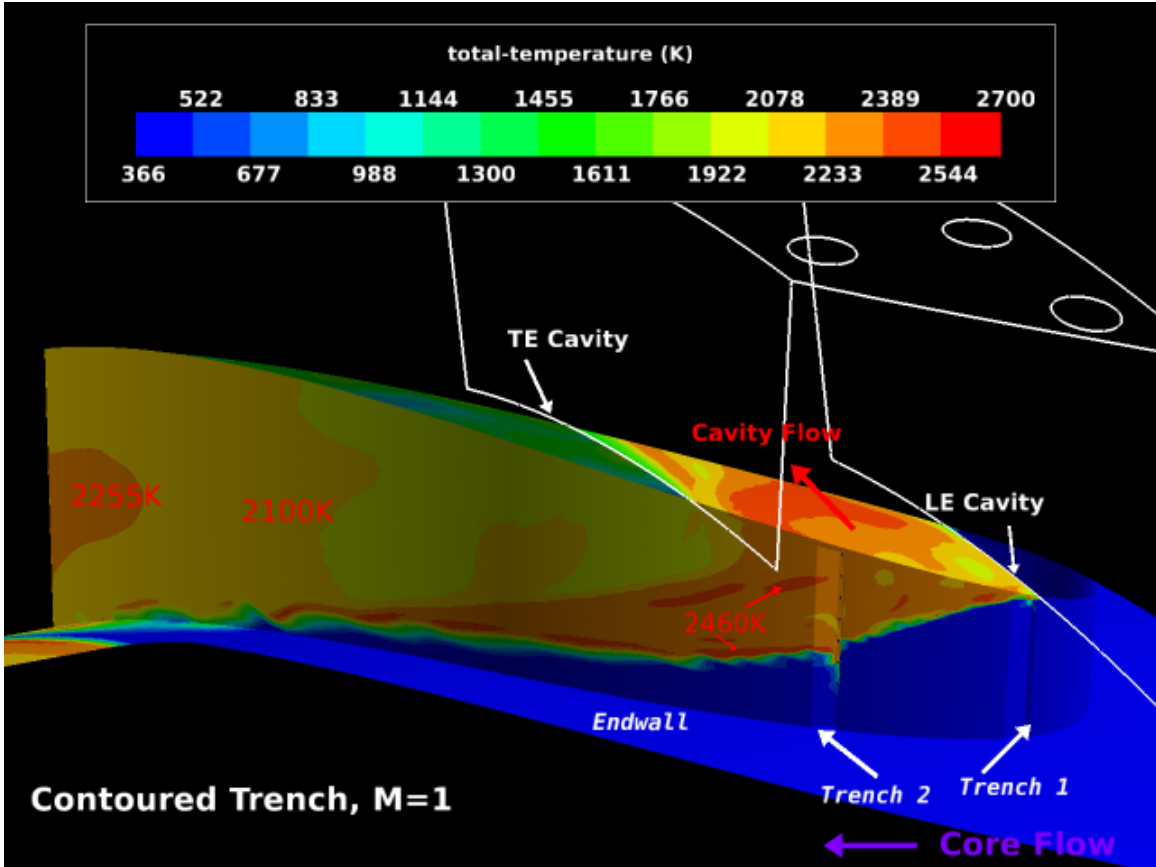


Figure 4.11: Airfoil temperature distribution for Contoured Trench Design ($M=1$)

Increasing the blowing ratio to $M=1.5$, the heat loads at the top of the vane right below the trailing edge section of the cavity were reduced in comparison to the $M=1$ case. Figure 4.12 shows the heat loads were more concentrated near the coolant holes. Right past trench one a temperature value of 2440 K was noticed. This behavior would be expected, as more oxygen is available for secondary reactions to

occur. For the $M=2$ condition, a thicker heat band was noticed along the reaction line separating the hotter and cooler region. In Figure 4.13, the value of this band is 2500 K. Again, the heat load at 80% chord of the vane is lower than the baseline geometry.

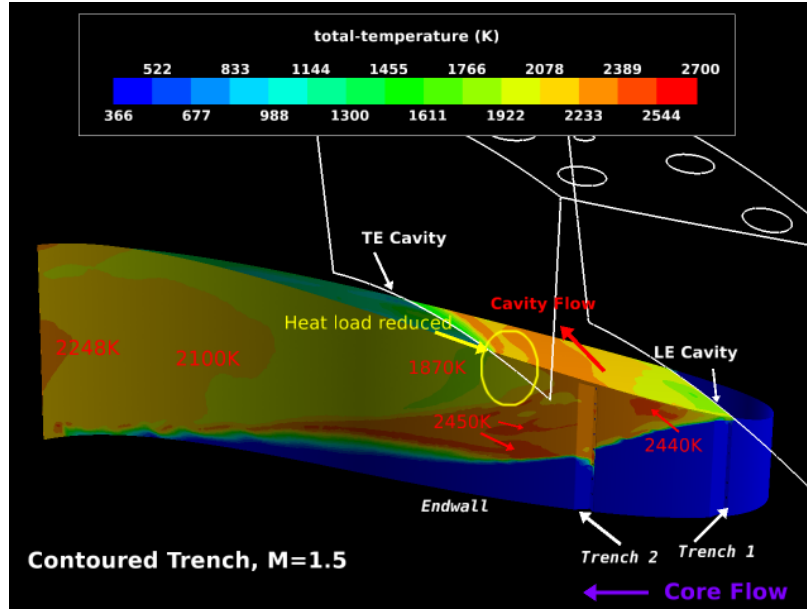


Figure 4.12: Airfoil temperature distribution for Contoured Trench Design ($M=1.5$)

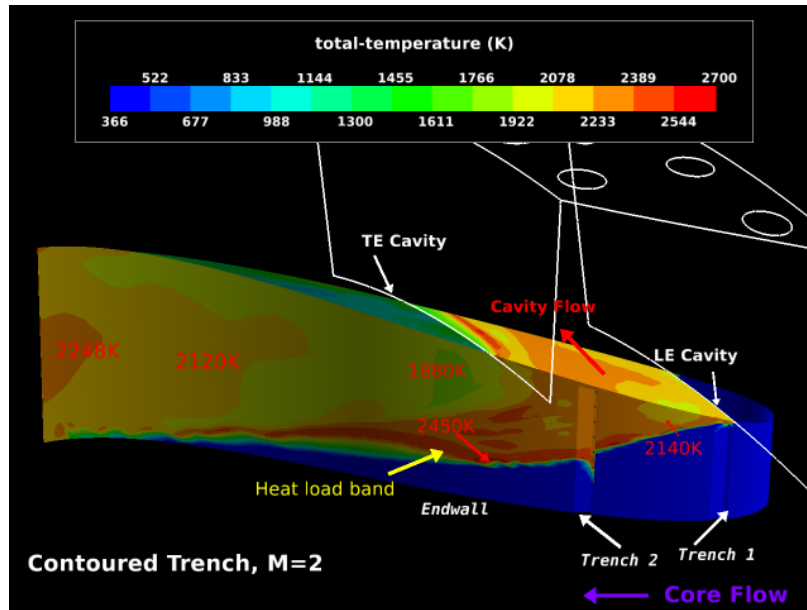


Figure 4.13: Airfoil temperature distribution for Contoured Trench Design ($M=2$)

To determine whether in fact the increased heat loads were due to secondary reactions, a single test case using N_2 coolant was conducted for a blowing ratio of $M=2$. Since nitrogen is an inert gas, this test case helped to isolate secondary reactions. Figure 4.14 illustrates the temperature distribution of the hybrid vane using N_2 coolant. Here the illustration shows that near the coolant holes the temperature value is 1730 K. Comparing the temperature profile of the N_2 case to Figure 4.12, it gives reason that the increased heat loads are due to secondary reactions when using air.

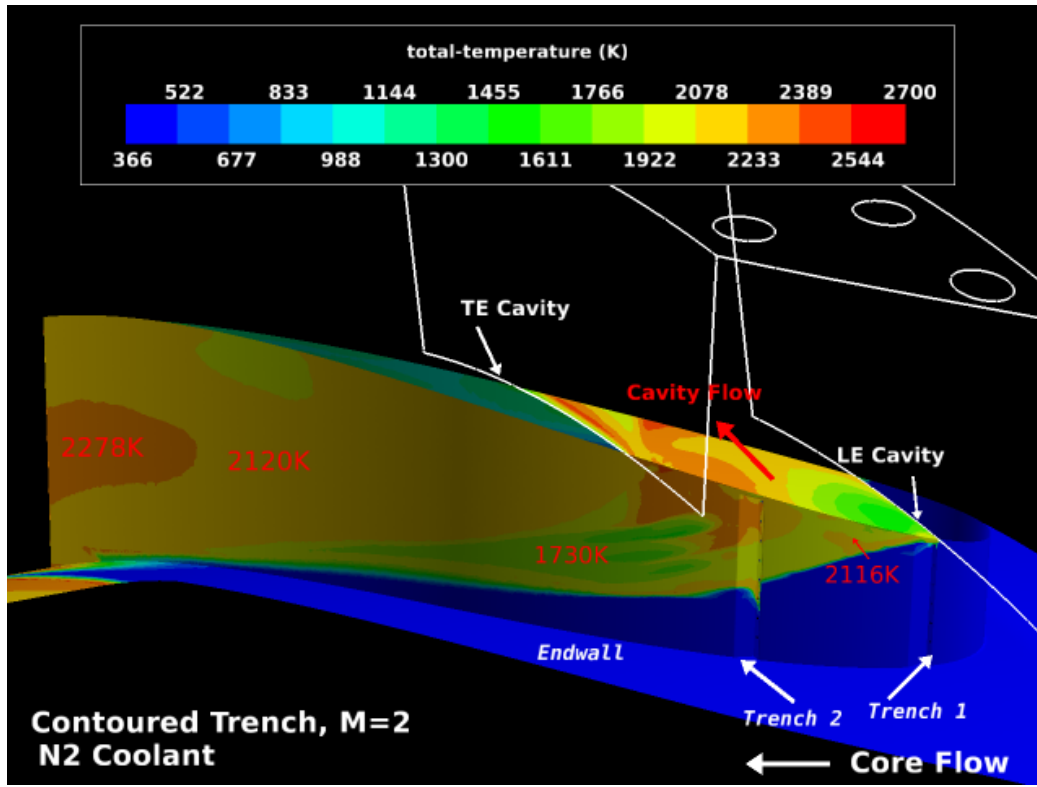


Figure 4.14: Airfoil temperature distribution for Contoured Trench Design ($M=2$) using N_2 coolant

Figure 4.15, 4.16, and Figure 4.17 show temperature contour planes made normal to the axial flow. The locations of planes A, B, C, D and E correspond to $X/D=40, 100, 130, 165,$ and 220 distances away from the leading edge cavity where the diameter for these positions is 0.5 mm. From Figures 4.15-4.17, plane B shows that as blowing ratio was increased more reactions were occurring upstream as shown

in the radial growth (normal to the vane surface) of the heat load in this plane. Continuing to the next contour plane C, 30 diameters downstream, it is interesting to note that in the radial direction away from the vane surface the reaction process is occurring off the wall. A similar trend was noticed at plane D where the cooler region (2000 K) spreads radially as the blowing ratio increases.

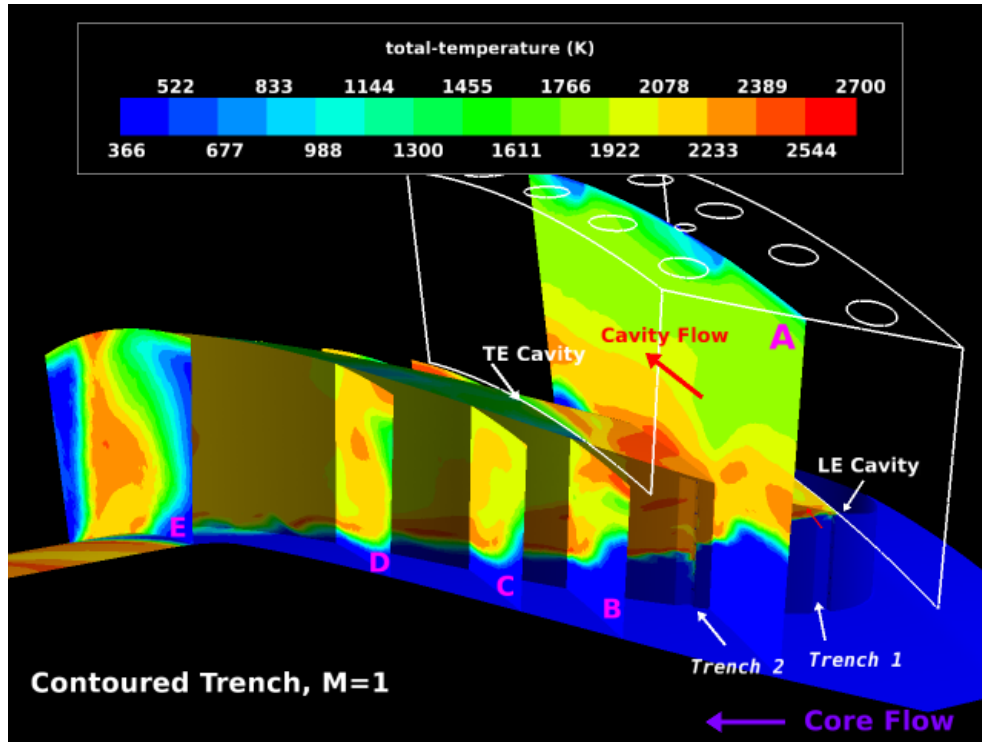


Figure 4.15: Radial temperature distribution for Contoured Trench Design (M=1)

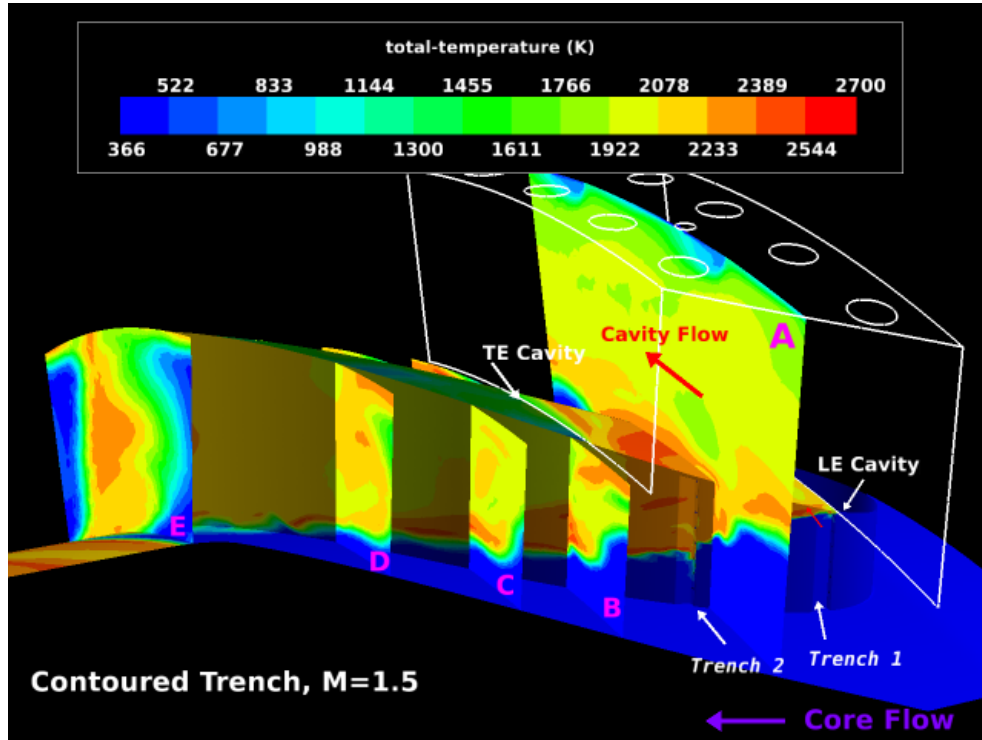


Figure 4.16: Radial temperature distribution for Contoured Trench Design ($M=1.5$)

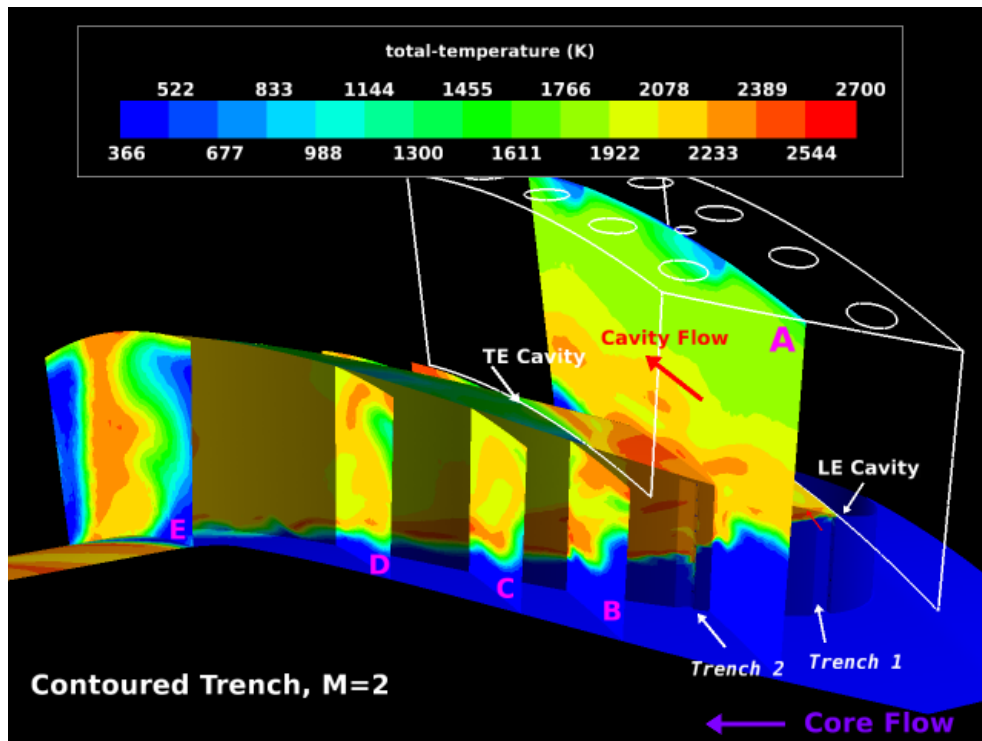


Figure 4.17: Radial temperature distribution for Contoured Trench Design ($M=2$)

In Figures 4.18-4.20, the temperature contours along the hybrid vane for the baseline model is shown for three spanwise locations. For each of these figures and the spanwise cut figures to follow, the spanwise location corresponds to distances of 30%, 50% and 75% of the vane height. Looking at the spanwise results of the contour trench design, Figures 4.21 - 4.22 are top-down views for each of the blowing ratios tested. The span distance starts from the inner endwall and goes up the span of the vane. From these illustrations, it is useful to understand whether reactions were occurring along the surface of the vane. By inspection of the contour plots in Figures 4.21 - 4.22, film-cooling caused secondary reactions to occur near the coolant holes which can be seen at 50% and 75% spanwise distances for the contoured trench design for all blowing ratios.

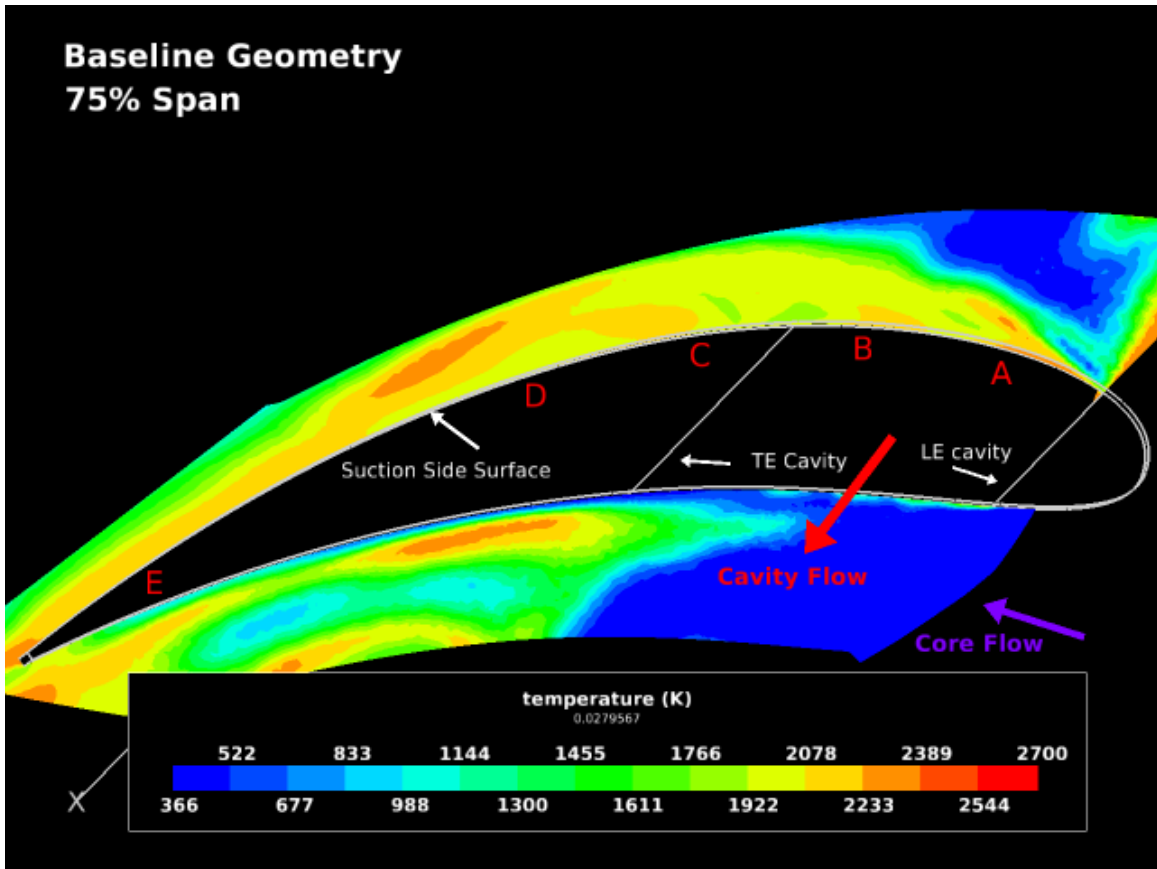


Figure 4.18: Spanwise Temperature of Baseline, 75% Span

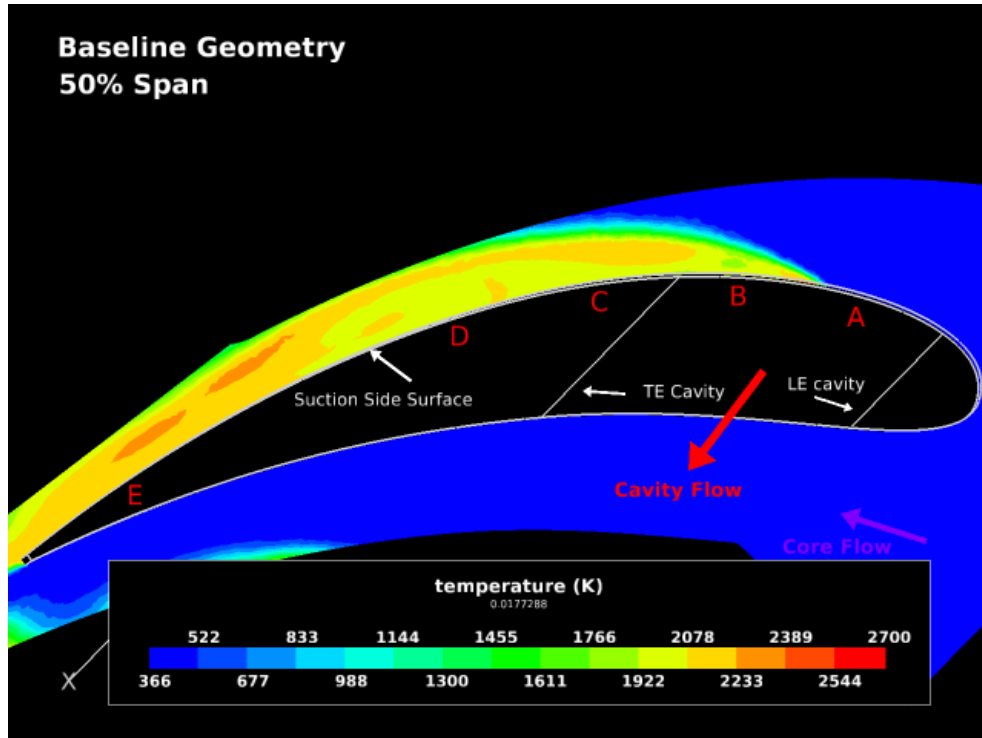


Figure 4.19: Spanwise Temperature of Baseline, 50% Span

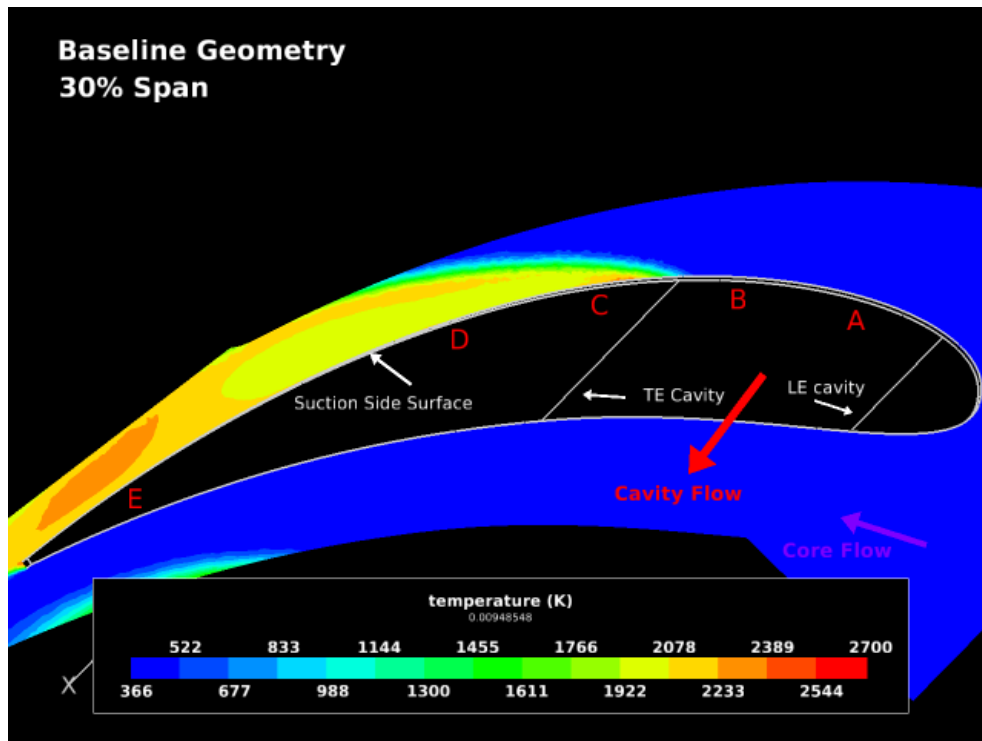
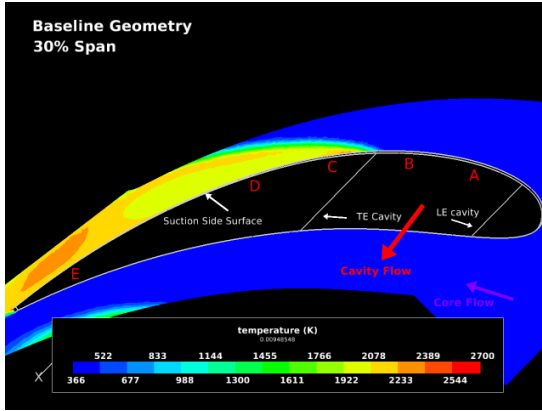


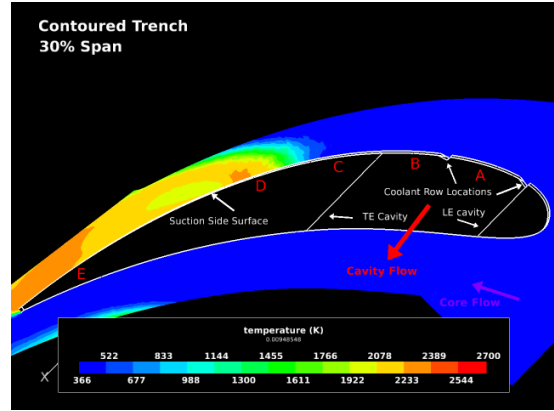
Figure 4.20: Spanwise Temperature of Baseline, 30% Span

Directly comparing the results at 75% span for the baseline case (Figure 4.18) to the contoured trench geometry for all the blowing ratios, Figure 4.21f reveals the presence of jet flames emerging from the cooling hole locations. These jets are consistent with the previous work of Polanka et al. [24] showing secondary reactions emerging from cooling holes subject to high fuel-to-air ratio environments. These two jets increase the temperature in this region of the vane. However, a reduction in temperature near the trailing edge occurred as the blowing ratio increased because of the upstream reactions. This was attributed to more of the unreacted radical species being consumed upstream just near the cooling holes versus further downstream. With secondary reactions occurring further upstream, the airfoil temperature values decrease as the reactive species complete their reaction.

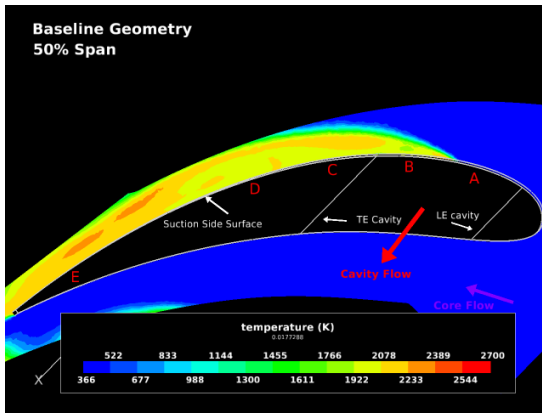
A significant benefit of the addition of film cooling was the marked delay of high surface temperatures along the suction surface at the lowest span. Comparing the baseline temperature distribution at 30% span (Figure 4.21a) with the same location with cooling (Figure 4.21b) reveals a 10% chord shift in the start of the high temperature along the suction surface. This location continues to slide downstream at higher blowing (Figure 4.22a and 4.22b). Clearly the addition of even a small amount of coolant along the surface upstream of the hot gas path has a significant effect. The coolant clearly serves to provide a buffer keeping the hot gases away from the wall, better than just the freestream fluid alone.



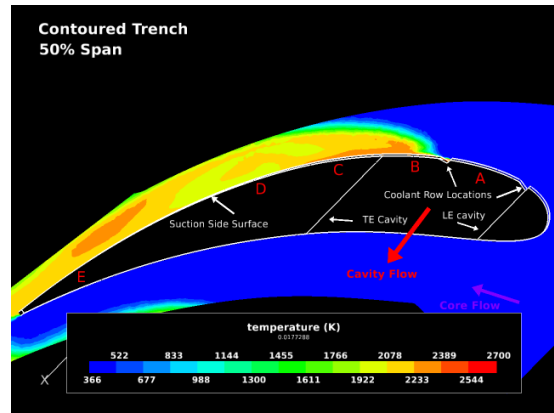
(a) Baseline 30% Span



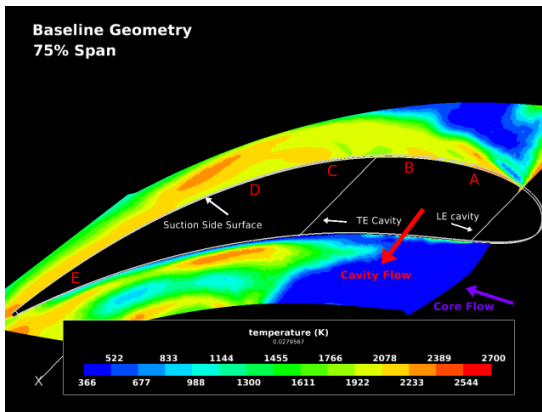
(b) Contoured Trench, 30% Span



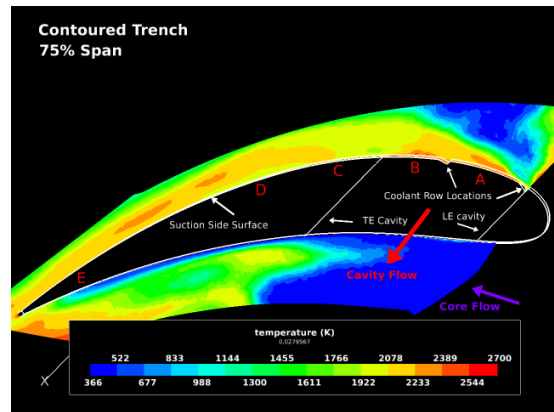
(c) Baseline 50% Span



(d) Contoured Trench, 50% Span

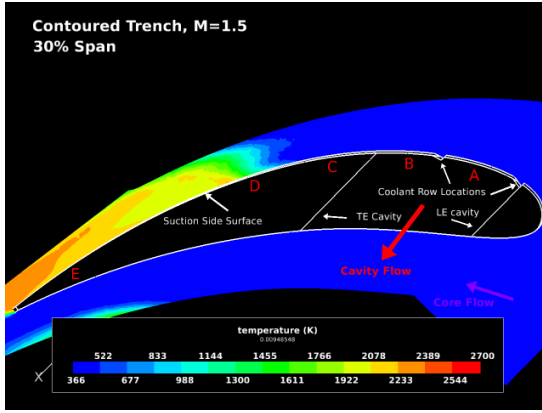


(e) Baseline 75% Span

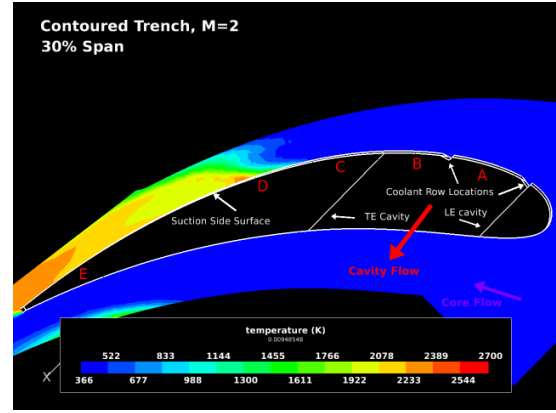


(f) Contoured Trench, 75% Span

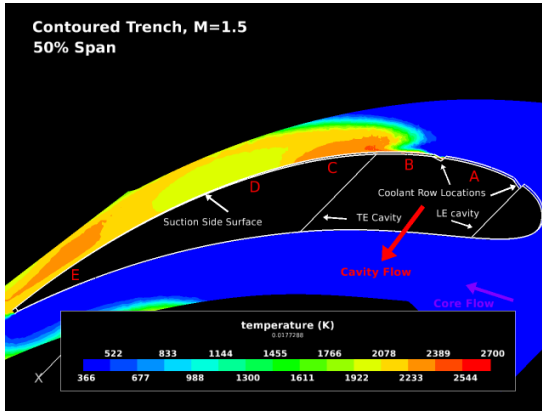
Figure 4.21: Spanwise Temperature of Baseline and Trench Design ($M=1$ case)



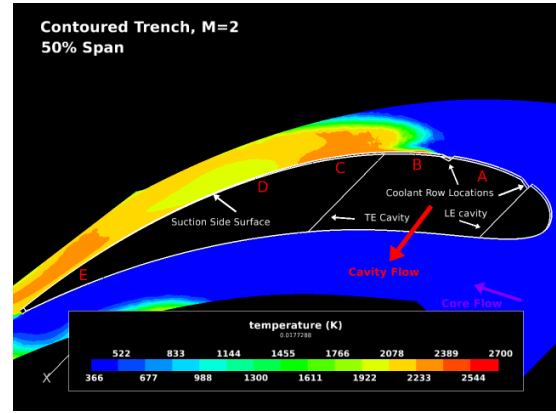
(a) Contoured Trench ($M=1.5$), 30% Span



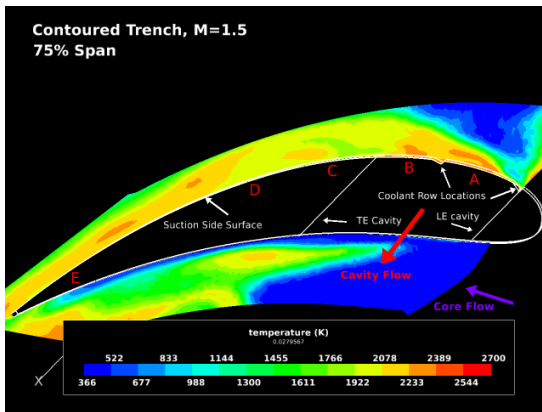
(b) Contoured Trench ($M=2$), 30% Span



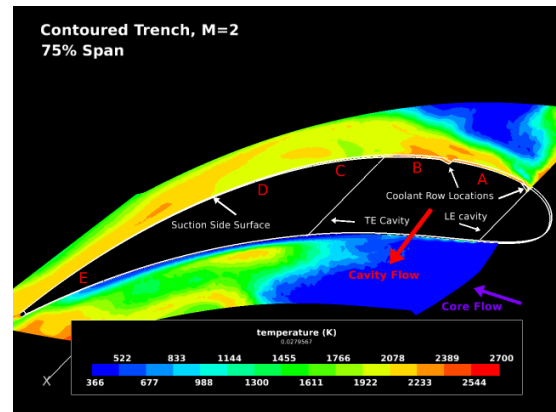
(c) Contoured Trench ($M=1.5$), 50% Span



(d) Contoured Trench ($M=2$), 50% Span



(e) Contoured Trench ($M=1.5$), 75% Span



(f) Contoured Trench ($M=2$), 75% Span

Figure 4.22: Spanwise Temperature of Contoured Trench for $M=1.5$ case (left column) and $M=2$ (right column)

4.2.3 *Exit Conditions.* A summary of the profile factor, pattern factor, Mach value and pressure losses are shown for the contoured trench design at the exit of the UCC in Table 4.1. At the exit of the UCC, a uniform temperature distribution is desired. In Figure 4.23, the spanwise-average temperature distribution for each case is shown. As the blowing ratio increases, the temperature distribution at the exit does not change. By applying film-cooling in the UCC, excess heating is expected at the lower endwall region compared to the baseline model. Figures 4.24 and 4.25 show that in the lateral direction the temperature distribution is fairly uniform.

Case	Mach	Profile Factor	Pattern Factor	$\frac{dp}{P}\%$
Baseline	0.280	0.40	0.71	10.5
M=1	0.308	0.72	0.79	9.1
M=1.5	0.306	0.72	0.78	9.1
M=2	0.307	0.72	0.77	9.3

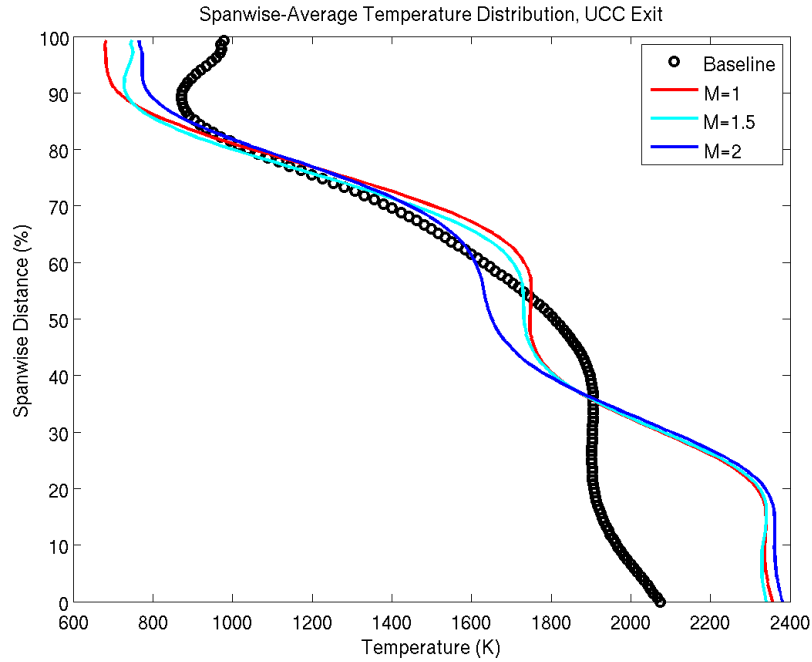


Figure 4.23: Spanwise-averaged temperature at UCC exit of the contoured trench design

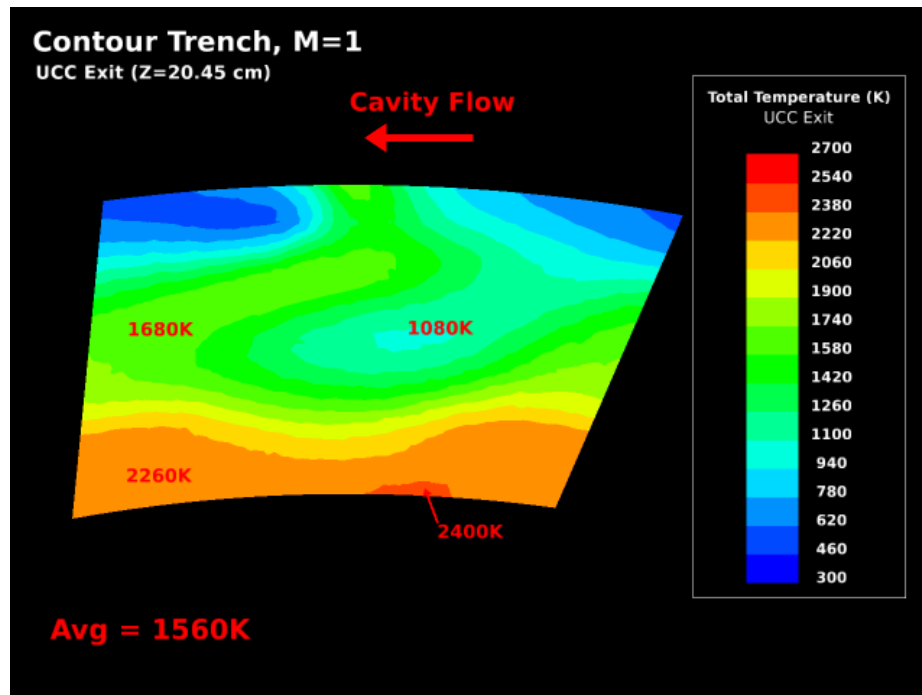


Figure 4.24: UCC Exit Temperature Contour M=1

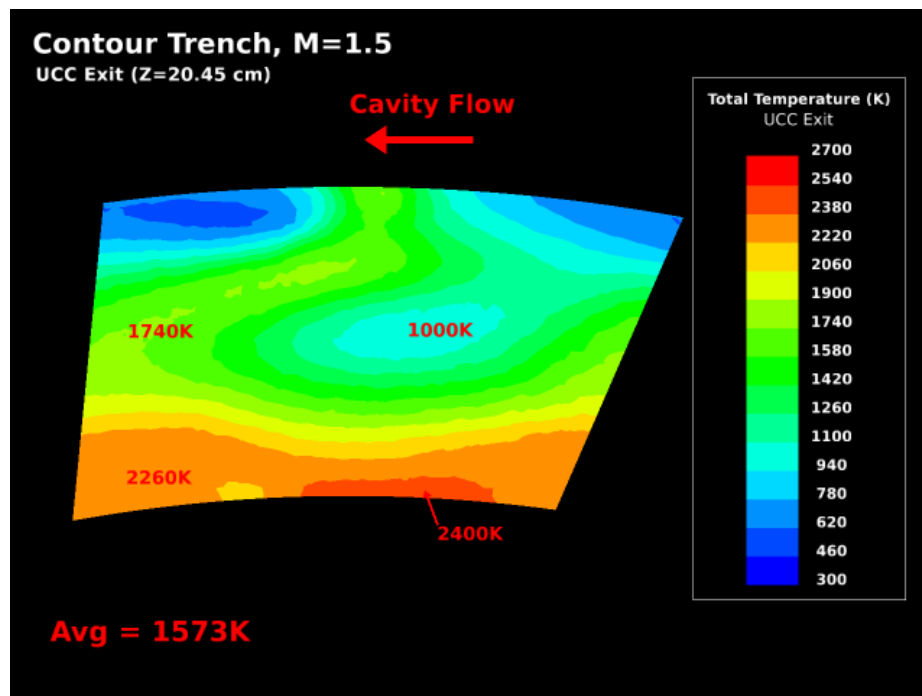


Figure 4.25: UCC Exit Temperature Contour M=1.5

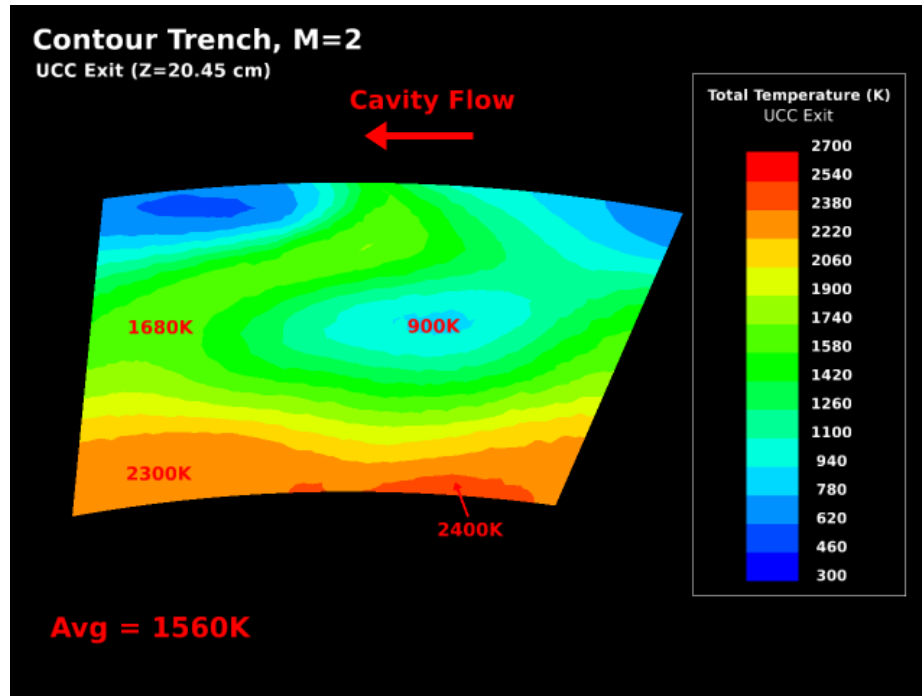


Figure 4.26: UCC Exit Temperature Contour M=2

Additional spanwise-averaged data were taken at 150D (right outside of the cavity) and 200D away from the leading edge circumferential cavity. Investigating the fuel and CO concentration uncovers more benefits of film-cooling the UCC other than a temperature reduction. Looking at the concentration of fuel through the UCC, the plots in Figures 4.27-4.29 reveal that unburned fuel near the upper endwall convects towards the lower endwall. Based on the flow characteristics previously discussed, the spanwise average data agrees with the fluid from the circumferential cavity convecting into the core flow starting at the upper endwall, and as the vortices form along the suction side surface it spans down the vane as shown in Figure 4.9. Figure 4.27 and 4.28 shows through film-cooling 75% of the fuel was consumed versus only 65% of unburned fuel consumed without film-cooling across a 50D distance. From the chemical reactions that are modeled for the current design, analyzing the CO_2 will give indication of complete combustion occurs. When CO combusts, more CO_2 is available. Figures 4.33-4.35 indicate that the reactions are completing as the

fluid exits the UCC, which will ensure that the turbine section does not encounter incomplete reactive species.

Although there is a higher concentration of fuel at the exit from Figure 4.29, the amount of fuel at 50% span shifted and shows it starting 30% span. In Figure 4.29, the plot helps reason why the lower endwall is heated, as shown in the temperature contour plots. It is because more fuel is being concentrated at the lower endwall region. Increasing the blowing ratio does reduce the amount of the fuel without drastically heating the wall from the additional amount of burning.

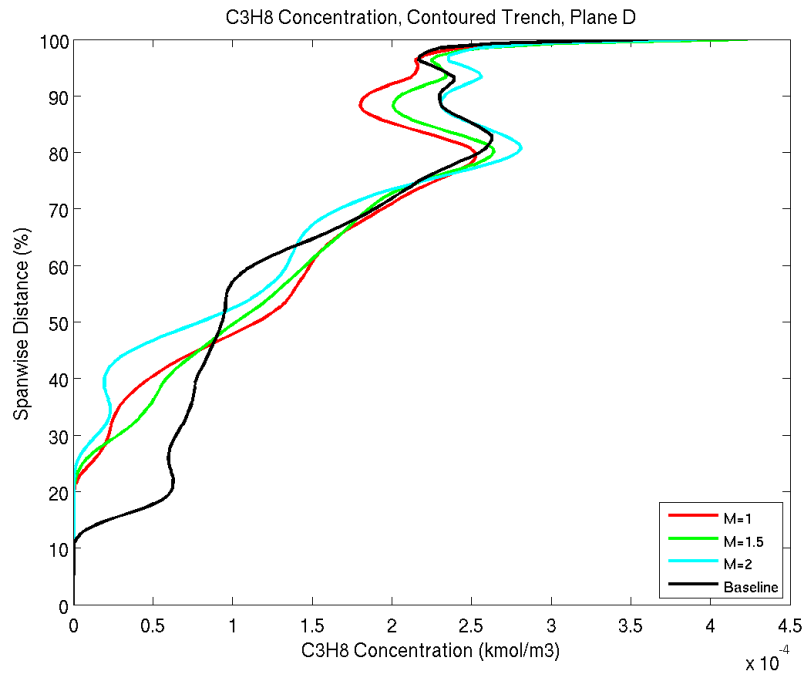


Figure 4.27: Spanwise average C_3H_8 concentration at location D (150D)

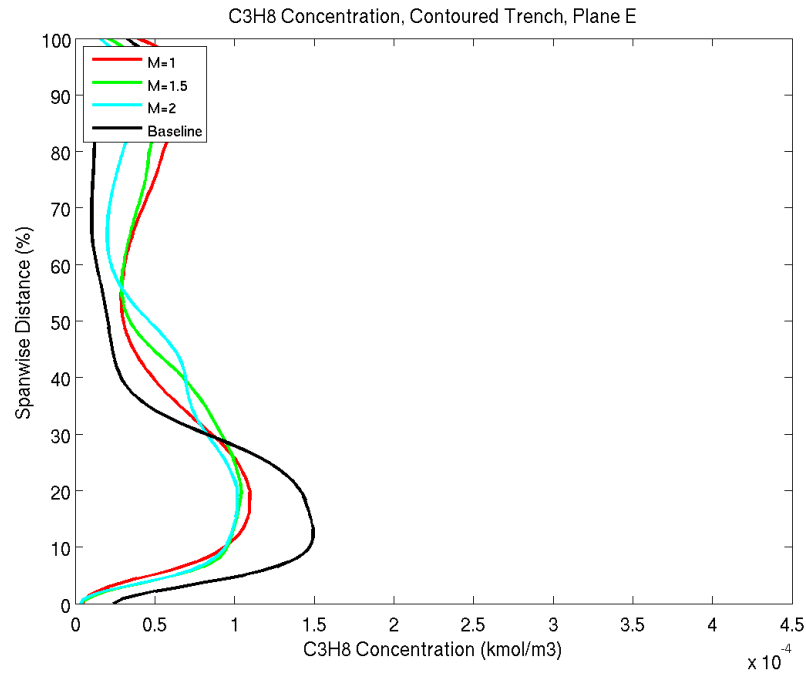


Figure 4.28: Spanwise average C₃H₈ concentration at location E (200D)

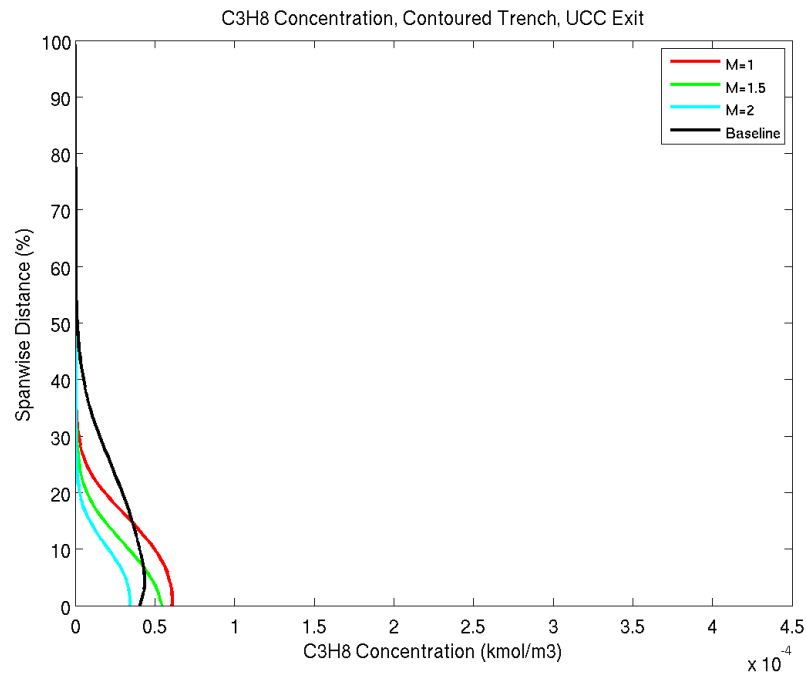


Figure 4.29: Spanwise average C₃H₈ concentration at UCC exit

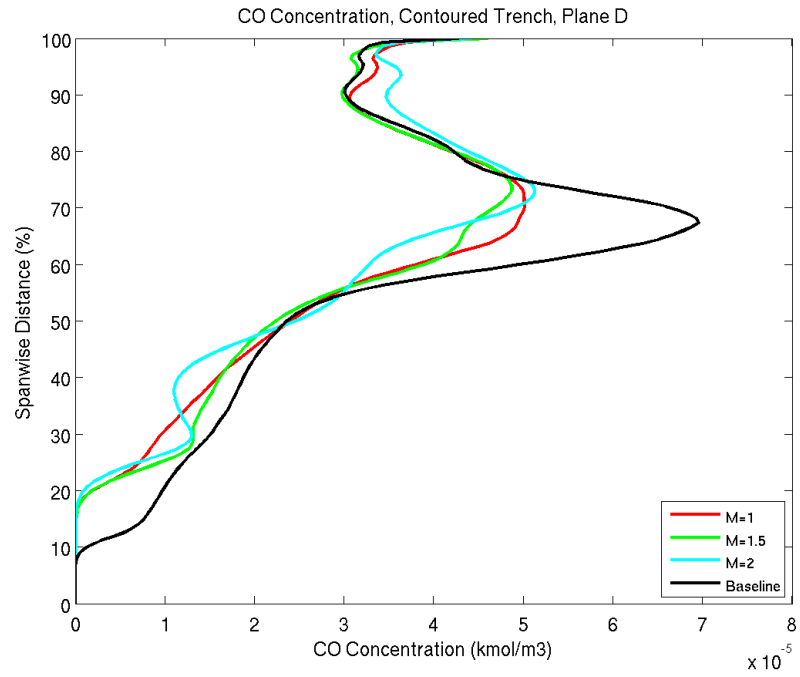


Figure 4.30: Spanwise average CO concentration at location D (150D)

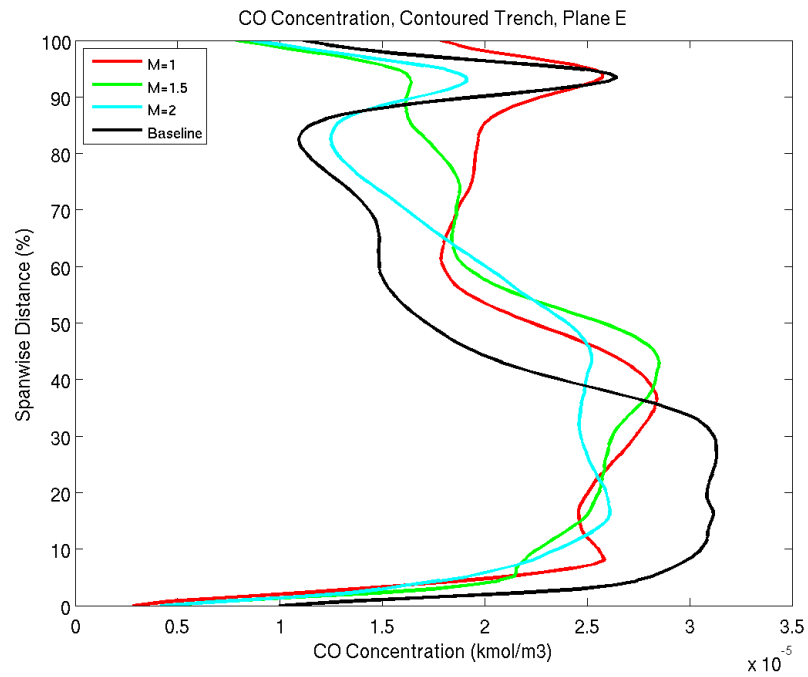


Figure 4.31: Spanwise average CO concentration at location E (200D)

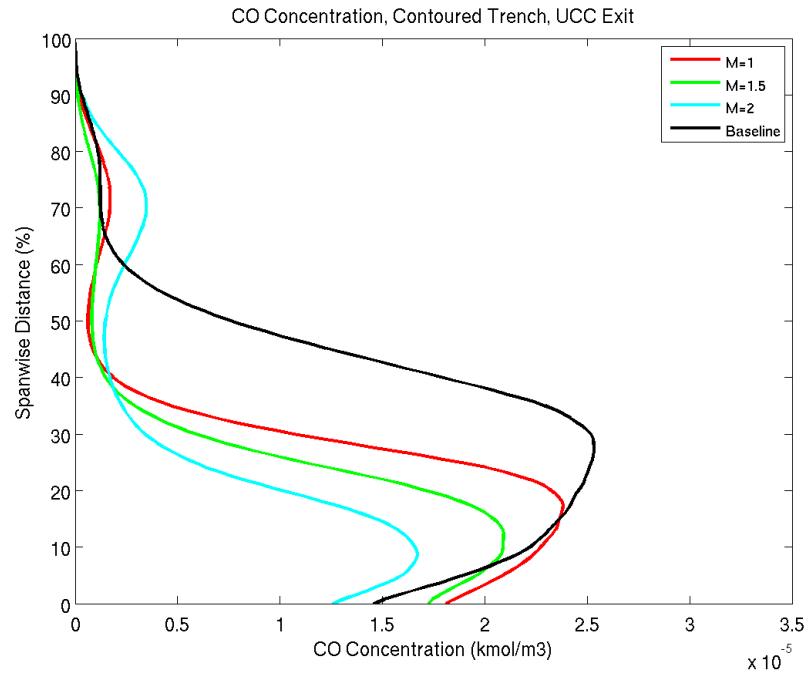


Figure 4.32: Spanwise average CO concentration at UCC exit

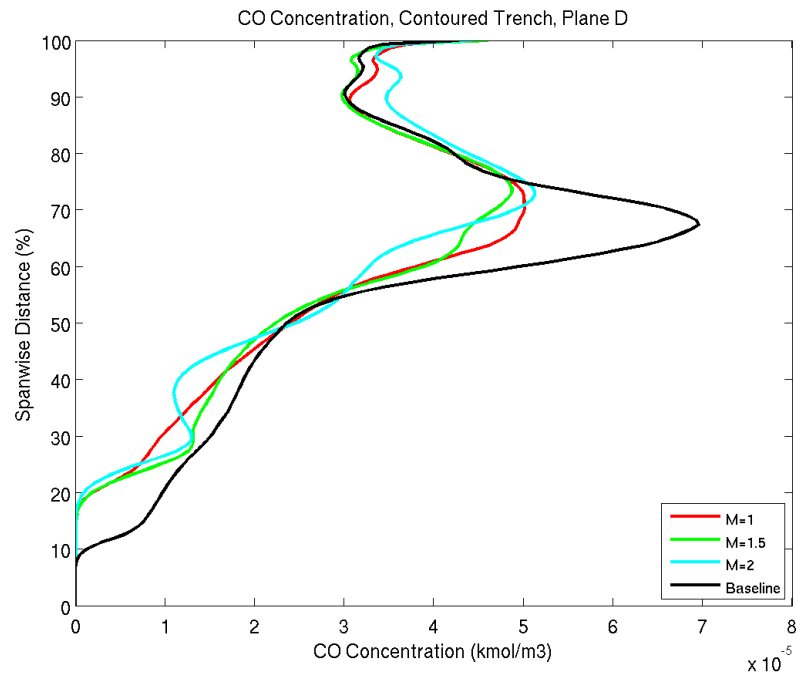


Figure 4.33: Spanwise average CO₂ concentration at location D (150D)

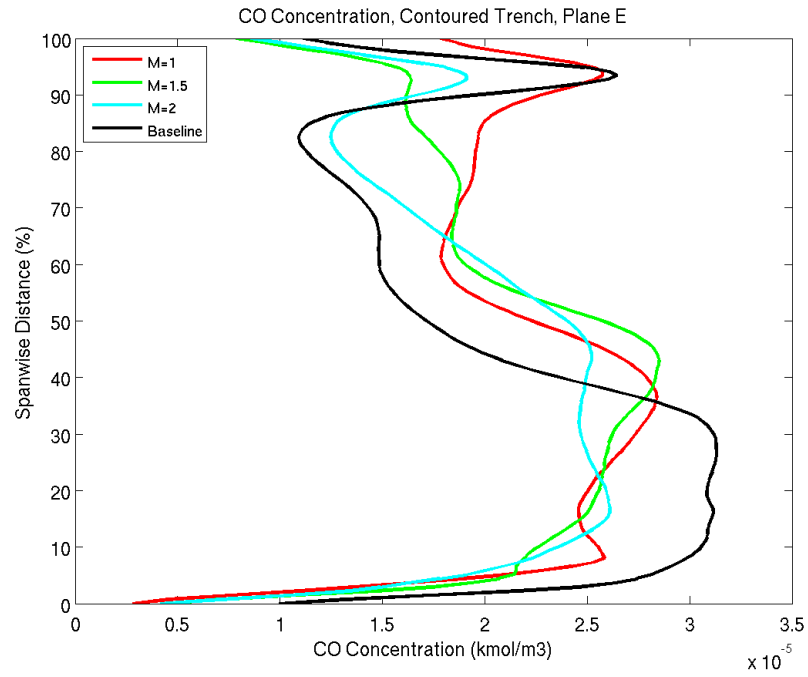


Figure 4.34: Spanwise average CO₂ concentration at location E (200D)

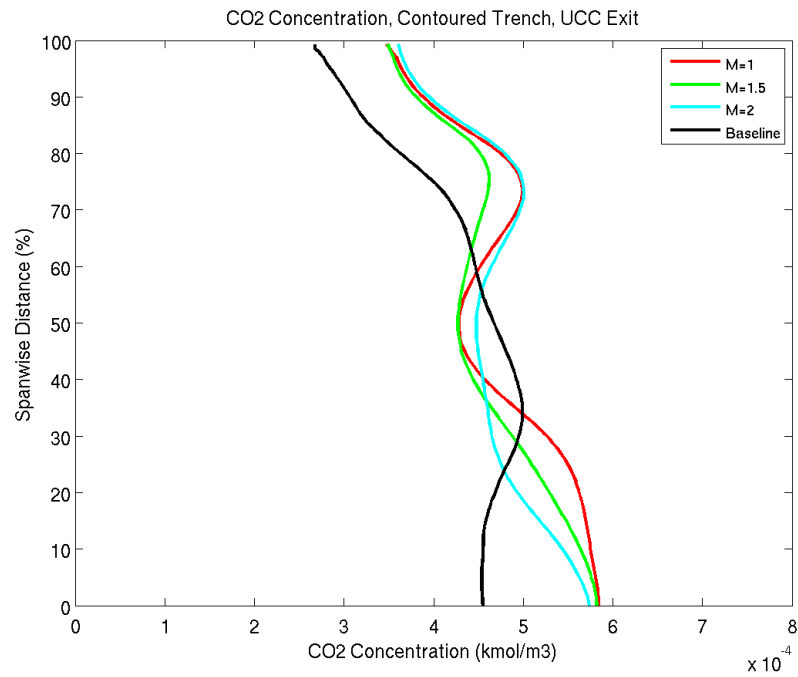
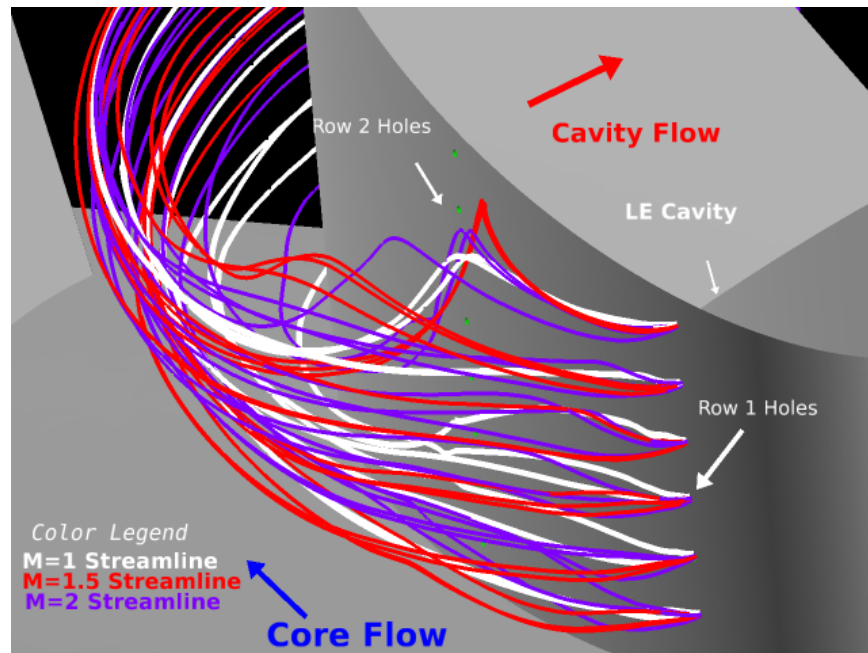


Figure 4.35: Spanwise average CO₂ concentration at UCC exit

4.3 Normal Hole Results

After the contoured trench study, the normal hole configuration was investigated and the results from the numerical analysis are discussed below. Similar to the contoured trench design, a single row of holes were placed on the suction side surface of the vane at two locations. The first row of holes was placed below the leading edge of the cavity, and another row of holes was placed below the mid-section of the circumferential cavity. With the same purpose as the contoured trench, the reason for these locations are to cool the surface by providing a film-cooling layer before the gaseous fluid exits the cavity keeping the vane surface cool.

4.3.1 Internal Flow Interactions. In each of the cases, the coolant contained enough momentum as it ejected out of the coolant holes separating away from the wall and into the core flow immediately. In Figures 4.36 and 4.39, the streamlines for each blowing ratio are shown in white, red, and purple for $M=1$, $M=1.5$ and $M=2$, respectively. As film-coolant is introduced from the first row (near the leading edge of the cavity), the coolant fluid was pushed away from the vane wall and spanned down the vane as it flows downstream. As it convected down the vane, the coolant for the two holes near the top of the vane exited into the core flow then curled back into the vane before reaching the second row of holes. The coolant was ejected far enough away from the vane surface that the lighter exhaust from the cavity section begins to roll down the vane. The coolant fluid that was flowing in the downstream direction interacted with the cavity fluid that has a normal velocity component. With the cavity fluid having more momentum, it drew the coolant up into the cavity then pushed it back down into the core flow. In Figure 4.38, an illustration of this fluidic behavior is shown by the use of velocity vectors and coolant streamlines.



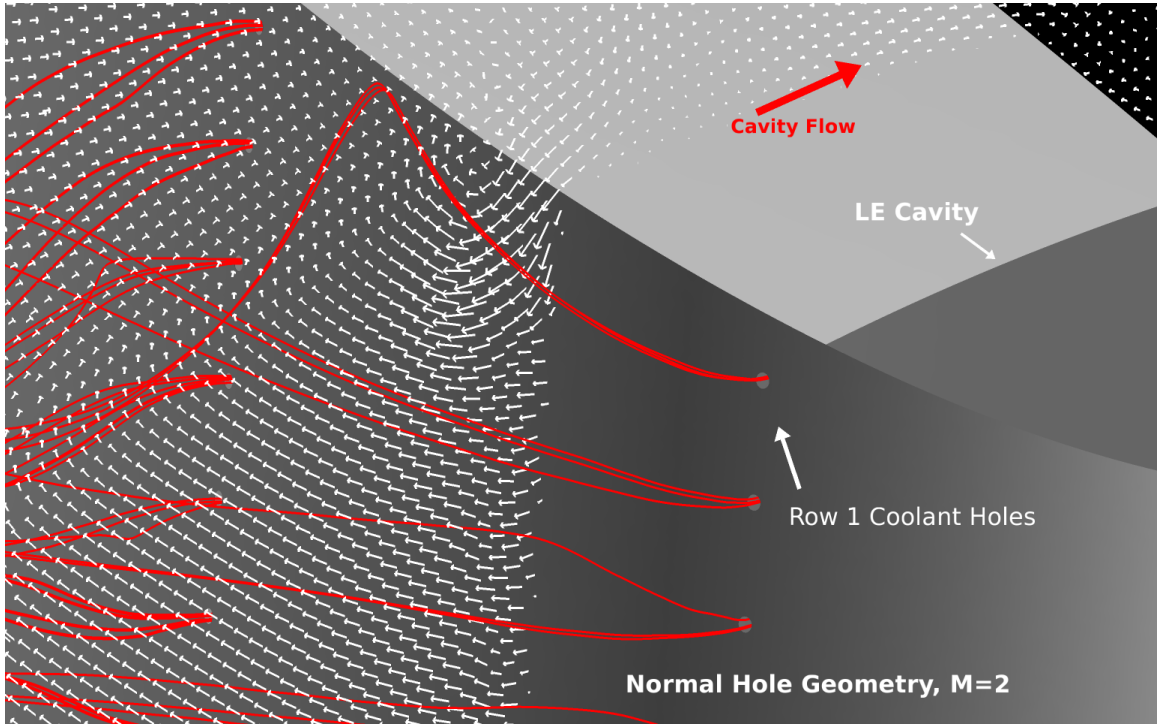
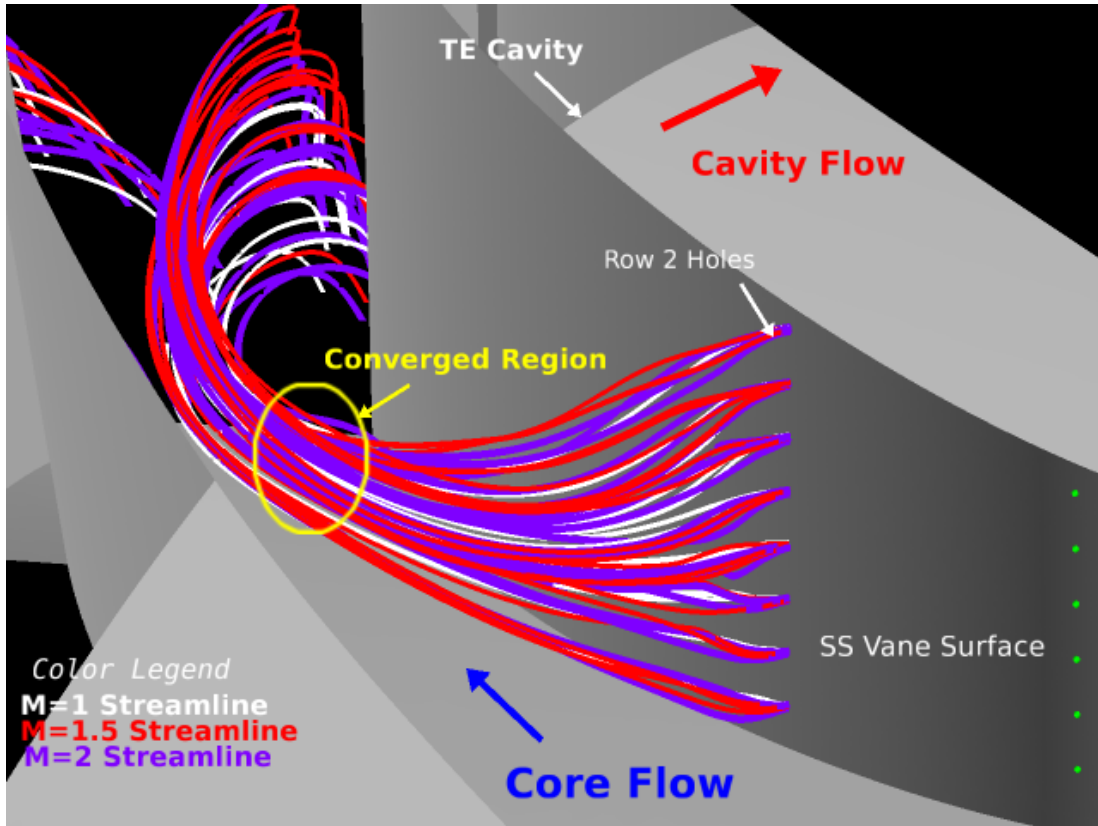
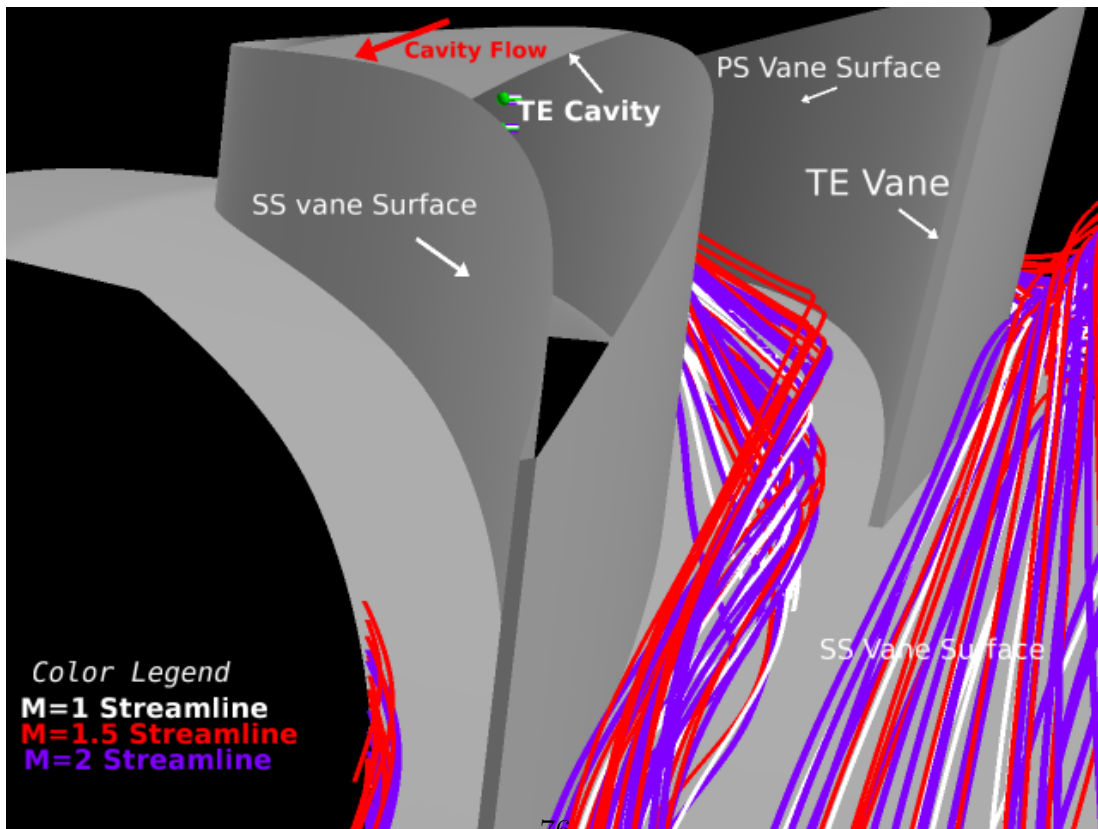


Figure 4.38: Normal hole coolant interaction plotted against velocity vectors

At the second row of holes of the normal hole configuration, the coolant does not have the curling behavior immediately after the holes as the contoured trench design. Instead the coolant converged together as it convected downstream as shown in Figure 4.39a. In Figure 4.39b, a view from looking upstream shows the coolant curling into the trailing edge section of the vane eventually. Figure 4.40 is a streamline illustration of the cavity fluid (red) and coolant fluid (blue) from a top down view. Here the figure illustrates that between the coolant layer and the vane wall is exhaust fluid from the cavity section.



(a)



(b)

Figure 4.39: Coolant migration of row 2 for M=1, M=1.5 and M=2 a) isometric

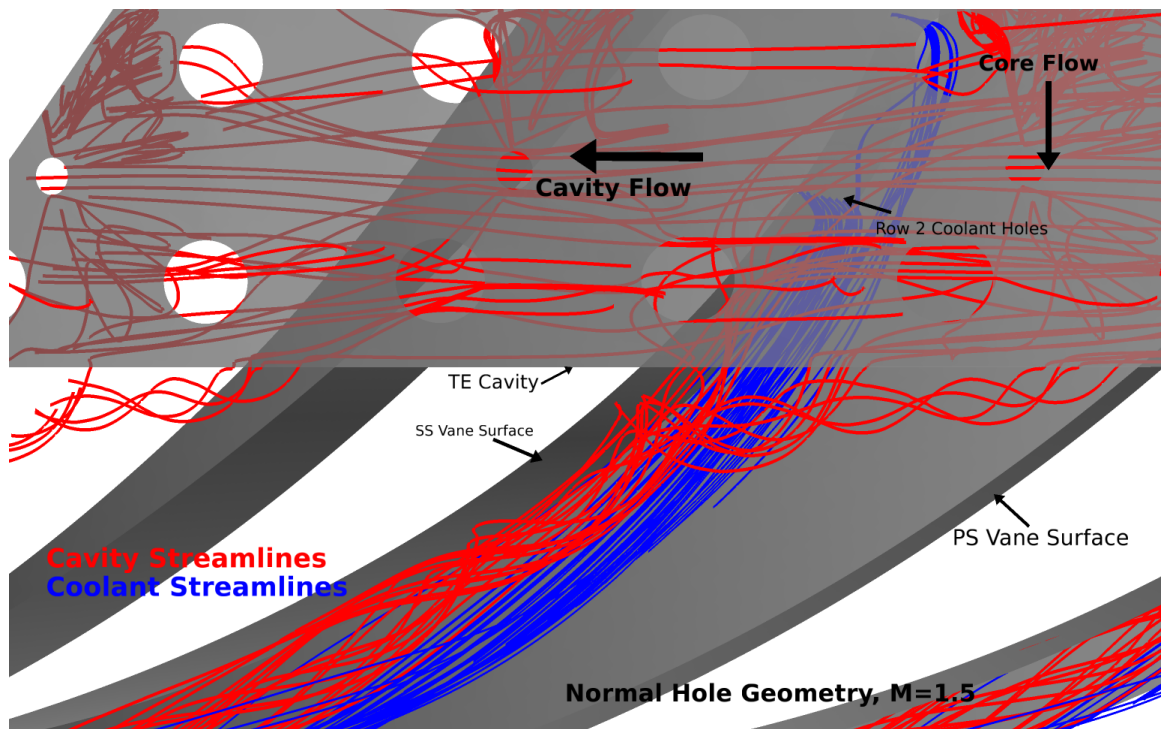


Figure 4.40: Cavity and coolant flow interaction for normal hole geometry, $M=1.5$ case

4.3.2 Temperature Distribution. Along the suction side surface of the vane, the temperature distribution does not vary towards the aft portion. Near the trailing edge section, the vane surface is predicted to be 2300K, independent of the the blowing ratio. In Figures 4.41 to 4.43, the temperature contours for each blowing ratio is shown and as the blowing ratio increases there is greater heating near the second row of coolant holes. For the $M=2$ case, a maximum value of the 2460K is predicted as shown in Figure 4.43 which indicates that secondary reactions are occurring right after the coolant holes. Looking at the temperature distribution radially, Figures 4.44 to 4.46 show temperature contour planes at 5 locations along the hybrid vane starting from the second row of coolant to the trailing edge section of the vane. Inspecting the countours closely for plane A, a distinct curling pattern is formed as the blowing ratio increases. At the next set of planes (B and C), temperature distributions were all the same for each blowing ratio.

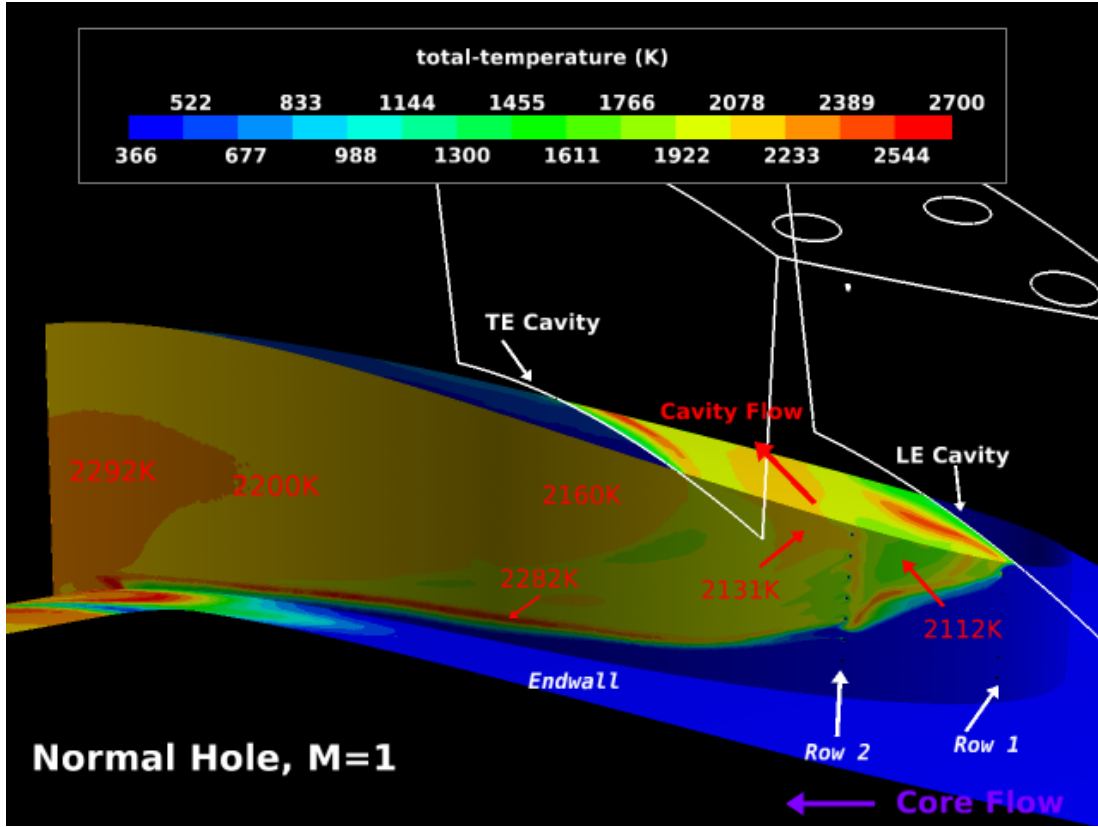


Figure 4.41: Airfoil temperature distribution for normal hole design ($M=1$)

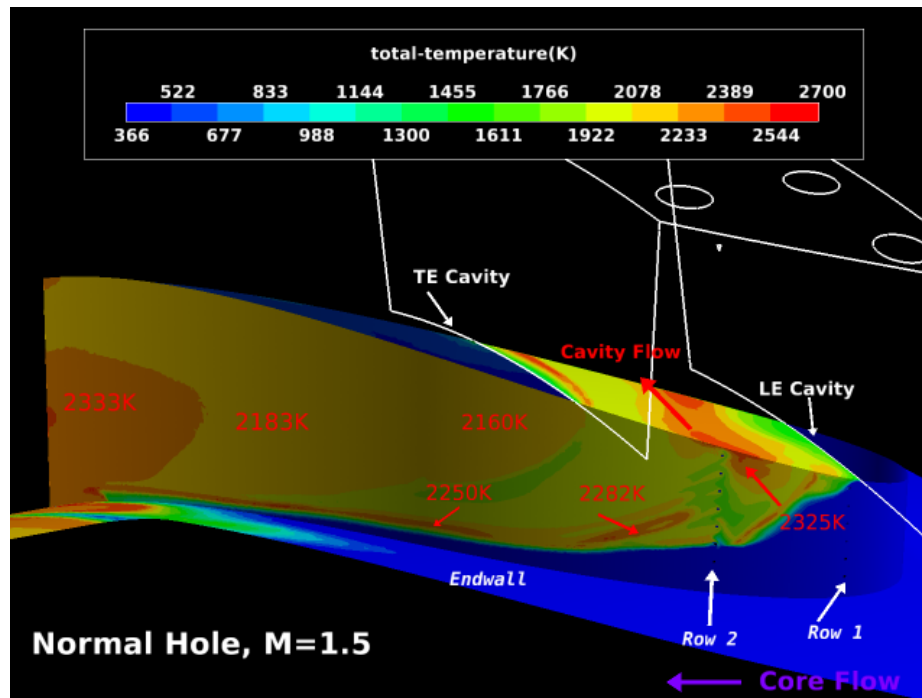


Figure 4.42: Airfoil temperature distribution for normal hole design (M=1.5)

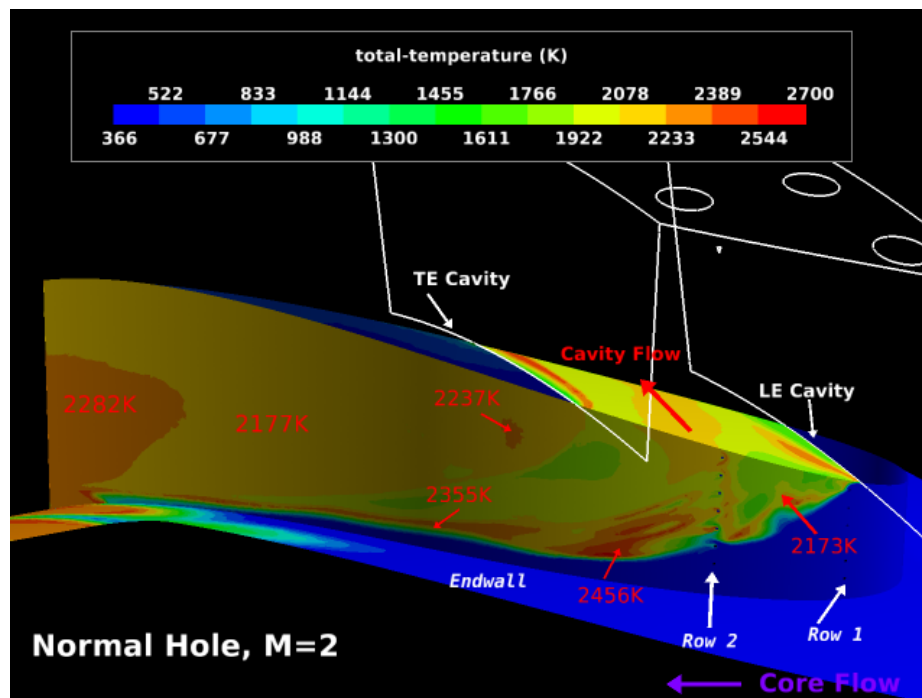


Figure 4.43: Airfoil temperature distribution for normal hole design (M=2)

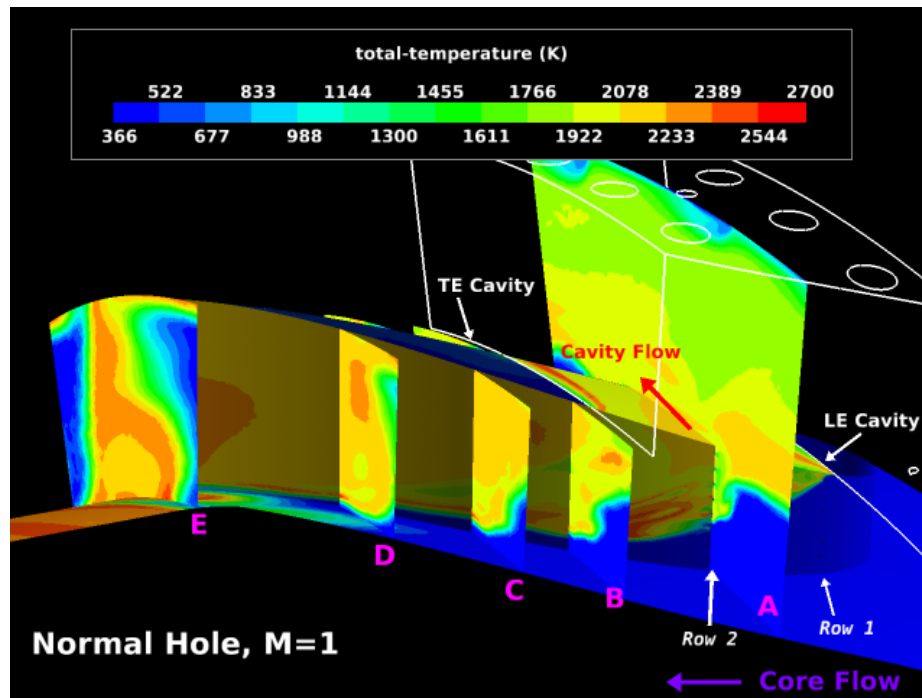


Figure 4.44: Radial temperature distribution for normal hole design ($M=1$)

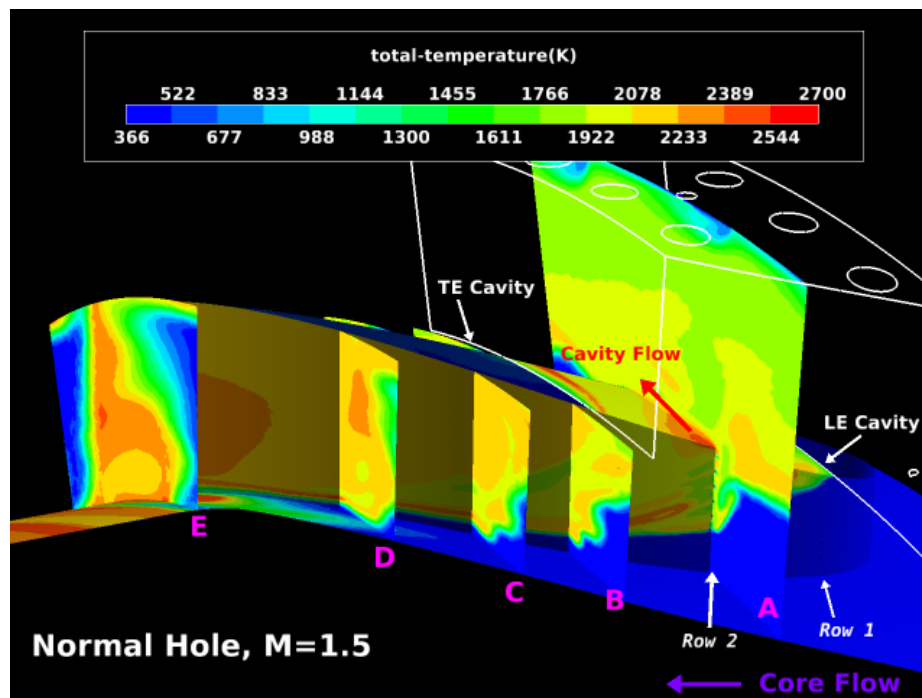


Figure 4.45: Radial temperature distribution for normal hole design ($M=1.5$)

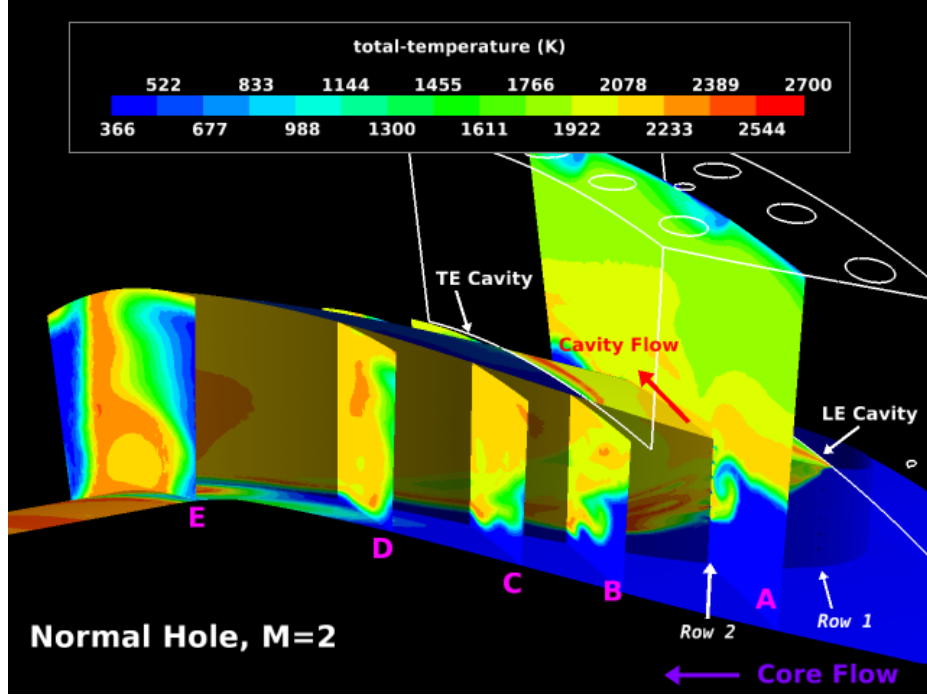
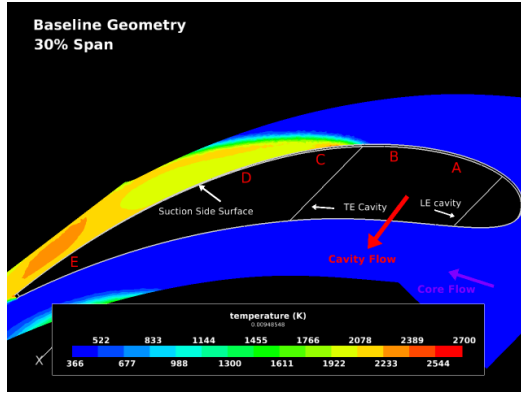
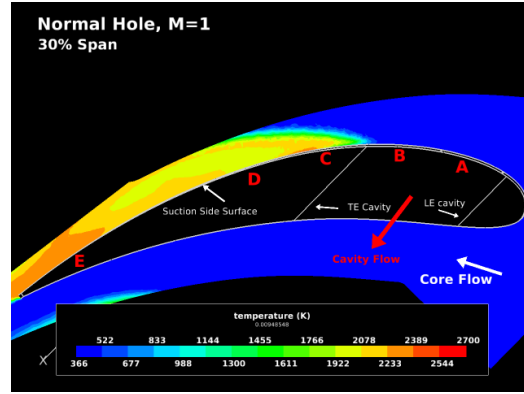


Figure 4.46: Radial temperature distribution for normal hole design ($M=2$)

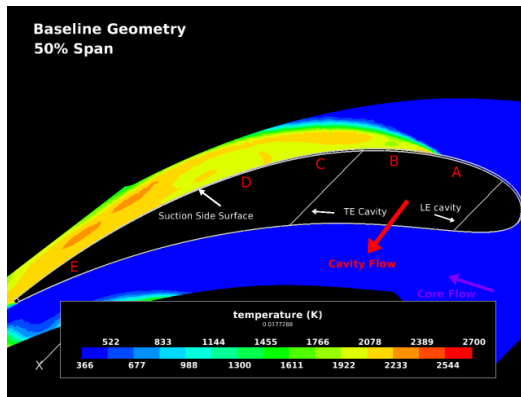
For the temperature distribution around the airfoil, at 30% span, the temperature contours reveal a spread in the start of the reactions along the suction side surface. In Figure 4.47b, the start of the reaction begins at location C for $M=1$, and when increasing the coolant flow to $M=2$, the secondary reactions spreads radially resulting in the vane being more heated. Figure 4.47b shows the reaction beginning at location B. The reason for this spread in reaction could be due to the fact that the normal hole configuration has more mixing from the presence of counter-rotating vortices. Comparing all the cases to the baseline model, significant heat loads were noticed near the trailing edge portion of the vane at 50% span. Figures 4.47d, 4.48c and 4.48d, all show the heat load across 25% of the chord near the vane surface. From this aspect, film-cooling negatively impacts the thermal profile of the UCC vane.



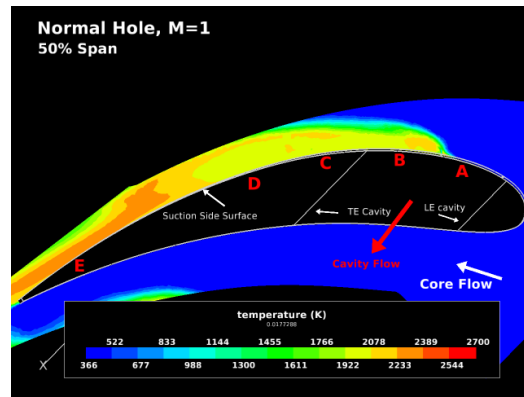
(a) Baseline 30% Span



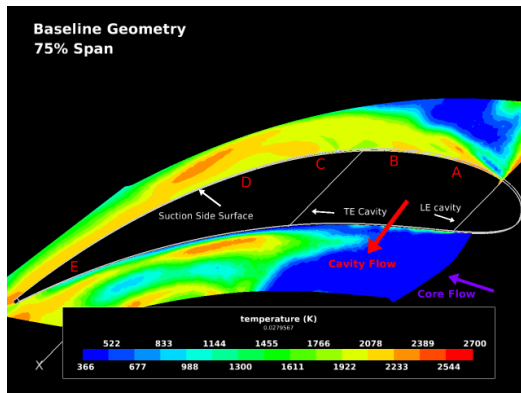
(b) Normal Hole ($M=1$), 30% Span



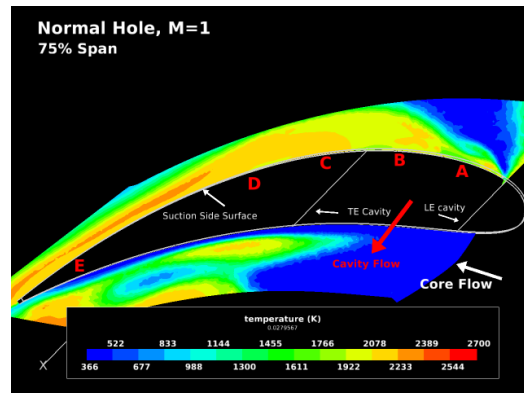
(c) Baseline 50% Span



(d) Normal Hole ($M=1$), 50% Span

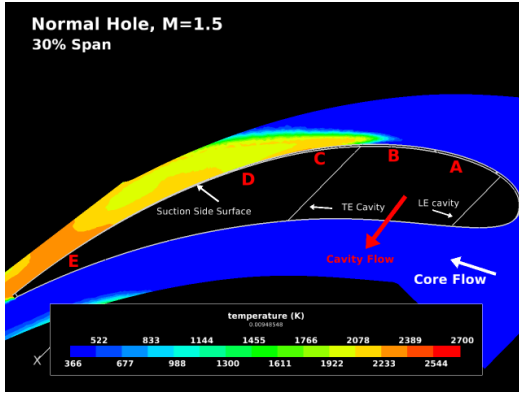


(e) Baseline 75% Span

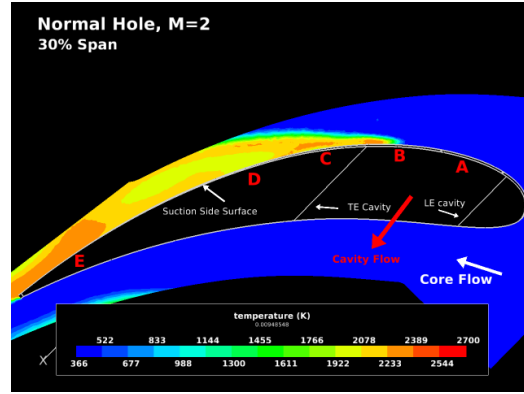


(f) Normal Hole ($M=1$), 75% Span

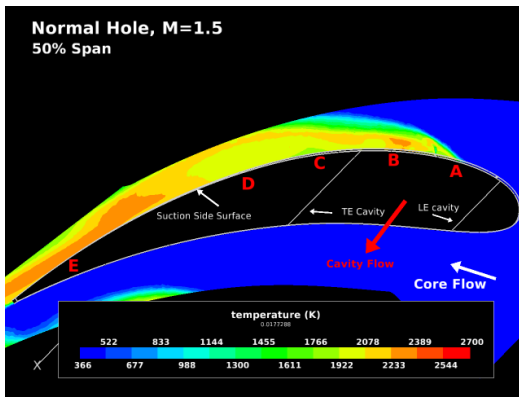
Figure 4.47: Spanwise temperature of baseline (left column) and normal hole design $M=1$ case (right column)



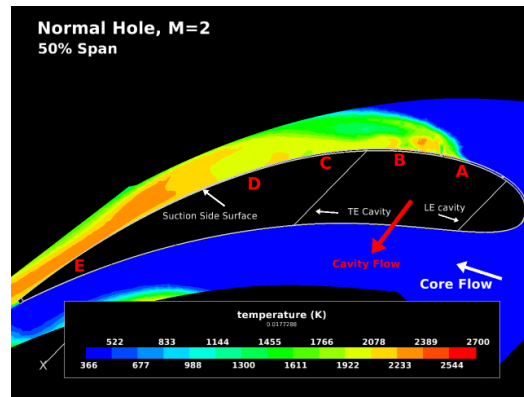
(a) Normal Hole ($M=1.5$), 30% Span



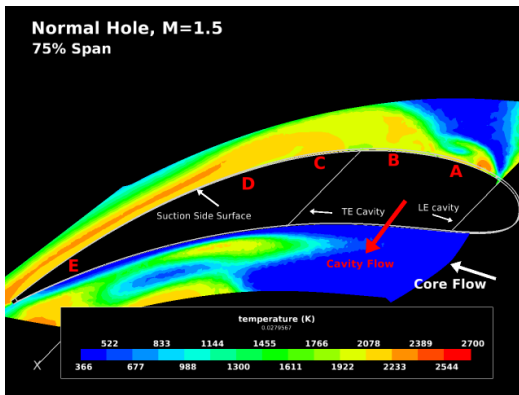
(b) Normal Hole ($M=2$), 30% Span



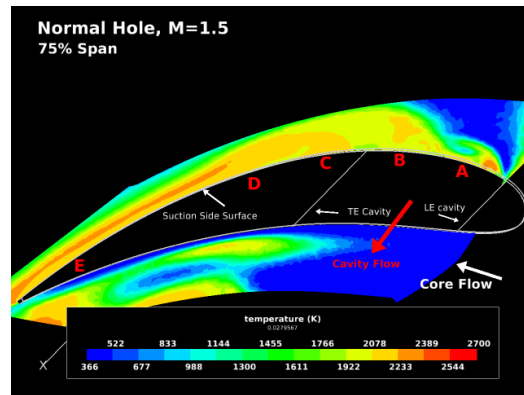
(c) Normal Hole ($M=1.5$), 50% Span



(d) Normal Hole ($M=2$), 50% Span



(e) Normal Hole ($M=1.5$) 75% Span



(f) Normal Hole ($M=2$), 75% Span

Figure 4.48: Spanwise temperature of normal hole for $M=1.5$ case (left column) and $M=2$ (right column)

4.3.3 Exit Conditions. As the flow exits the UCC, excessive heating occurs on the lower endwall surfaces as shown in Figure 4.50 to 4.52. A peak temperature of 2440K is predicted and located on the lower endwall. A summary of the exit conditions can be seen in Table 4.2 for each of the cases. Similar to the contoured trench design, the normal hole design configuration has a uniform temperature distribution in the radial direction yet up the span of the vane is an undesirable temperature profile. A slight improvement to the profile factor was noticed because of more radial spreading of the hotter region near the lower endwall which raised the average temperature at the exit.

Table 4.2: Normal hole geometry exit conditions

Case	Mach	Profile Factor	Pattern Factor	$\frac{dp}{P}\%$
Baseline	0.280	0.40	0.71	10.5
M=1	0.311	0.51	0.56	9.2
M=1.5	0.315	0.50	0.58	9.5
M=2	0.319	0.54	0.57	9.6

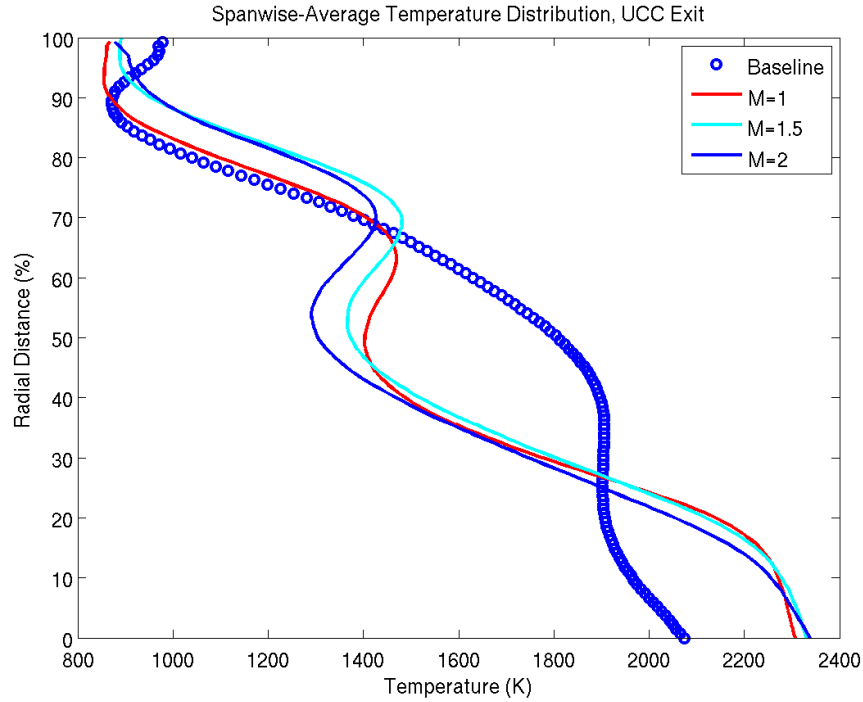


Figure 4.49: Spanwise averaged temperature distribution at UCC exit

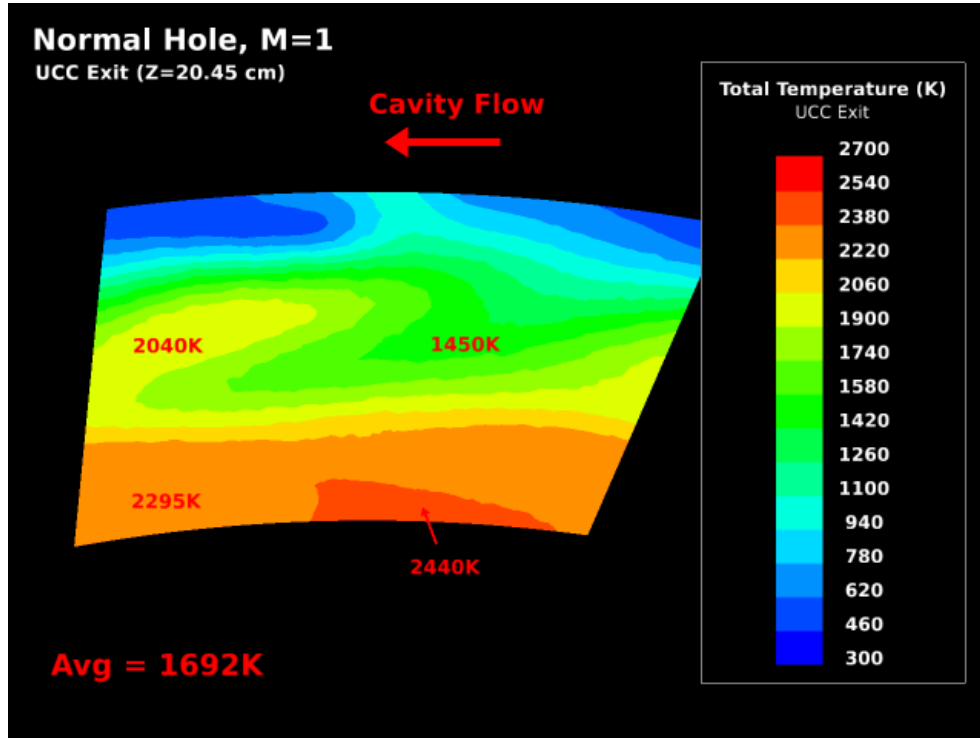


Figure 4.50: UCC exit temperature contour M=1

Looking at the spanwise-average concentration of C_3H_8 , CO , and CO_2 through the UCC, Figures 4.53–4.55 reveal that the concentration of fuel has decreased near the lower endwalls of the UCC when applying film cooling. This makes sense as more burning occurs near the lower portion of the vane as shown in the temperature contours and the higher heating at the exit of the UCC. The spanwise locations of the species agree with the flow characteristics previously discussed. In Figure 4.53, the high concentrations of fuel is present, and as the flow progresses from Location D to the UCC exit, fuel is concentrated near the lower endwall. In essence this corresponds to the vortex that sheds out of the cavity section and spans down the vane wall. Figures 4.56–4.58 indicate that in exchange of fuel being burned more CO is available. As the blowing ratio increases, the amount of CO is reduced. The reason for this is because further completion of reactions occur and more CO_2 is produced. It is interesting to point out that from the CO_2 plots in Figure 4.59 to Figure 4.61 the

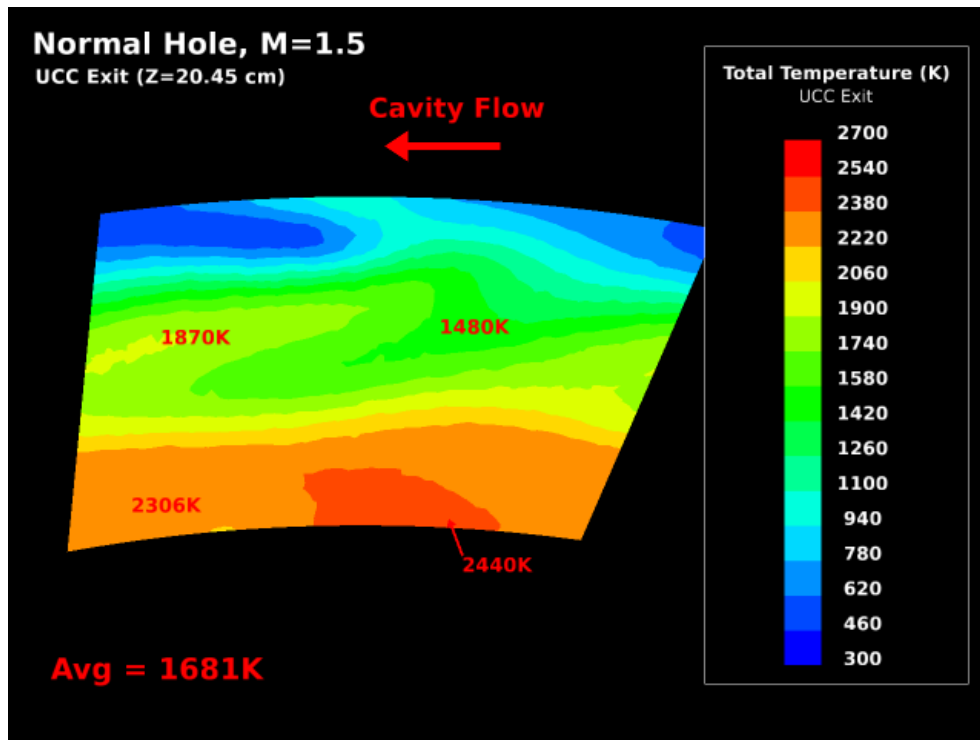


Figure 4.51: UCC exit temperature contour M=1.5

possibility of unburnt species reacting within the turbine has been reduced as CO_2 is a good indicator of completion of reactions.

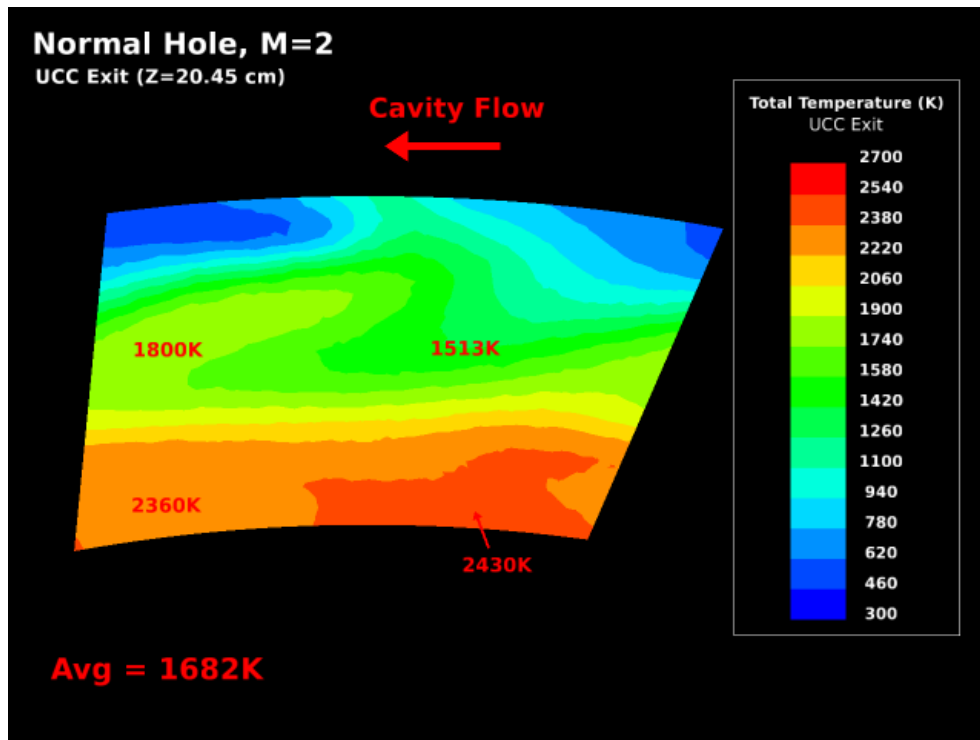


Figure 4.52: UCC exit temperature contour M=2

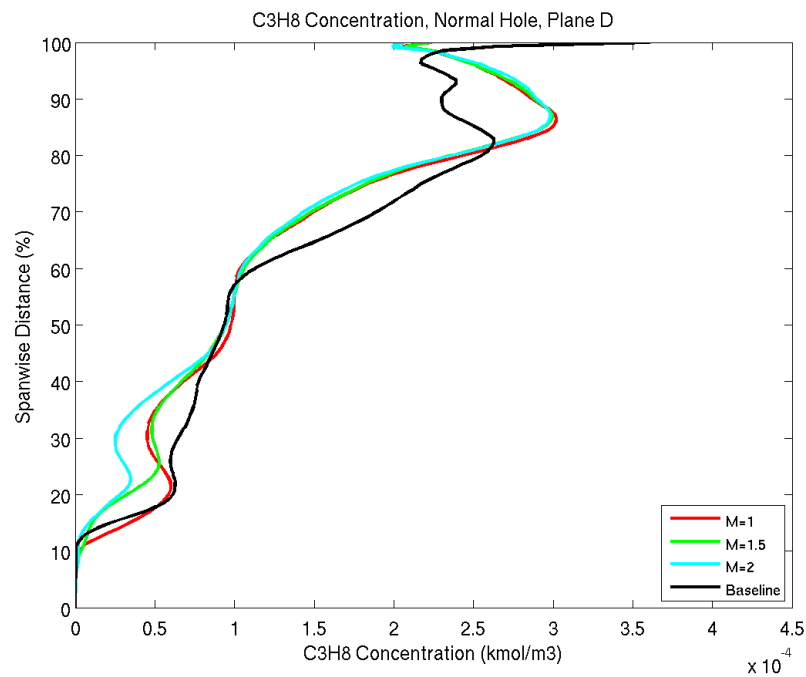


Figure 4.53: Spanwise-average C_3H_8 concentration at location D (150D)

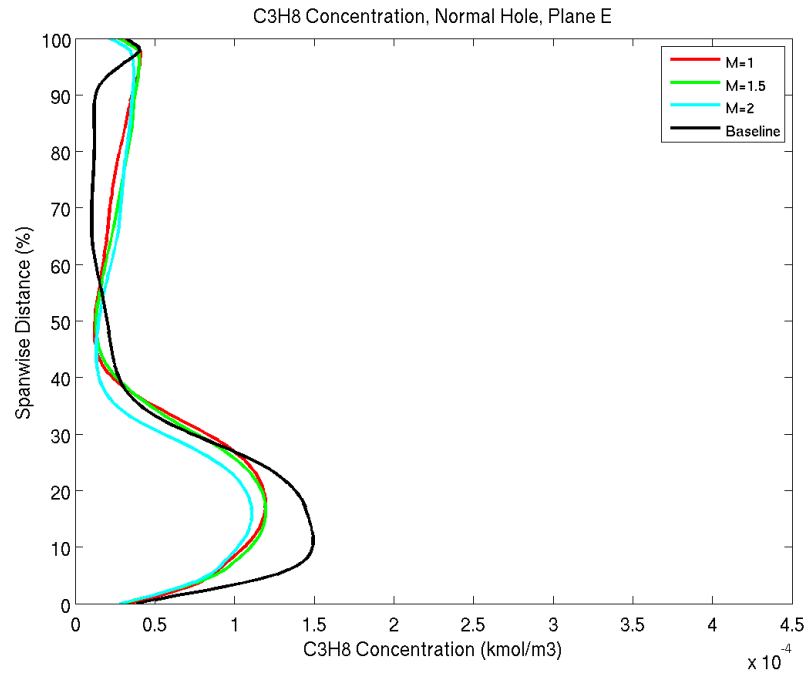


Figure 4.54: Spanwise-average C_3H_8 concentration at location E (200D)

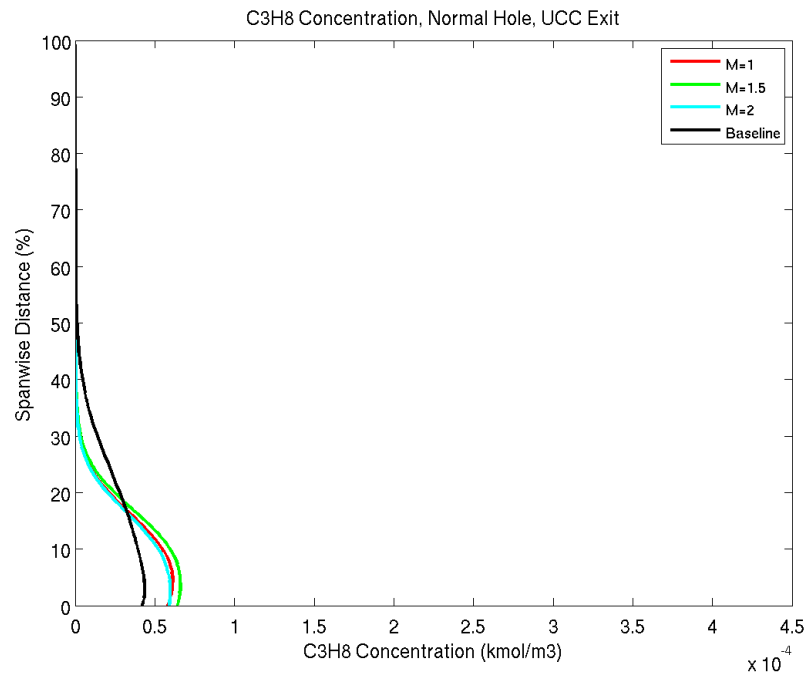


Figure 4.55: Spanwise-average C_3H_8 concentration at UCC exit

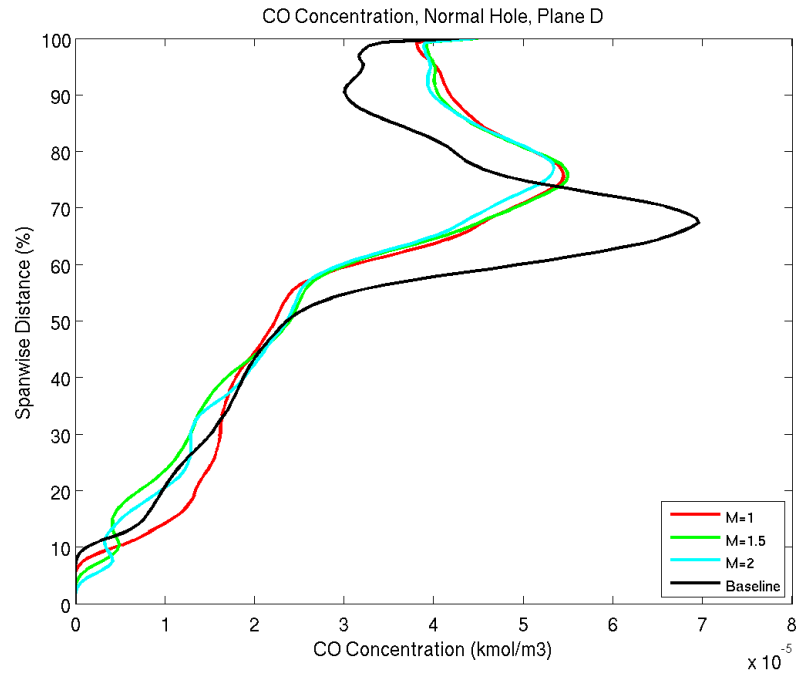


Figure 4.56: Spanwise-average CO concentration at location D (150D)

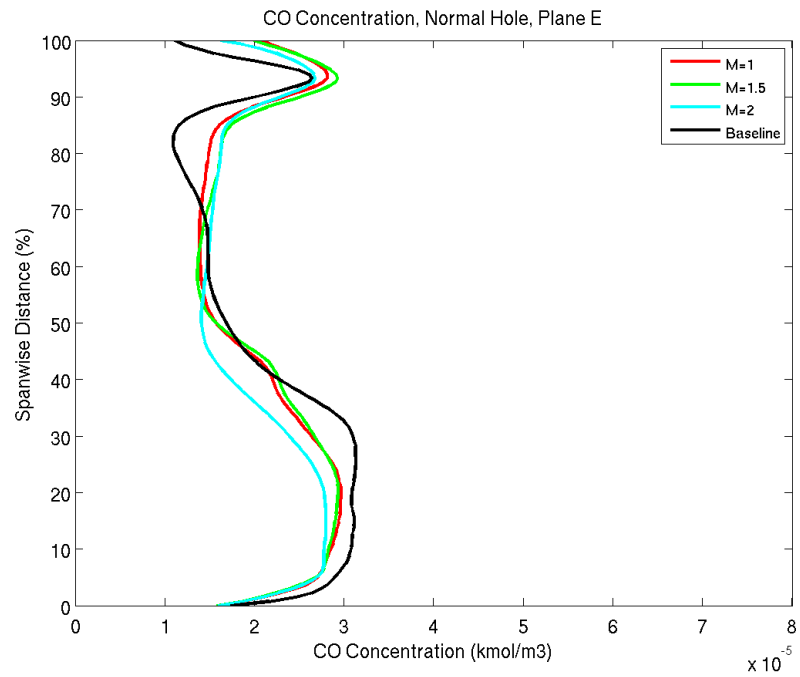


Figure 4.57: Spanwise-average CO concentration at location E (200D)

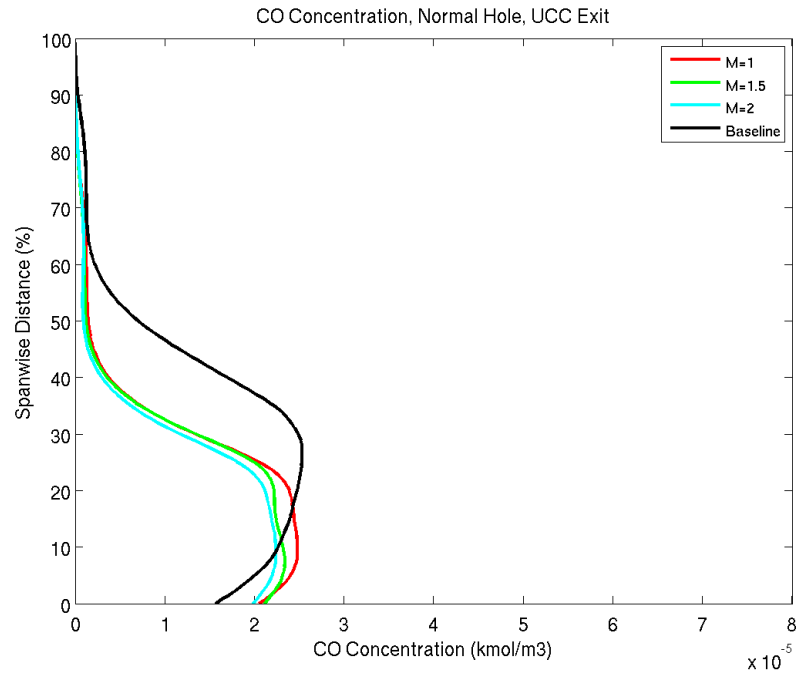


Figure 4.58: Spanwise-average CO concentration at UCC exit

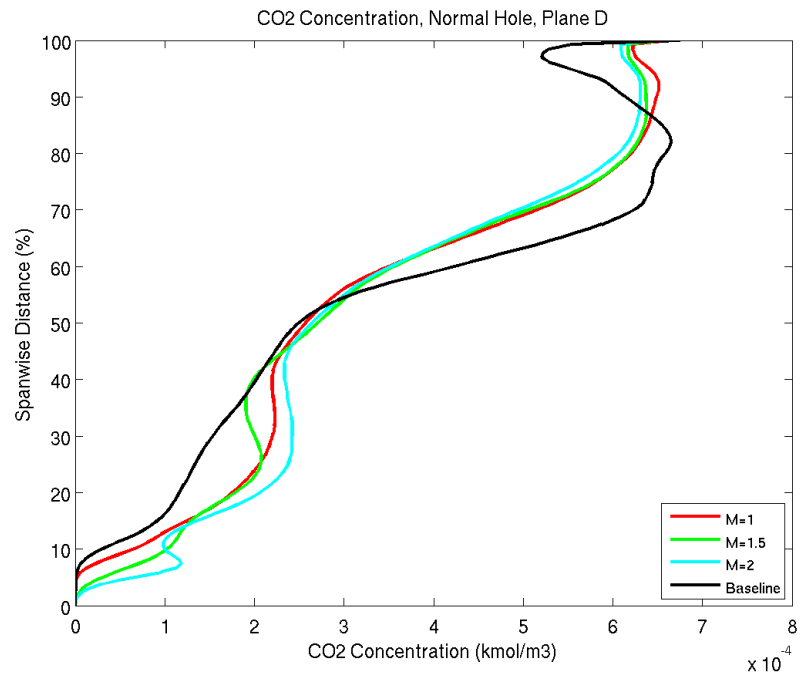


Figure 4.59: Spanwise-average CO₂ concentration at location D (150D)

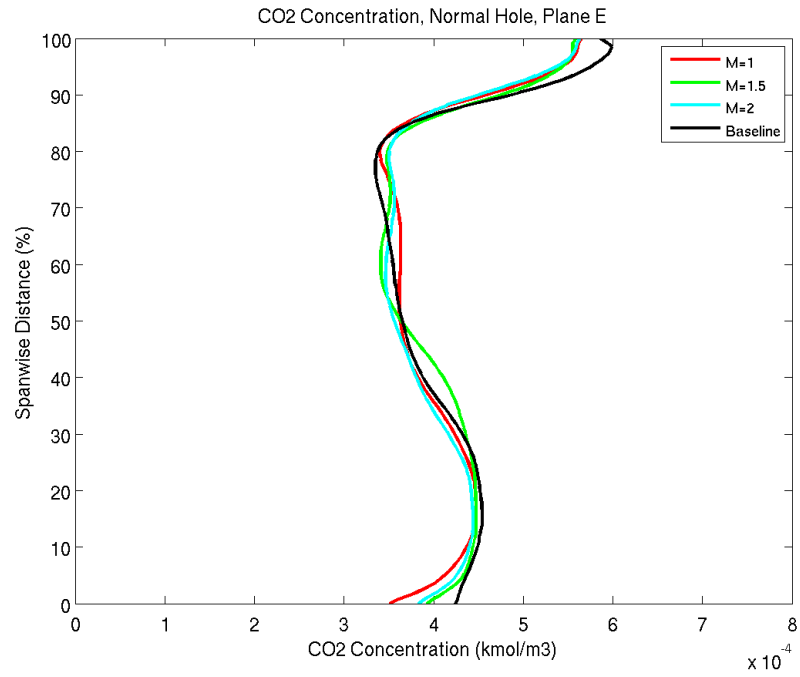


Figure 4.60: Spanwise-average CO₂ concentration at location E (200D)

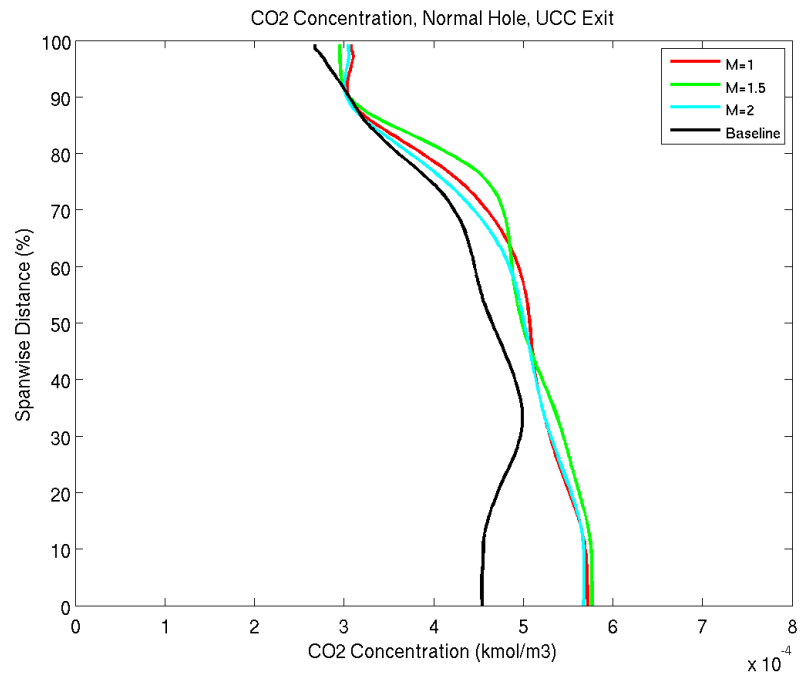


Figure 4.61: Spanwise-average CO₂ concentration at UCC exit

4.4 Hybrid Geometry Results

From the results of the normal hole geometry and contoured trench design, a final film-cooling geometry that combines the two geometries was analyzed for this effort. In Figure 4.62, the outline of the hybrid coolant geometry is overlayed against a temperature contour of the baseline model. From this view, one can see that the first trench follows along the reaction line of the baseline model. The two distinct temperature regions formed along the suction side surface of the baseline model has cooler region at 366 K and hotter region above 2200 K. For the hybrid geometry, a blowing ratio of $M=2$ was studied and the results for this test case are presented below.

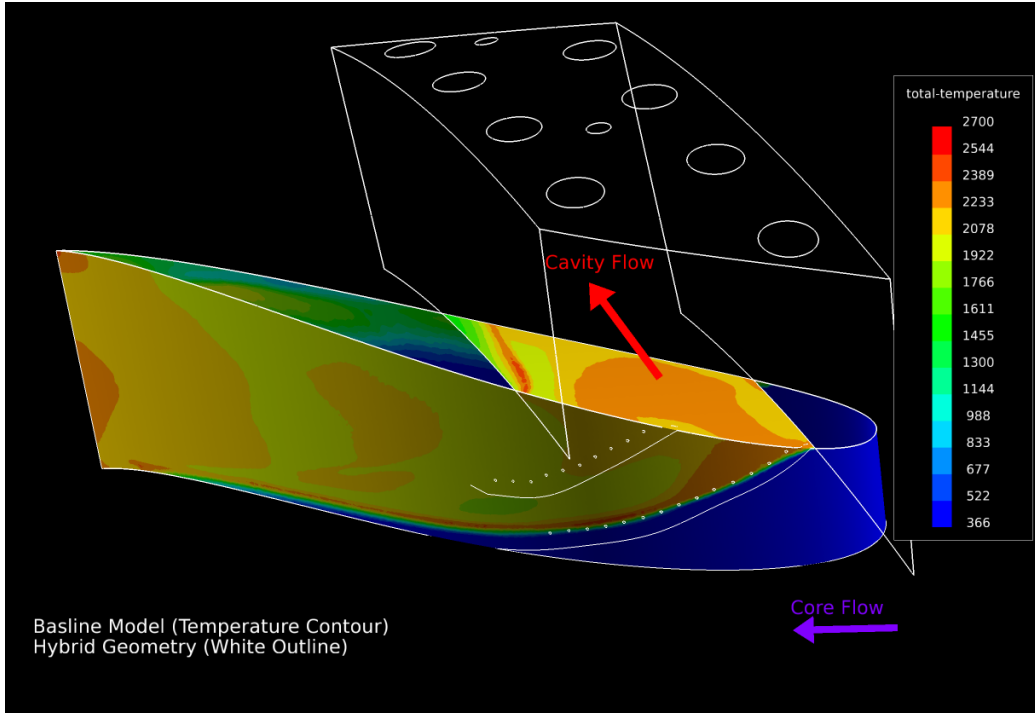


Figure 4.62: Hybrid geometry layout set against baseline temperature predictions

4.4.1 Internal Flow Interactions. As discussed before, vortices were formed by the exhaust fluid that exited out of the circumferential cavity and into the axial core flow. For the two geometries previously studied, it was shown that the vortex of the exhaust fluid begins at the lip of the trailing edge cavity at the top of the

suction side surface of the vane, and streamlines showed that the vortex rolls along the span of the vane as it exits the UCC. It was also shown that the vortex had greater momentum and pushed the coolant away from the vane surface, decreasing the effectiveness of film-cooling. The fluidic behavior within the UCC for the hybrid geometry is also similar to the two geometries previously analyzed.

For the first row, the trench with discrete holes behaved similar to the contoured trench design. From Figure 4.5, the coolant near the top of the vane ejected and rolled out radially away from the vane. In Figure 4.63, the same pattern was noticed. For this figure, the first two coolant holes were seeded pink in order to draw out this rolling feature.

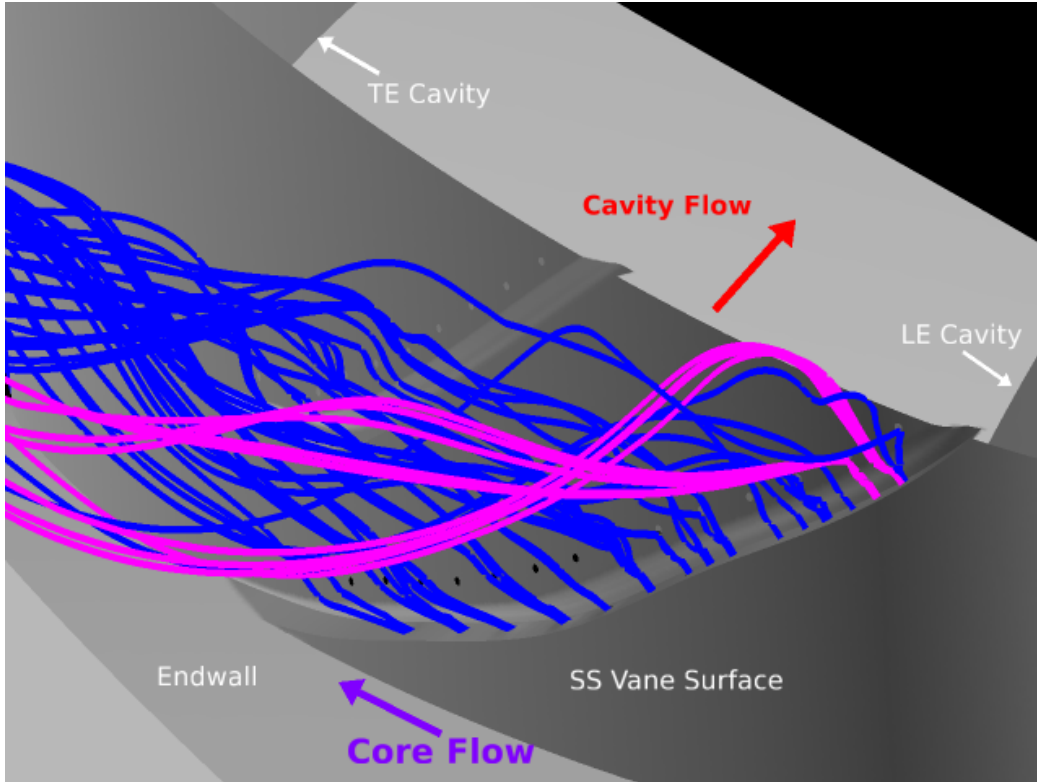


Figure 4.63: Hybrid geometry trench 1 coolant flow separation (pink) from vane surface, $M=2$

Looking at the second row, Figure 4.64 shows the coolant (blue) flow separated again from the cavity (red) fluid as expected. Interestingly, tapering the coolant trench along the vane helped in keeping the lower endwall and vane surface cool. In

Figure 4.65, the streamlines of the exhaust exiting the cavity is shown. It is interesting to point out that the vortex travels in the streamwise direction rather than down the span of the vane as the previous two coolant geometries did. Experimental work done by Parks [21] showed a similar behavior of the cavity fluid not making it to the inner endwalls in his ‘tiger-claw’ configuration. Figure 4.66 shows the same streamlines as in Figure 4.64 but scaled with temperature, illustrating the reactions along the vane surface.

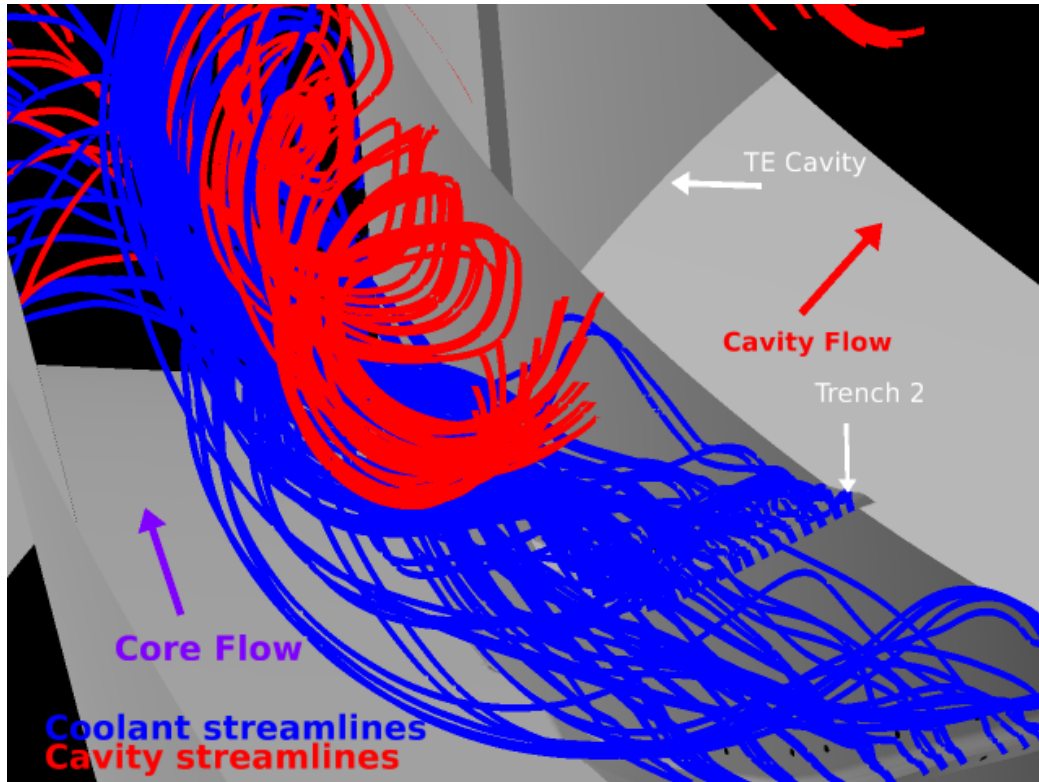


Figure 4.64: Coolant and cavity flow interaction for Hybrid coolant geometry, M=2 Case

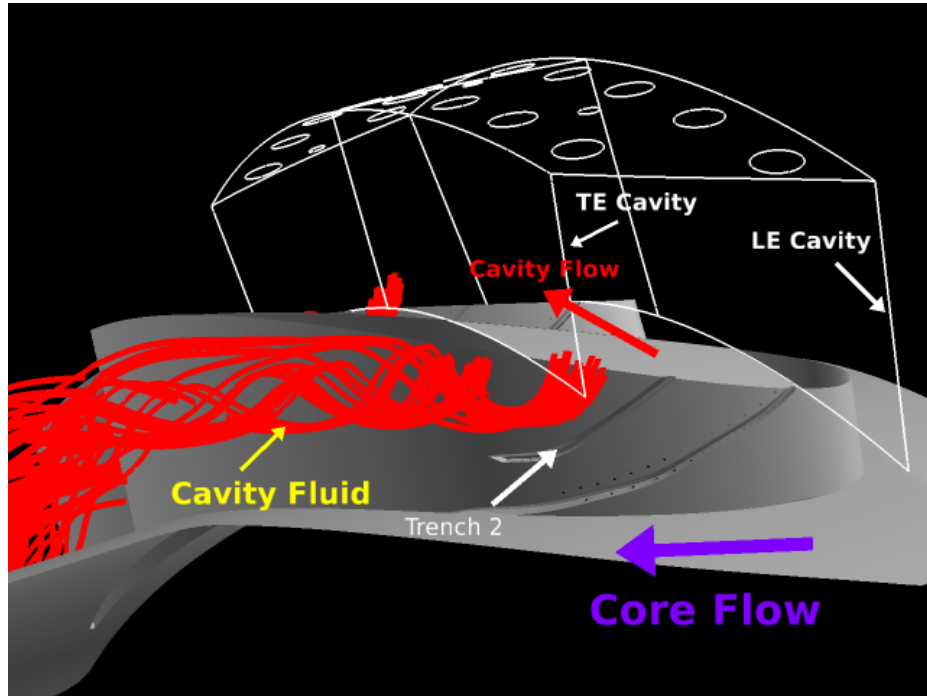


Figure 4.65: Side profile of cavity vortex forming along the suction side surface for Hybrid coolant geometry, $M=2$ Case

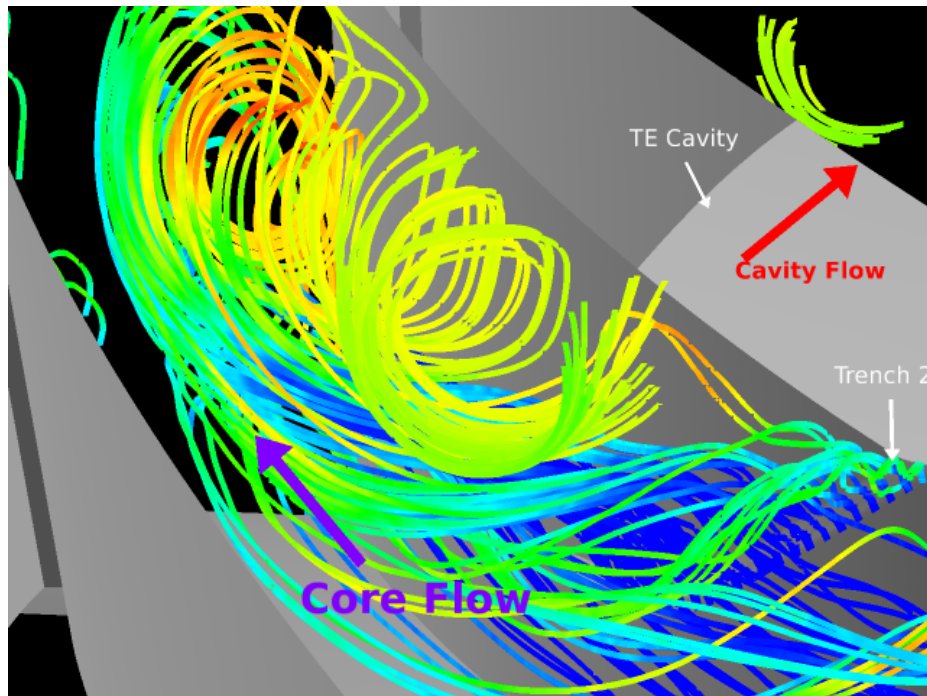


Figure 4.66: Temperature colored streamline out of the cavity interacting with coolant

4.4.2 Temperature Distribution. The temperature distribution of the hybrid geometry was very interesting when the temperature contours were plotted on the surface. In Figure 4.67, the result of the hybrid vane is shown and compared against the baseline model and first two coolant geometries, the heat loads have been significantly removed. For all the geometries a heated zone near the trailing edge section of the vane experienced temperatures above 2200K. This geometry reached a value of 2257K at the trailing edge. Under the circumferential cavity, temperatures around 2500–2700K are seen just before and after the second trench. The hybrid geometry cooled the surface of the airfoil by about 50%. As seen from the coolant migration through the UCC. In Figure 4.68, the temperature contour planes show that burning still does occur as it convects out of the UCC but away from the vane surface as shown in plane B, C, and D.

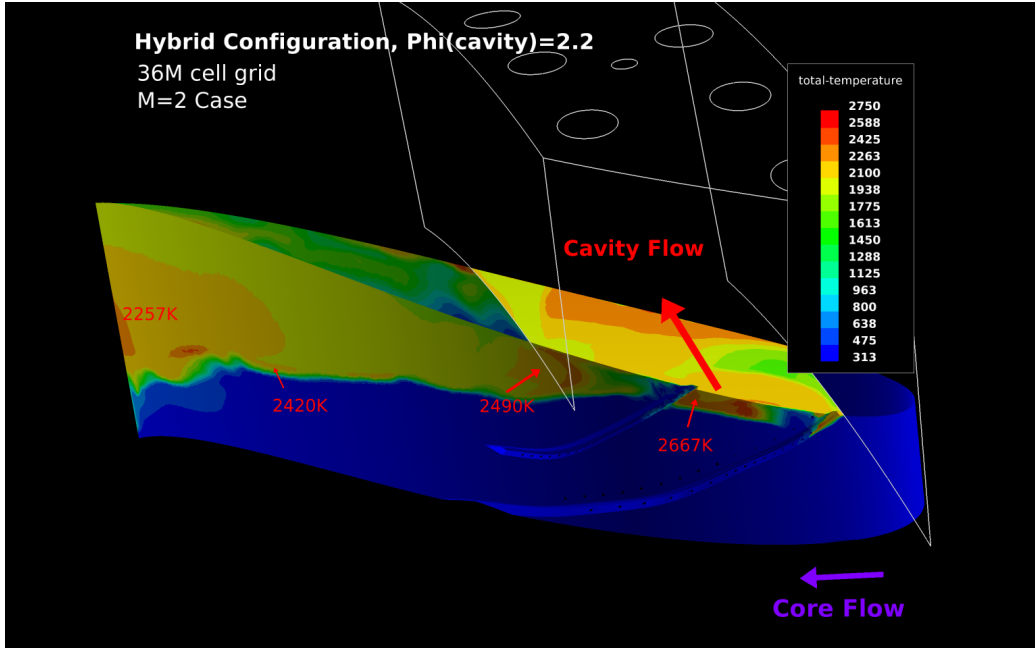


Figure 4.67: Hybrid geometry temperature distribution, M=2

Cutting the airfoil in the spanwise direction and looking at the temperature contours, Figure 4.69 shows the comparison of the baseline model to the hybrid coolant design. Figure 4.69b shows that at 30% span the vane remains cool until location E as the reactions occur off of the vane wall. The same behavior is seen for the 50%

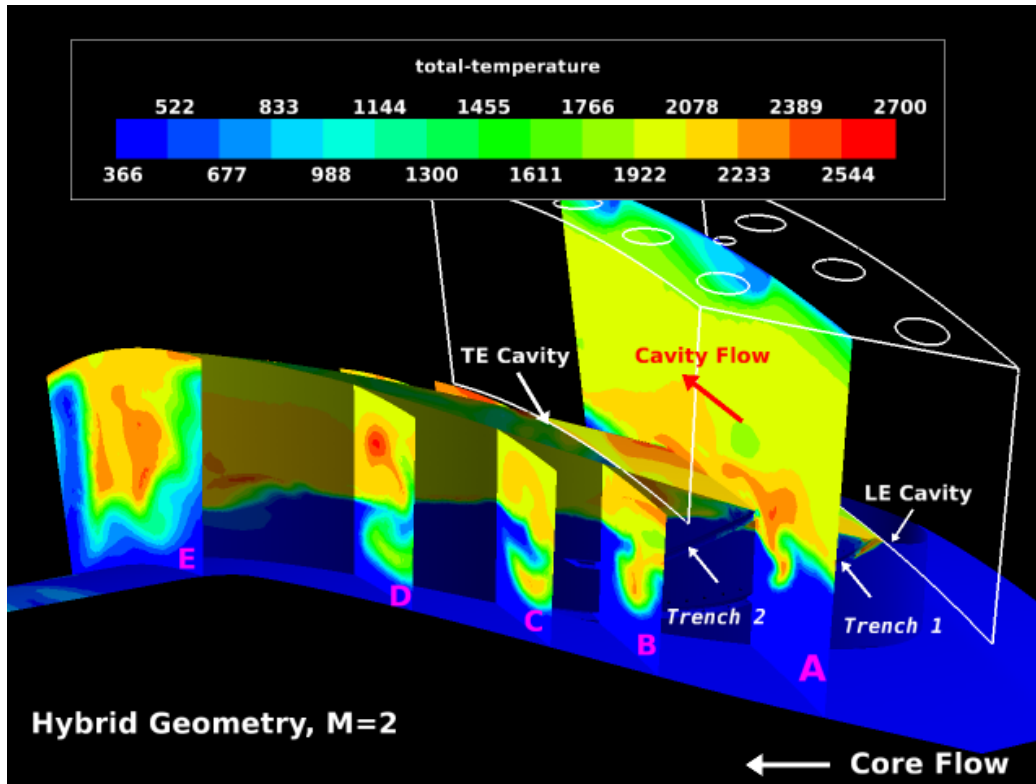
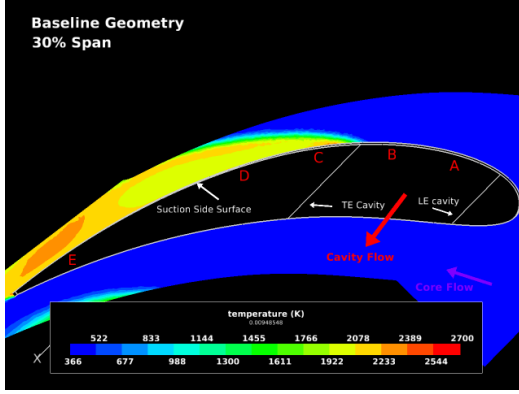
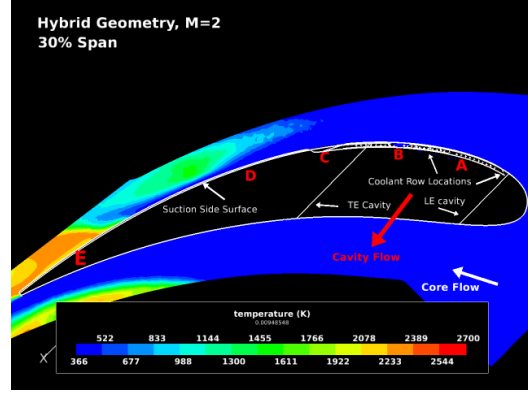


Figure 4.68: Hybrid geometry radial temperature distribution, $M=2$

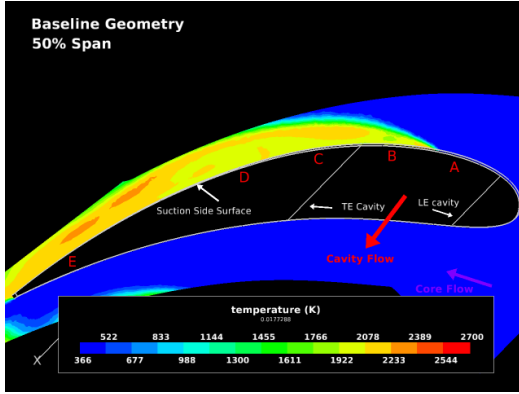
spanwise cut in Figure 4.69d. Looking closer to the 50% spanwise cut in Figure 4.69d, the start of reactions begin at location B just like the baseline model shown in Figure 4.69c. It appears here that burning away from the vane surface allows a cooler buffer layer to form between the reaction and vane surface.



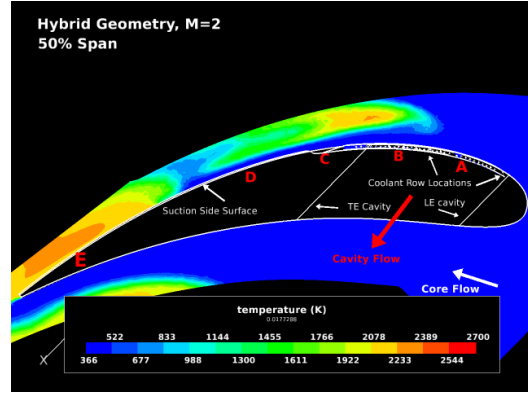
(a) Baseline 30% Span



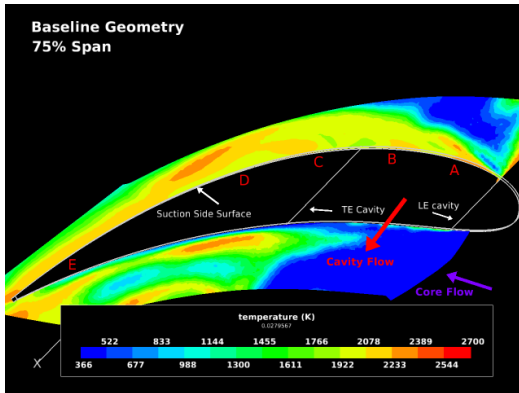
(b) Hybrid Geometry, 30% Span



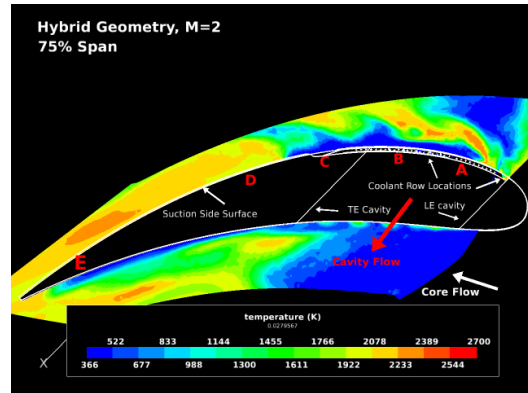
(c) Baseline 50% Span



(d) Hybrid Geometry, 50% Span



(e) Baseline 75% Span



(f) Hybrid Geometry, 75% Span

Figure 4.69: Spanwise temperature of baseline (left column) and Hybrid geometry M=2 case (right column)

4.4.3 Exit Conditions. In comparing the Hybrid geometry against all the coolant configurations studied, the Hybrid geometry had the most pressure losses of 10.2%. The spanwise average temperature distribution in Figure 4.70 shows that at 40% span and above the temperature distribution is superior. Figures 4.72-4.74 show that the concentration of fuel remains near the upper endwall region. For each of the streamwise locations, the spanwise average plots further support the fact that coolant entraining the exhaust fluid kept the fuel above 40% span. Figure 4.72 clearly illustrates the concentration of fuel at the upper endwall location. Figure 4.74 shows the Hybrid geometry having the least amount of fuel at the UCC exit. To further determine if unreacted species have come to completion before exiting the UCC, CO and CO₂ spanwise-average data were analyzed. Based on the CO data in Figures 4.75-4.77, the plots show the concentration of the CO to be near the upper endwall surface. At location D (outside of the cavity section), the amount of CO was not different compared to the baseline model. Further downstream of the UCC at location E, the Hybrid geometry had the most CO concentration compared to the baseline, contoured trench and normal hole configurations. A larger amount of CO indicates that fuel has broken down to carbon monoxide. The lesser amount of CO indicates either reactions have fully completed or fuel has not broken down to CO. When reactions have fully complete, more carbon dioxide should be available. Figure 4.79 shows that at location E more CO₂ is available indicating that final oxidation of carbon monoxide is occurring. Although these reactions due occur upstream, at the exit of the UCC for the Hybrid geometry the maximum amount of CO₂ available does not exceed the baseline case. In light of this knowledge, the small amount of the fuel and CO at the exit is more likely due to dilution from the coolant.

Table 4.3: Exit condition comparison for all geometries

Case	Mach	Profile Factor	Pattern Factor	$\frac{dp}{P}\%$
Baseline	0.280	0.40	0.71	10.5
Contoured, M=2	0.307	0.72	0.77	9.3
Normal Hole, M=2	0.319	0.54	0.57	9.6
Hybrid Design, M=2	0.349	0.48	0.85	10.2

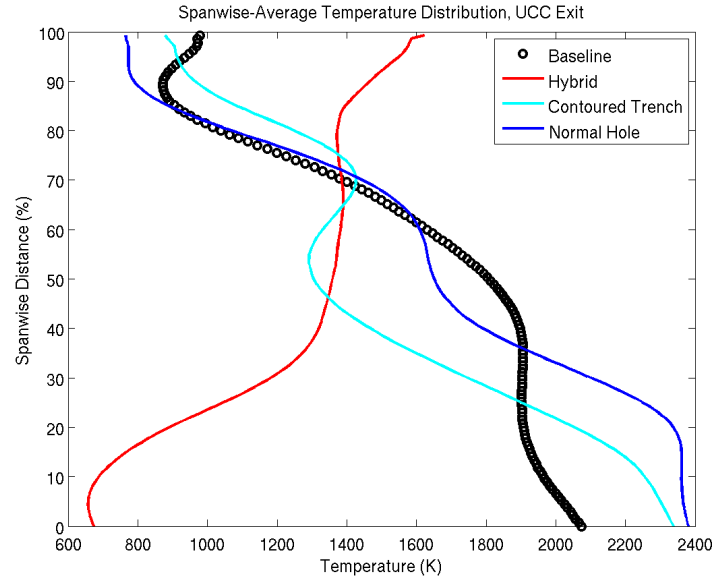


Figure 4.70: Spanwise-temperature average at UCC exit for Hybrid geometry, M=2

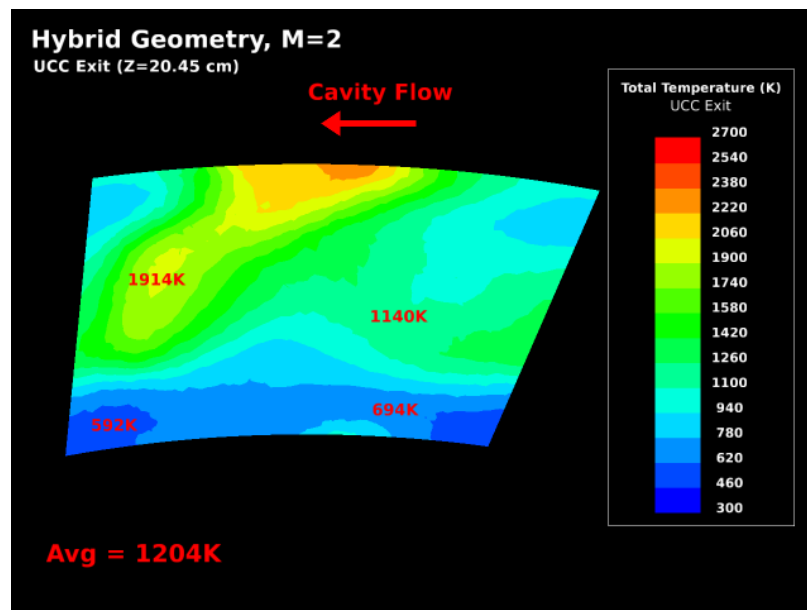


Figure 4.71: UCC exit temperature contour for Hybrid geometry, M=2

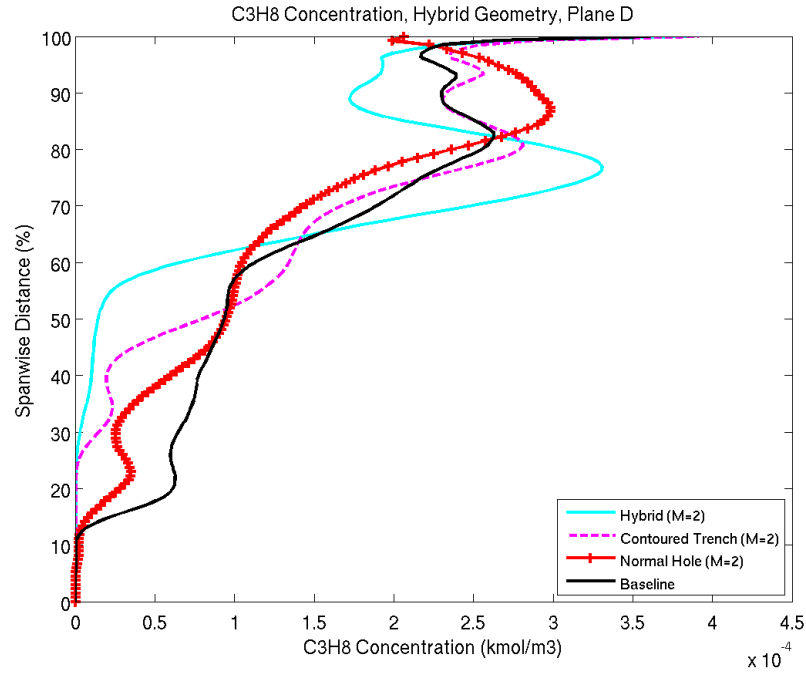


Figure 4.72: Spanwise-average C_3H_8 concentration at location D (150D)

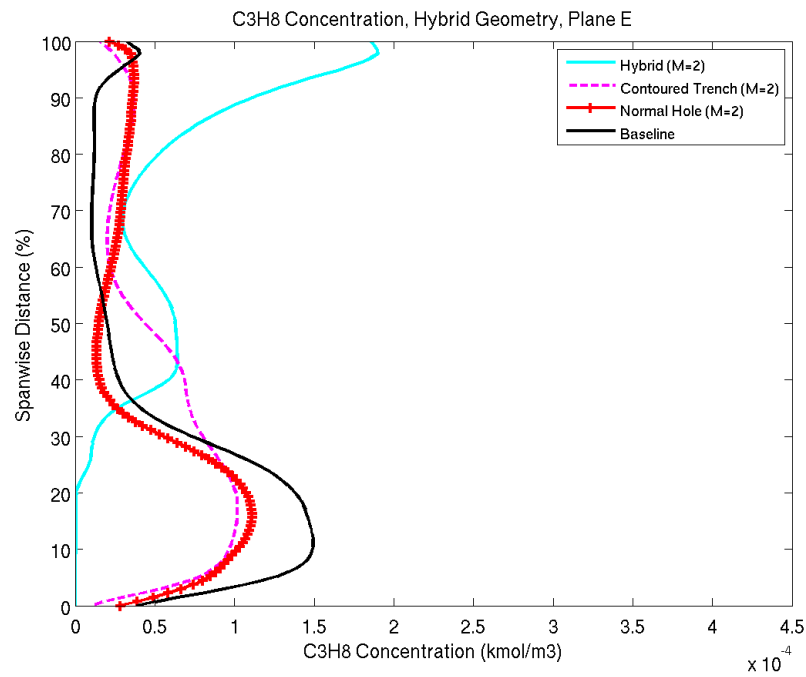


Figure 4.73: Spanwise-average C_3H_8 concentration at location E (200D)

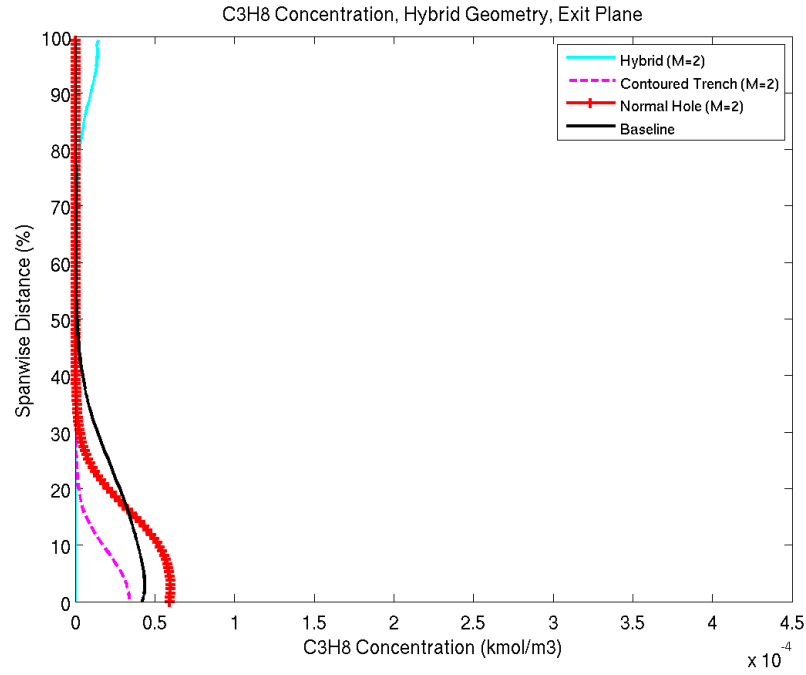


Figure 4.74: Spanwise-average C_3H_8 concentration at UCC exit

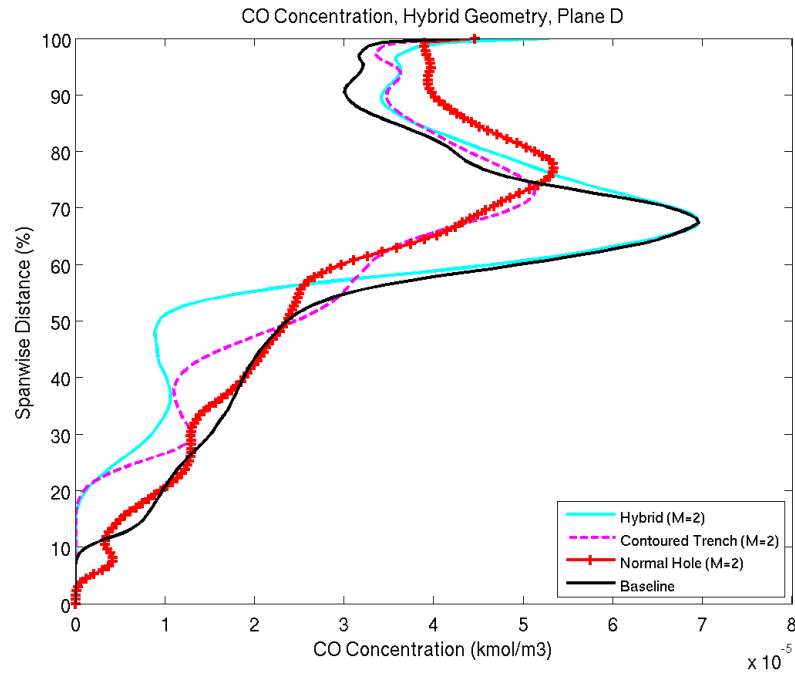


Figure 4.75: Spanwise-average CO concentration at location D (150D)

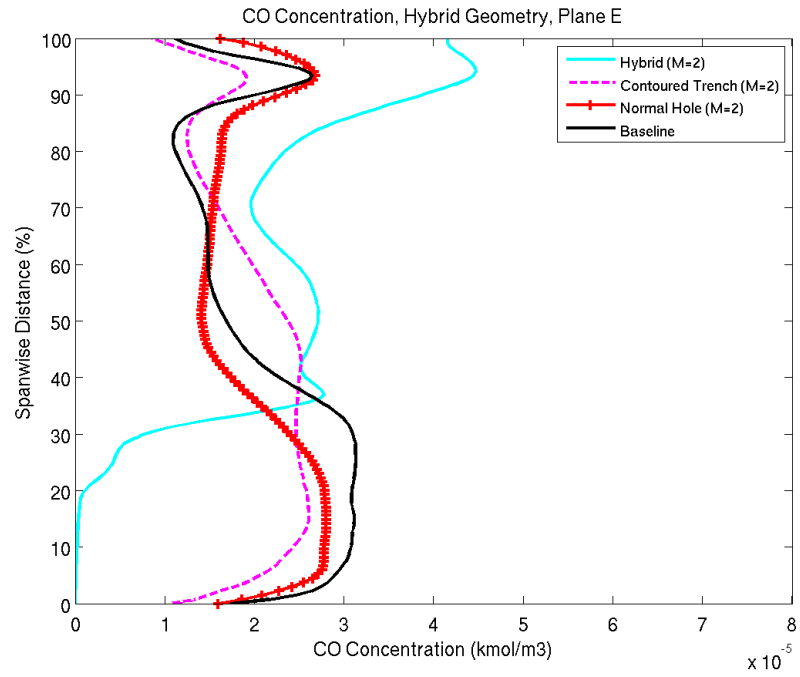


Figure 4.76: Spanwise-average CO concentration at location E (200D)

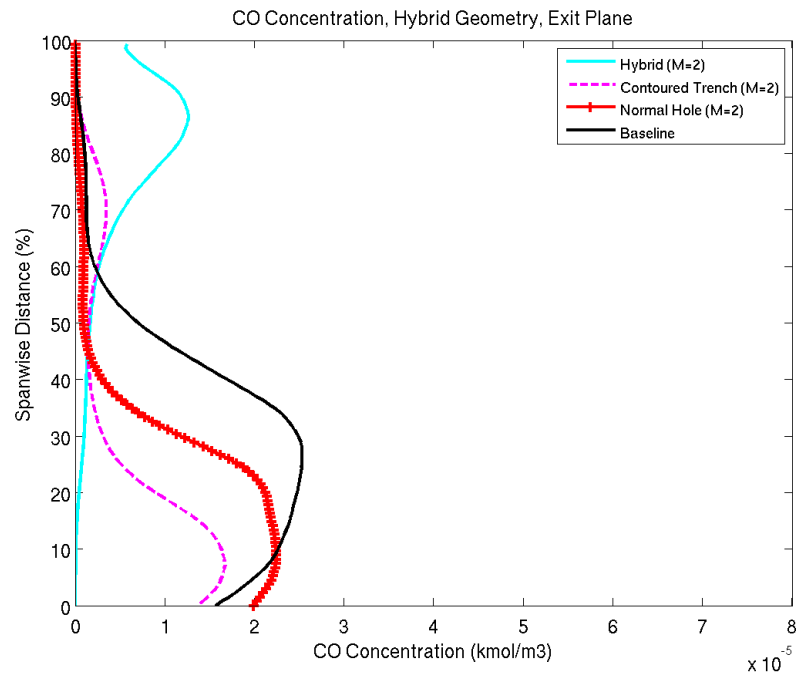


Figure 4.77: Spanwise-average CO concentration at UCC exit

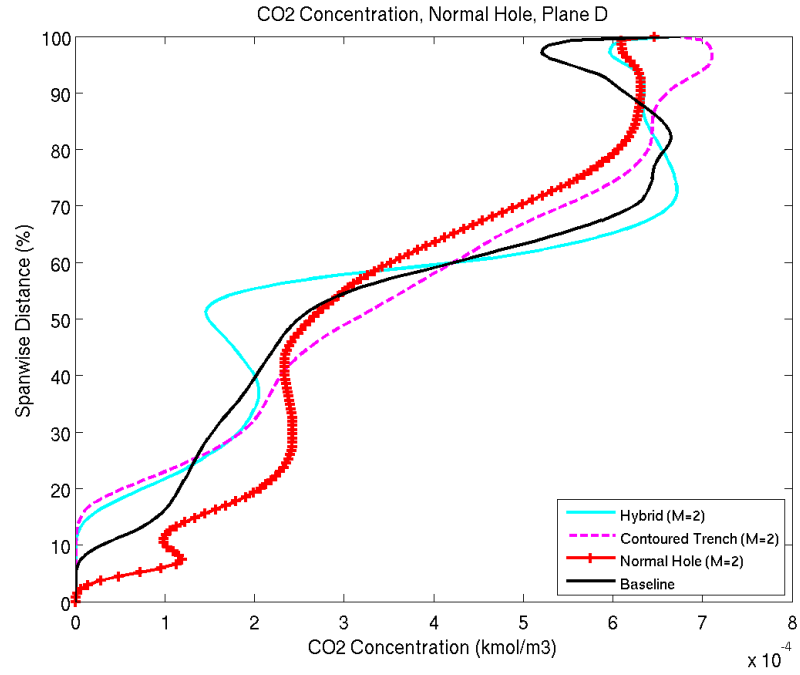


Figure 4.78: Spanwise-average CO_2 concentration at location D (150D)

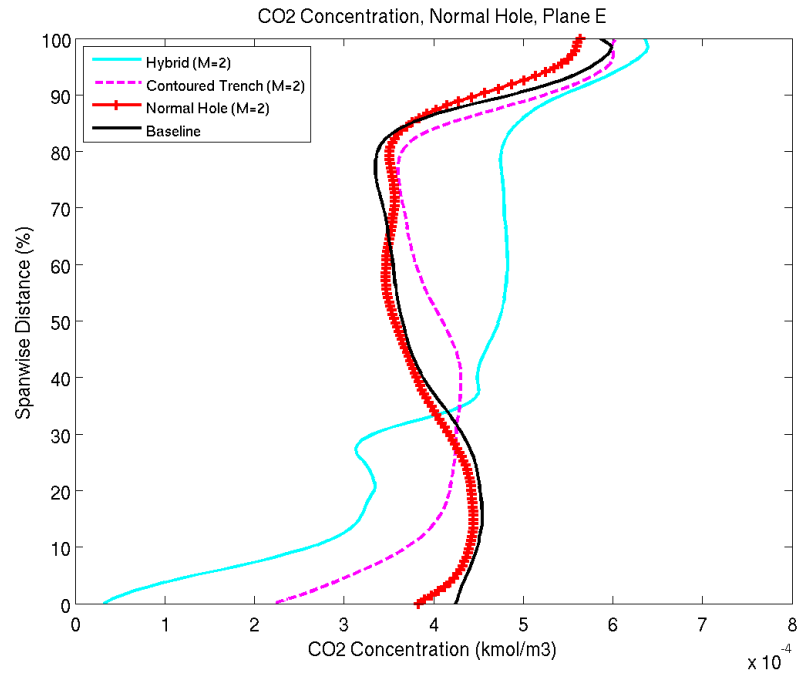


Figure 4.79: Spanwise-average CO_2 concentration at location E (200D)

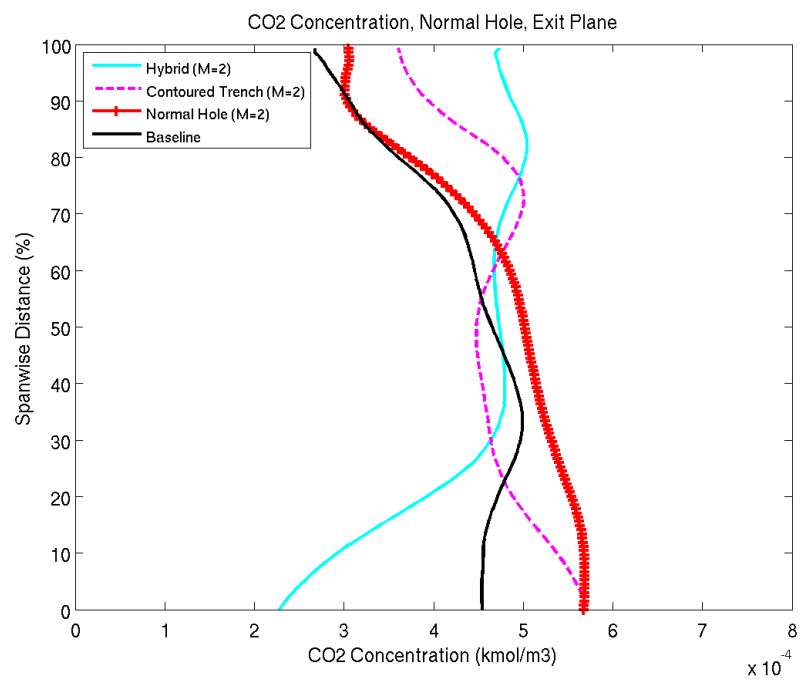


Figure 4.80: Spanwise-average CO₂ concentration at UCC exit

V. Conclusions

5.1 Overview

As an exploratory study, film cooling was applied in order to address the problem of thermal stresses within the UCC. For this initial study, film-cooling research was focused on the suction side of the hybrid vane by using three coolant hole configurations: contoured trench, normal hole and hybrid design. The objective was to investigate the use of three film-cooling configurations and study the fluidic interaction between the circumferential cavity and axial core flow as coolant was introduced into the freestream. In addition, an investigation on the potential for secondary reactions to occur as the fluid exits into the turbine section was considered. Based on the results from the film-cooling analysis, the data revealed that secondary reactions would occur in the UCC.

5.2 Major Findings

For the normal hole geometry and contoured trench geometry, the secondary reactions helped in reducing the potential of the heat release to occur in the turbine section. Consequently though for the contoured trench design, higher heat loads are expected to occur on the vane surface as the exhaust fluid from the cavity interacts with the coolant fluid. For both normal hole and contoured trench design, the coolant separated away from the vane. For the normal hole configuration, the coolant separated further away from the vane surface than the contoured trench design and as a result extreme temperatures on the vane surface did not appear. Higher heat loads above 2200 K started to appear for a blowing ratio of 1.5 and became even more apparent for a blowing ratio of 2.

While the completion of reactive species was seen at the exit of the UCC, the desired temperature distribution was not achieved. Excess heating (2400 K) on the lower endwalls was predicted for both the normal hole and contoured trench design. The Hybrid geometry on the other hand significantly kept the lower vane surface and bottom endwall surface cooler (370 K). The reason for this is because the tapered

trench design helped to entrain the hot exhaust fluid exiting the circumferentially section and prevent it from reaching the lower endwall surface as it convects out of the UCC.

A major finding for this research was that vortices shed from the circumferential cavity section played a large role in the fluid dynamics of the coolant geometries. For each of the cases, the coolant did not remain attached as the blowing ratios were varied. It was found that the cavity fluid immediately rolled against the suction side surface of the vane and pushed the coolant away from the vane degrading the film-cooling effectiveness and led to secondary reactions. Interestingly, the coolant served as a mechanism to draw the secondary reactions away from the vane as seen in the Hybrid geometry.

The results of this research also revealed that secondary reactions helped to reduce the potential for unreacted species to enter into the turbine section and lead to additional heat release. Based on the spanwise average data for C_3H_8 , CO , and CO_2 at the UCC exit, the results dispel the argument that secondary reactions should be avoided within an engine [18]. With this being the first study on film cooling the UCC, more work must be done on optimizing a coolant scheme to further exploit the use of secondary reactions.

5.3 Future Recommended Work

For the three coolant geometries studied for this effort, the numerical analysis gave a general understanding of the flow behavior within the UCC as film coolant is applied in the UCC. An optimal design has not yet been developed, but the initial work done here give insights into the type of design needed. Additional investigation should be done using different coolant hole configurations, such as fan-shaped holes, laid-back fan-shaped holes and angled circular holes. It would be advantageous to investigate whether these configurations would keep the coolant attached to the vane surface. Coolant hole placement is also another area of research that should be studied. Placing coolant holes on the top or bottom of the endwalls may possibly help by keeping the

endwalls cool and forcing the reactions to occur at the mid-span location which may help with temperature distribution at the exit.

As the cavity fluid played a large role in this study, various geometric studies should be done on either breaking up the cavity vortex or directing the fluid in a certain direction. The sharp intersection of the trailing edge cavity wall and upper endwall surface could possibly trip the cavity fluid at it exits out of the cavity. A rounded intersection should be tested to determine if the cavity vortex lessens.

As secondary reactions occurred in the UCC, the coolant holes experienced extreme heating during the process. Numerical and experimental studies should be done on addressing the issue of burning near the holes.

To validate whether unreacted species are completely reacted, it would be advantageous to conduct experimental studies to quantify the emissions at the exit of UCC when secondary reactions occur upstream.

For this research effort, the goal was to lay the groundwork for a cooling scheme design for use within the Ultra-Compact Combustor. While the current study was done for a laboratory rig environment, it is desirable to conduct similar numerical tests at conditions more representative of an actual combustor. Ultimately, experimental tests on vanes with coolant holes in a UCC rig model under realistic flow conditions should be done.

Appendix A. Rayleigh Study

In addition to the film-cooling study, a numerical study was completed to investigate the exit condition of the UCC into the turbine section. Based on discussions with AFRL [4], the desired exit condition of the UCC is a Mach 0.8 value into the turbine section. The current UCC model studied by Bohan [6] does not exit into the turbine at the desired conditions. The goal of this objective was to numerically investigate a proposed UCC geometry that attempts to raise the exit Mach condition. Given that the focus of the study was to raise the Mach number in the UCC, the UCC would be more susceptible to Rayleigh pressure losses as it operates at higher Mach numbers. According to Saravanamuttoo et al. [9] Rayleigh flow is the relationship in the change of momentum of a flowing gas caused by heat addition. As heat is added to a subsonic flow in a duct of constant area, a drop in pressure must be accompanied with the heat addition in order to provide the force required to accelerate the flow and satisfy the momentum equation. The change in pressure in turn leads to changes in flow speed. If the gas flow is subsonic, the addition of heat increases the flow towards Mach 1, and for supersonic flow the addition of heat lowers the speed to Mach 1. In light of Rayleigh theory, the numerical study was aimed at investigating the Rayleigh losses of the current UCC configuration and a “Rayleigh-free” UCC configuration.

A.1 Rayleigh Geometry

The geometry analyzed for this effort was based on a 2-D heat release study conducted by Wilson [30]. As an effort to improve the exit Mach condition as well as minimize the losses expected in a large scale UCC, Wilson varied the cross-section of the UCC to manage the velocity thus Mach speed in order to control the losses due to Rayleigh effects. His study predicted a UCC geometry that would complete the burning process in a low Mach number regime by expanding the cross-section of the UCC. The UCC was then contracted downstream with the goal to achieve a Mach number of 0.8 expected for a representative turbine section.

In Figure A.1, the endwall dimensions of the UCC Rayleigh geometry considered is shown. Here the endwall surfaces are plotted showing its radial position with respect to the centerline axis of the UCC. In Figure A.2, a layout of the modified UCC geometry is shown. The core axial flow goes from right to left and the flow within the cavity section goes into the plane. The hybrid vane height is 18 cm from endwall to endwall as shown in solid gray. While varying the cross-sectional area of the UCC, the upper endwalls and cavity section was held fixed and the dimensions set the same as Bohan [6]. The length of the square cavity was 4.83 cm, and twenty hybrid vanes were situated below the cavity section.

The same mesh generation practice described Section 3.3.2 was used to create a three-dimensional unstructured volume mesh within Gridgen. Using periodic boundary conditions, a single vane was computationally modeled resulting in a mesh size of five million mixed element computational cells.

A.2 Computational Setup

For the study, Fluent[®] 6.3 CFD software was used to simulate a combustion model of the UCC. The solver settings include a 3-dimensional, node centered, steady state, pressure-based solver with second order accuracy for momentum, density and energy with SIMPLE algorithm used for pressure-velocity coupling. From the results of Bohan [6] as well as Hermanson and Thole [27], the RNG k- ϵ turbulence model proved to be sufficient in capturing the secondary flows existing in the UCC due to the anticipated vortex shedding on the leading edge of the vane. For the film-cooling analysis, SST k- ω model was used in order to accurately model the coolant behavior close to the surface of the vane wall. From the turbulence comparison test, described in Section 3.2.1, the SST k- ω model required 3000 iterations while the RNG k- ϵ model required only 400 iterations to converge. Given that the turbulence model used by

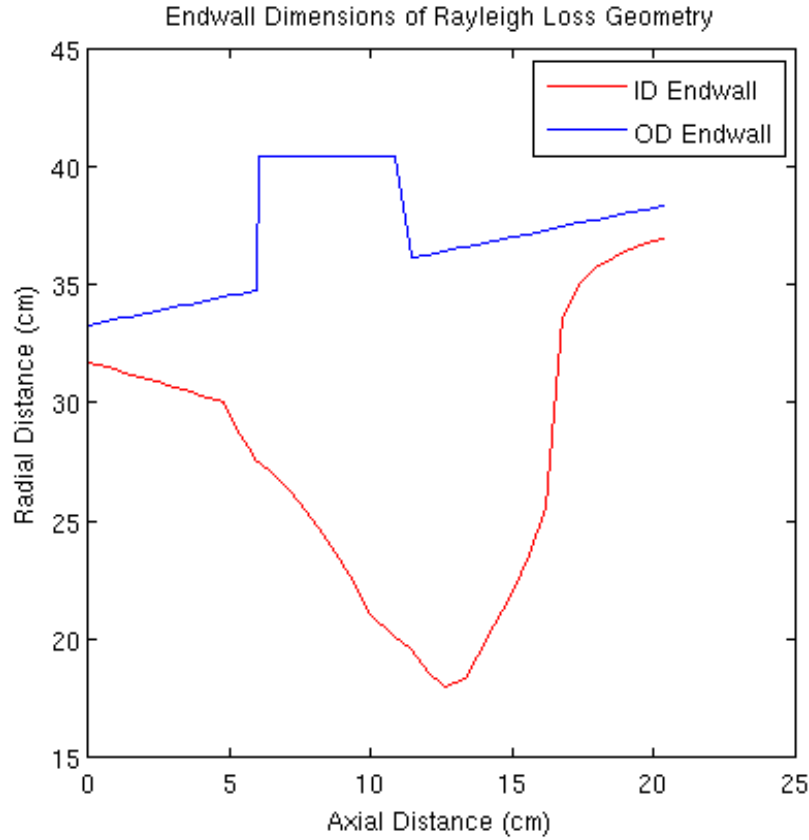


Figure A.1: Endwall dimensions of UCC Rayleigh study

Rayleigh Geometry Schematic

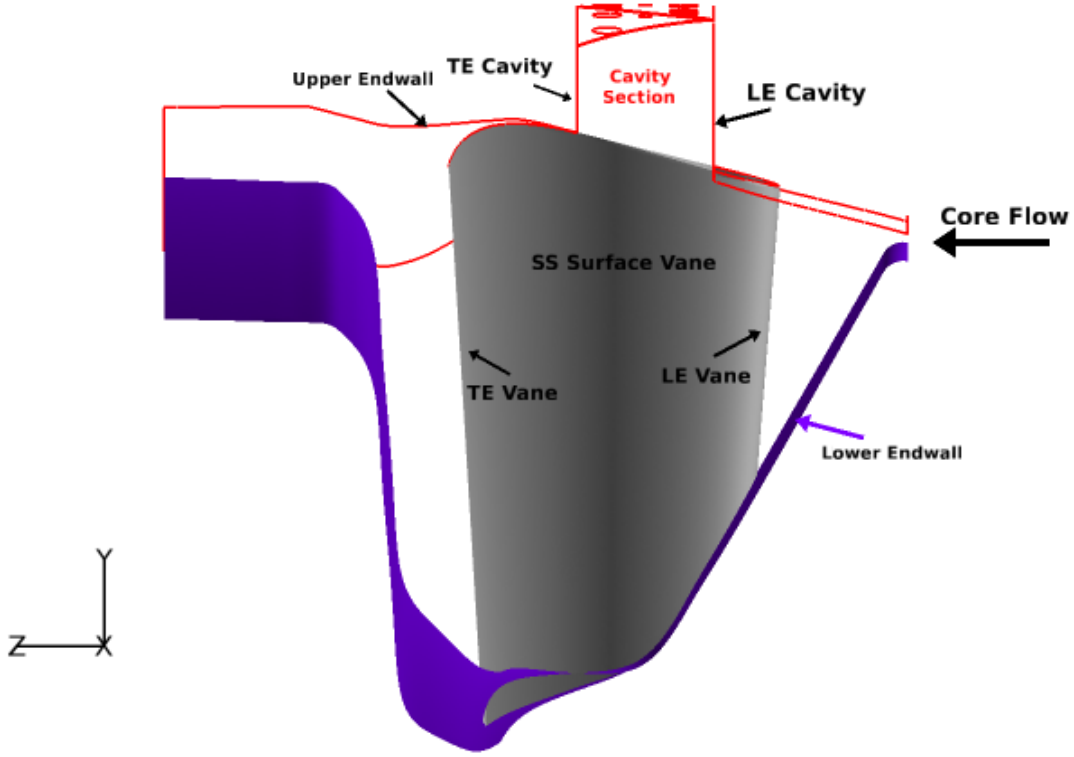
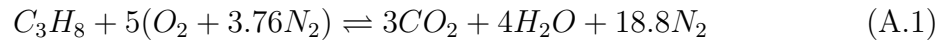


Figure A.2: Schematic layout of Rayleigh geometry

Bohan [6] captures the flow features within the UCC and less computational time was required for the RNG $k-\epsilon$ model, the RNG $k-\epsilon$ turbulence model was employed.

To further simplify the computations and obtain an overall global understanding of the combustion behavior in the UCC, a single-step chemical reaction scheme was employed and is shown in Equation A.1. Here the combustion of propane-air is represented and was modeled for this study. Eddy dissipation model was selected in order to handle turbulence-chemistry interactions.



A.2.1 Numerical Results. For the start of this analysis, the flow field within the UCC was investigated. A two-dimensional view, shown in Figure A.3, shows the

velocity vectors of the core flow as it enters the UCC. From this view, the vectors reveal the flow entering into the UCC and curling up towards the upper endwall then back into the core flow. At the lower endwall, another recirculation zone is formed as shown in Figure A.4. This indicates that separation must be occurring within the UCC. Seeding the core flow as it enters into the UCC shows that in fact separation is present (see Figure A.5).

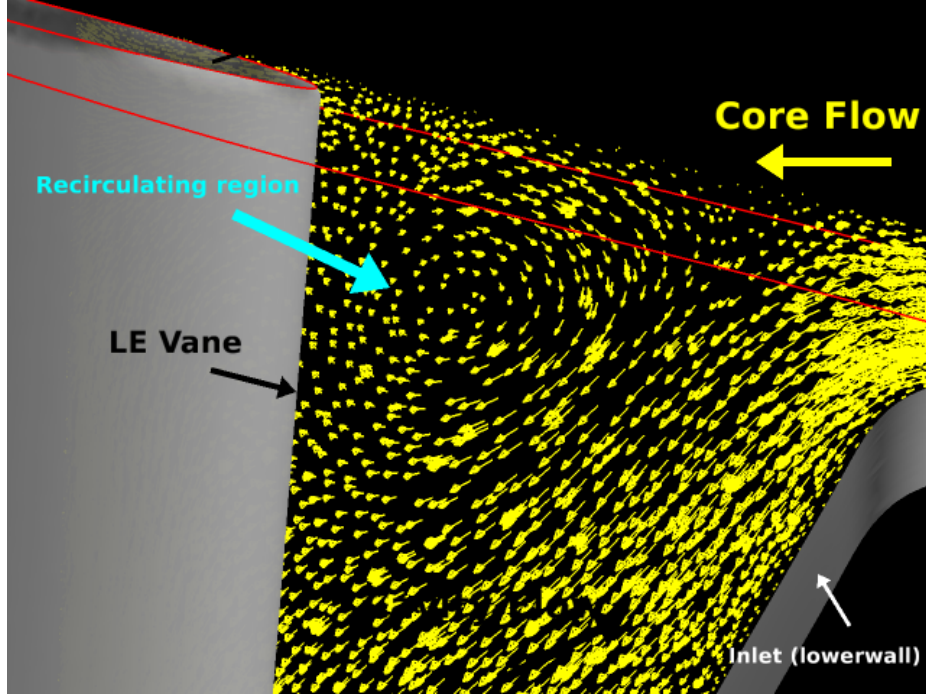


Figure A.3: Velocity vector of leading edge circulation within Rayleigh geometry

In regards to the cavity and core flow interaction, Figure A.6 is also a stream-line view showing the cavity fluid (red) penetrating into the core flow (blue) then convecting downstream. Set against the streamlines is a temperature contour of the hybrid vane showing the pressure side surface of the vane. For the baseline model, heating was only experienced along the suction surface. The curl like feature near the leading edge of the vane is possibly due to recirculation zone previously discussed. With large amounts of mixing near the leading edge of the vane, any unburnt fuel leaving the circumferential cavity and curling upstream as shown in Figure A.6 has great potential toward secondary reactions occurring.

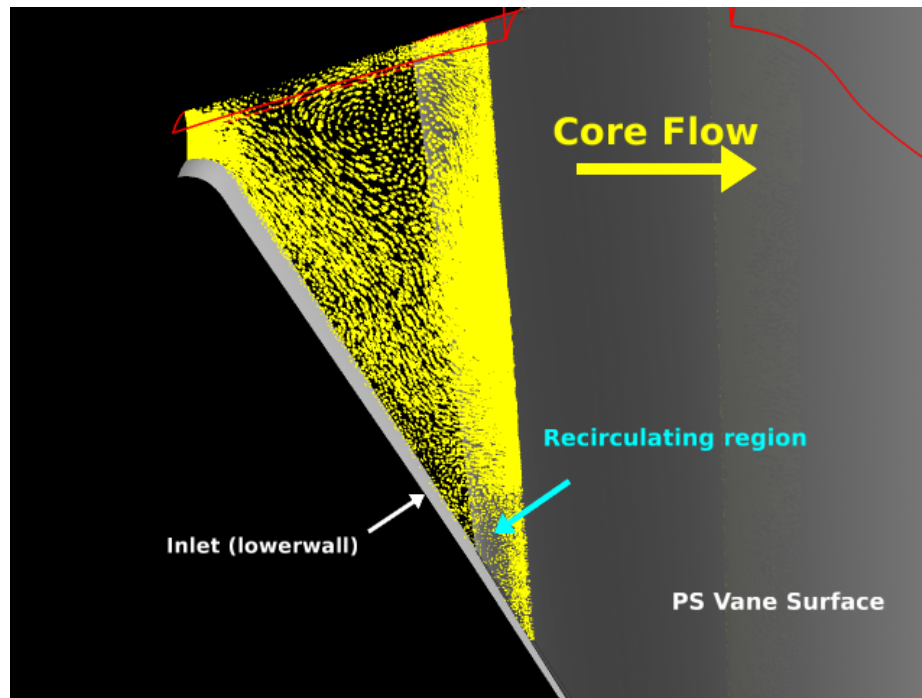


Figure A.4: Recirculation formation near lower endwall within Rayleigh geometry

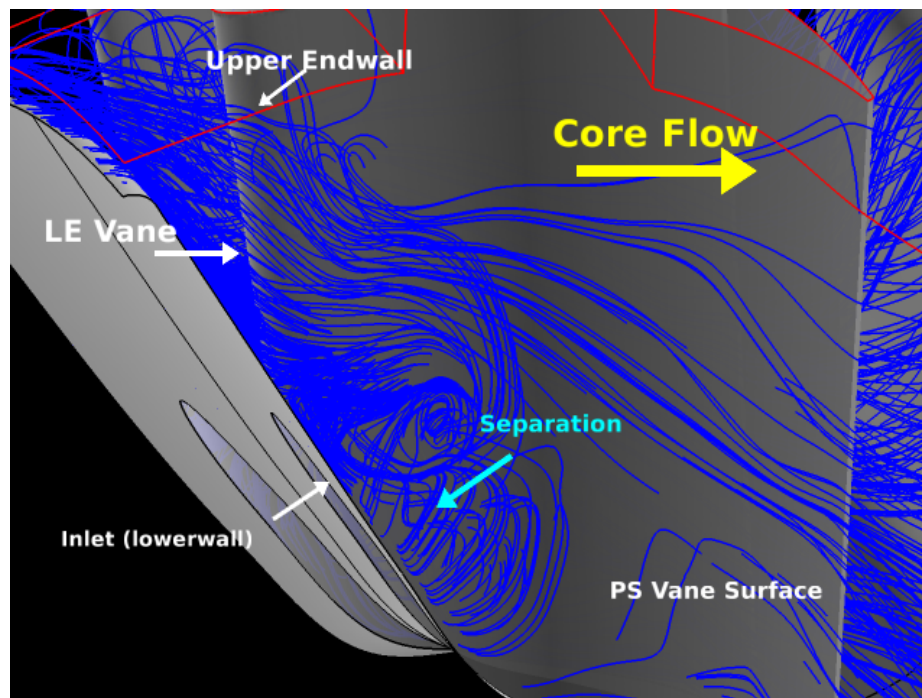


Figure A.5: Streamline view of recirculation formation near lower endwall within Rayleigh geometry

It is quite evident from Figure A.6 that as the exhaust from the circumferential cavity exits into the core flow unburnt fuel remains and is brought to complete reaction, heating the vane surface. In Figure A.7, temperature contour planes are taken in the streamwise direction. Starting from Figure A.7a, heating is noticed along the upper endwall. Taking another step downstream of the UCC at location D, Figure A.7b shows the heat load spreading in the radial direction. In Figure A.7c-f, the temperature contours imply that reactions are occurring both on the pressure side and suction side surface of the hybrid vane. This leads to a crossroad because while at the process of avoiding Rayleigh losses the hybrid vane is experiencing extreme heating on both sides of the surface.

Figure A.9 shows the total temperature and total pressure (area average) values through the UCC in the axial direction and compared against the previous model studied by Bohan [6]. As noted earlier, higher temperatures were noticed upstream because of localized heating near the leading edge of the vane as shown in Figure A.7a. Reviewing the total pressure loss through the UCC, the plot reveals that great im-

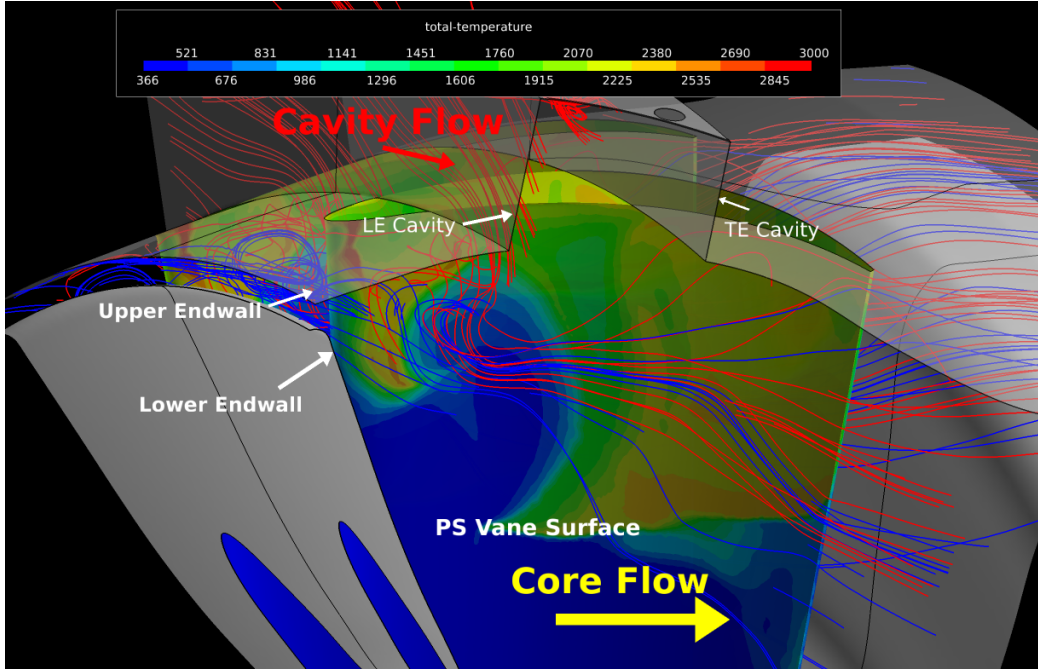


Figure A.6: Streamline view of cavity and core flow interaction

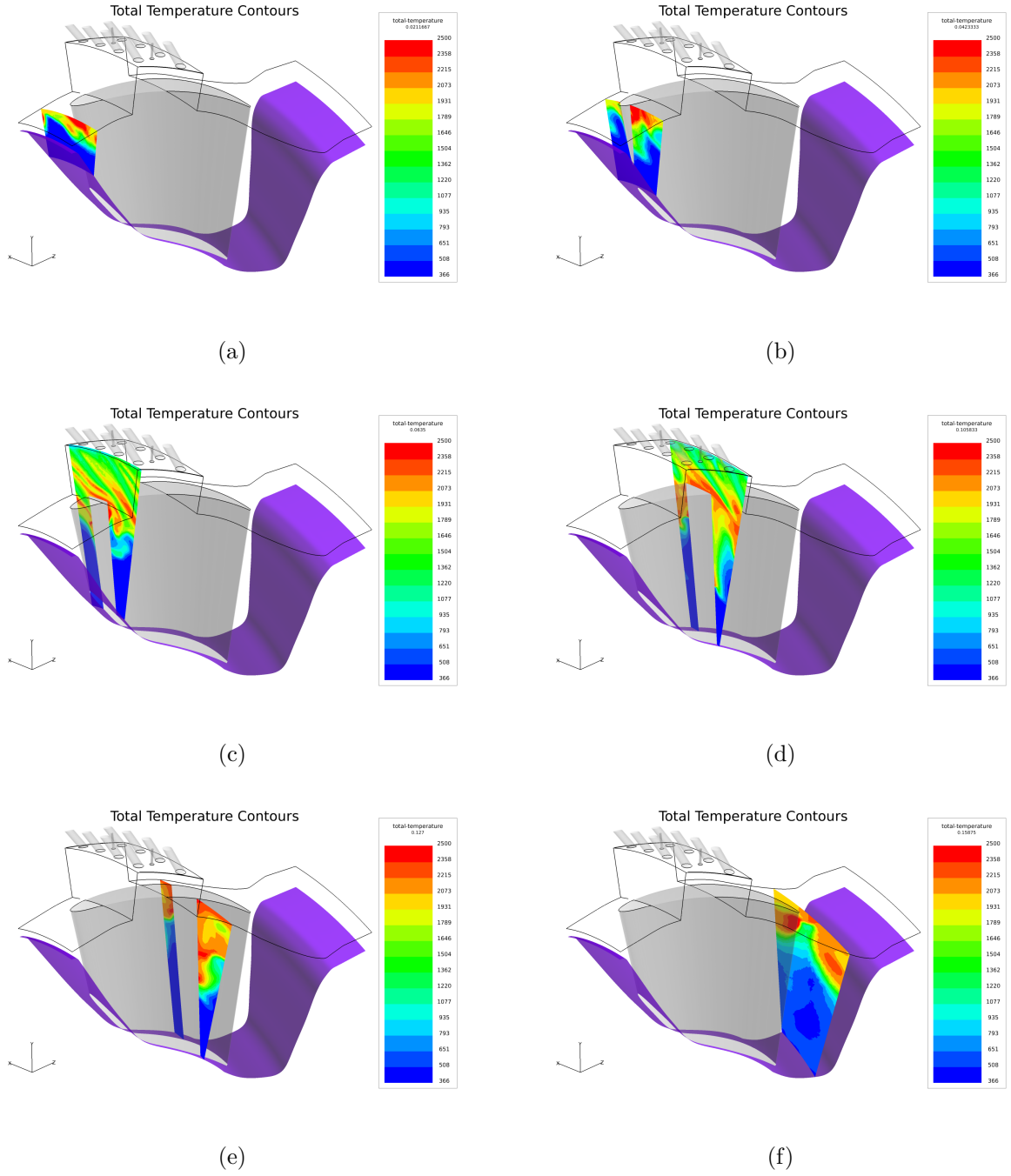


Figure A.7: Temperature contour planes through the UCC for Rayleigh geometry

provement is made with the Rayleigh geometry. Improvement in the pressure loss was from 9.4% to 4.2%. In Table A.1, the pressure losses between the two geometries are summarized.

Table A.1: Total pressure loss results of Rayleigh study					
Geometry	Pressure Type	Domain Inlet (Pa)	Cavity Inlet (Pa)	Domain Exit (Pa)	% Loss
Bohan	Static	115,951	131,303	101325	12.61
	Total	119,212	133,820	108,022	9.39
Rayleigh	Static	103,374	109,921	102,786	0.05
	Total	110,781	110,555	106,115	4.21

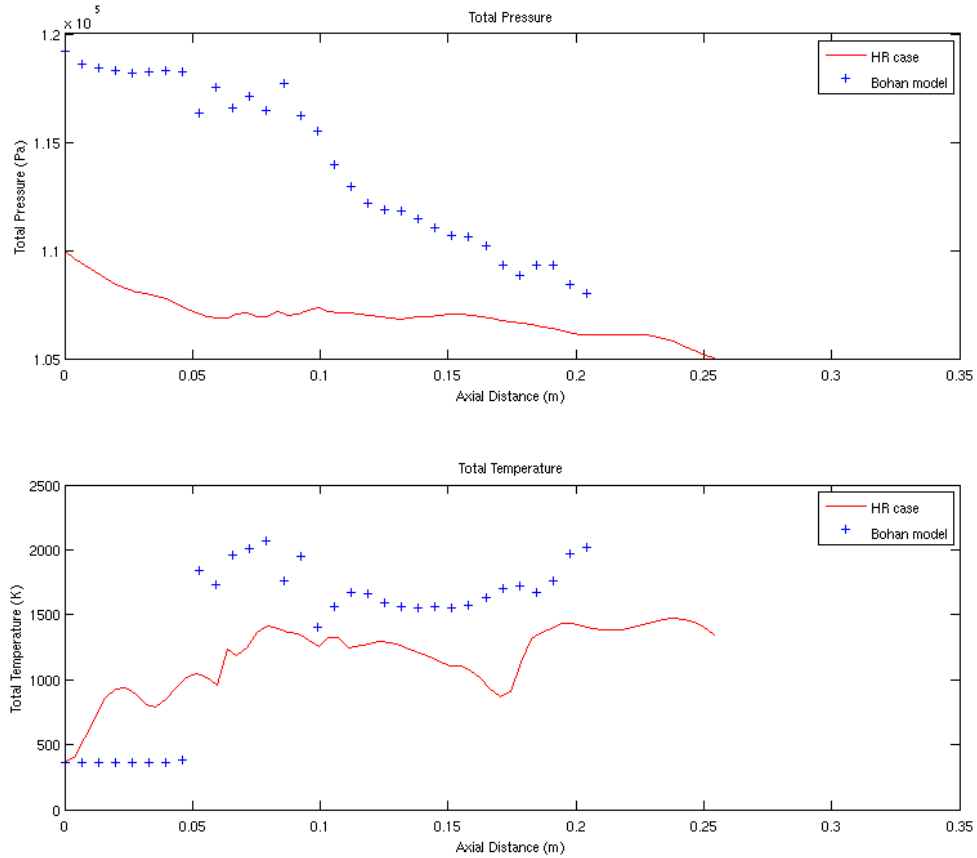


Figure A.8: Total temperature and total pressure area-average values of Rayleigh geometry study

In Figure ??, the plot highlights the cavity region and contraction region for the Rayleigh geometry for the total pressure and total temperature values through the UCC. Here the cavity section was excluded while taking the area averages through

the UCC. The end of the contraction region represents the exit of the UCC. From Figure A.10, the plot shows that the UCC does not exit at Mach 0.8 as desired. At the exit, the Rayleigh geometry achieves a Mach 0.23 in the axial direction and Mach 0.41 when including the swirl velocity component. A possible reason for the lower Mach value that includes the swirl angle is because of the contraction region. As the fluid exited, the axial velocity component sped up while the tangential velocity components reduced. A plot of the swirl angle through the Rayleigh geometry is shown in Figure A.11.

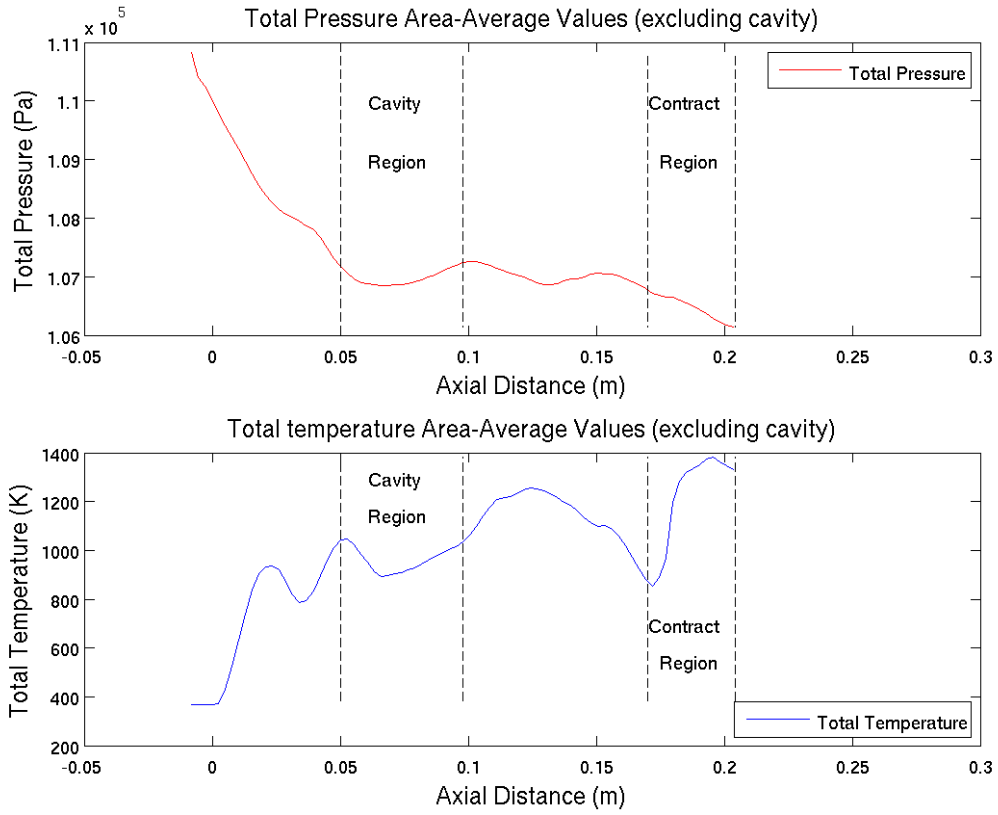


Figure A.9: Total temperature and total pressure area-average values of Rayleigh geometry only

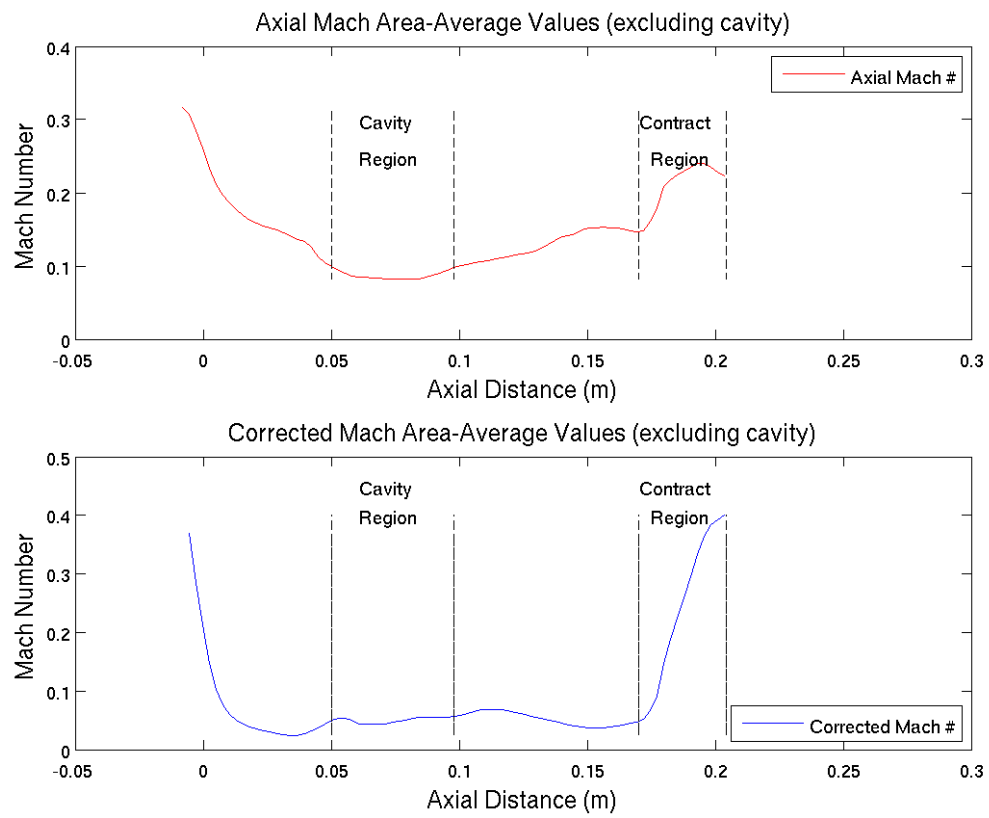


Figure A.10: Mach distribution for Rayleigh geometry

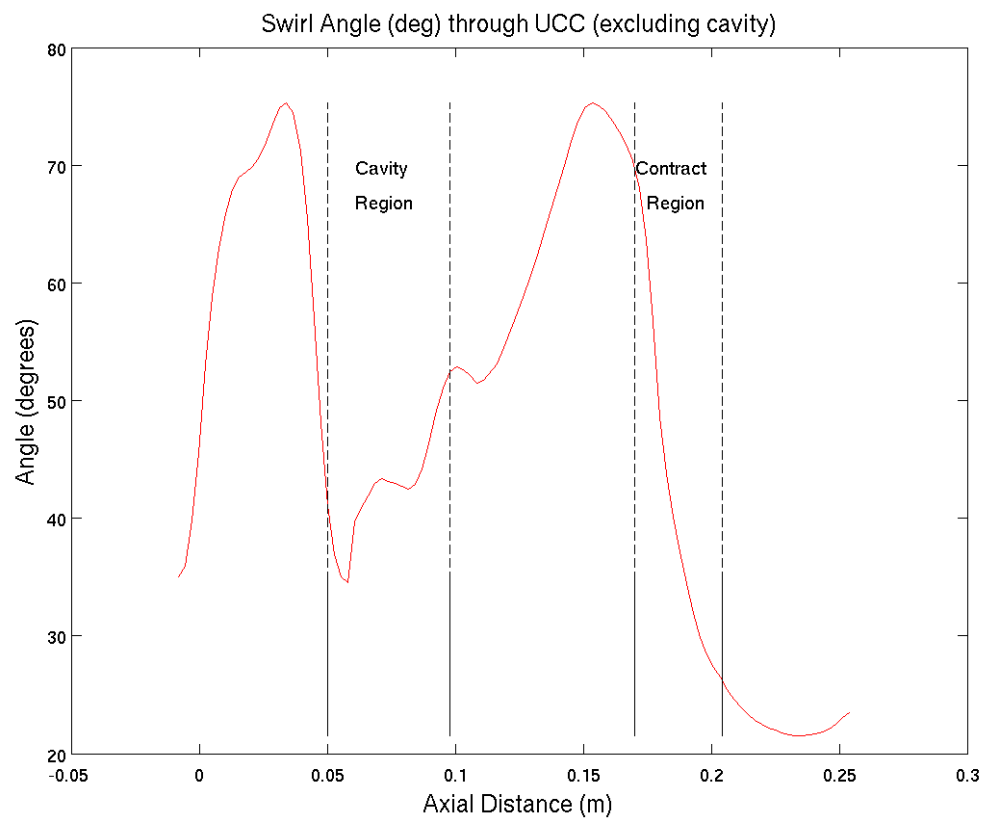


Figure A.11: Swirl angle value through Rayleigh geometry

A.3 Summary

In summary of the results for the Rayleigh geometry analysis, a low Mach regime was accomplished during the combustion process through the UCC. As a result, 50% of the pressure losses for the current UCC geometry were recovered when completing the reactions in a low Mach regime. Consequently though, the results revealed that the Rayleigh geometry requires more optimization. Separation was shown as the flow enters into the UCC. Even though the design is not aerodynamically sound, the improvement to the pressure losses due to heat addition at high Mach number are far better than the baseline configuration. From a durability standpoint, the Rayleigh geometry resulted in unwanted uniform distribution across the hybrid vane. Additional heat loads on the pressure side surface were seen as a result of this geometry. As the flow had lesser momentum because of the expansion within the UCC, the cavity flow had greater momentum and penetrated further into the core flow reacting along both the suction side and pressure side surface of the hybrid vane. Based on the Rayleigh geometry, this drives an even greater importance for cooling the UCC.

Appendix B. Additional Numerical Analysis Results

This appendix includes additional streamline illustrations supporting the the results for the analysis discussed in Chapter 4. The results are presented in the order the geometries were presented in Chapter 4.

B.1 Coolant, Cavity and Core Flow Interactions

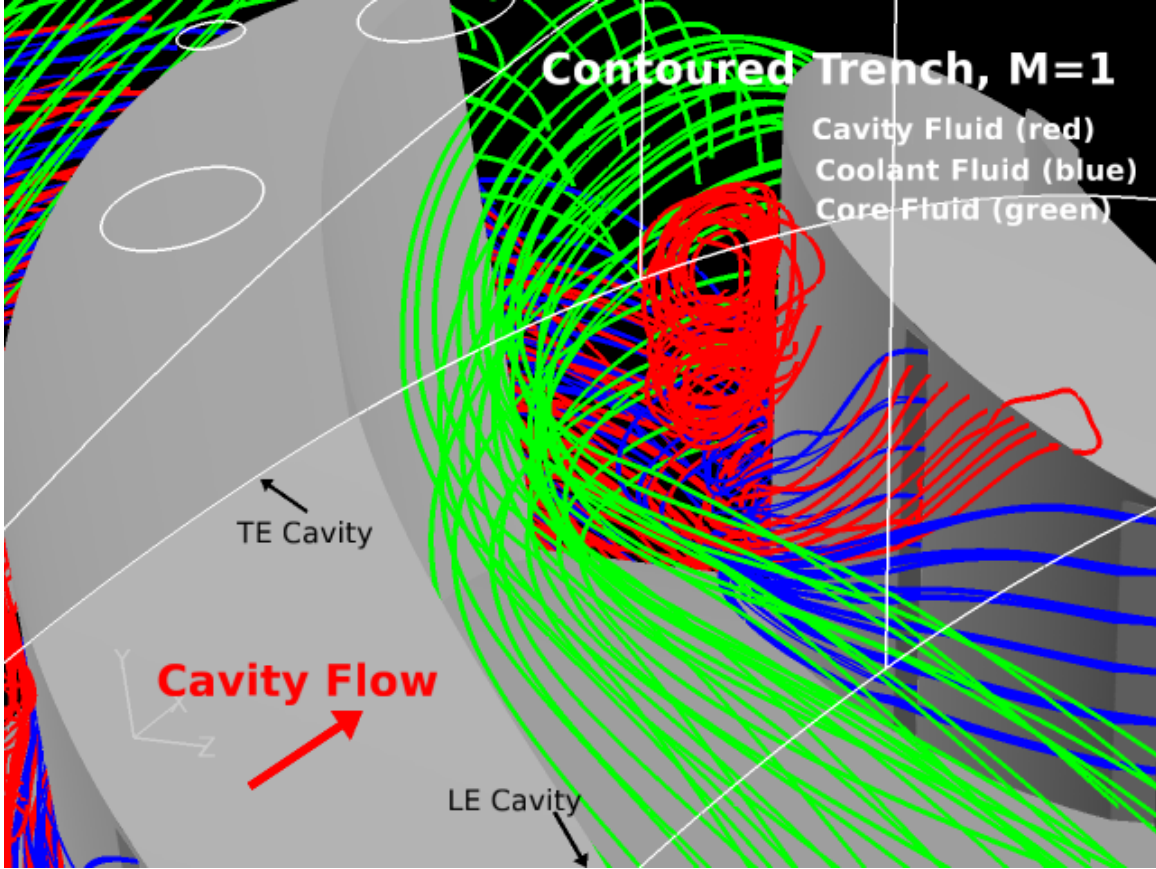


Figure B.1: Contoured trench fluid interaction of cavity fluid (red streamline), coolant fluid (blue streamline) and core fluid (green streamline) for M=1 test case

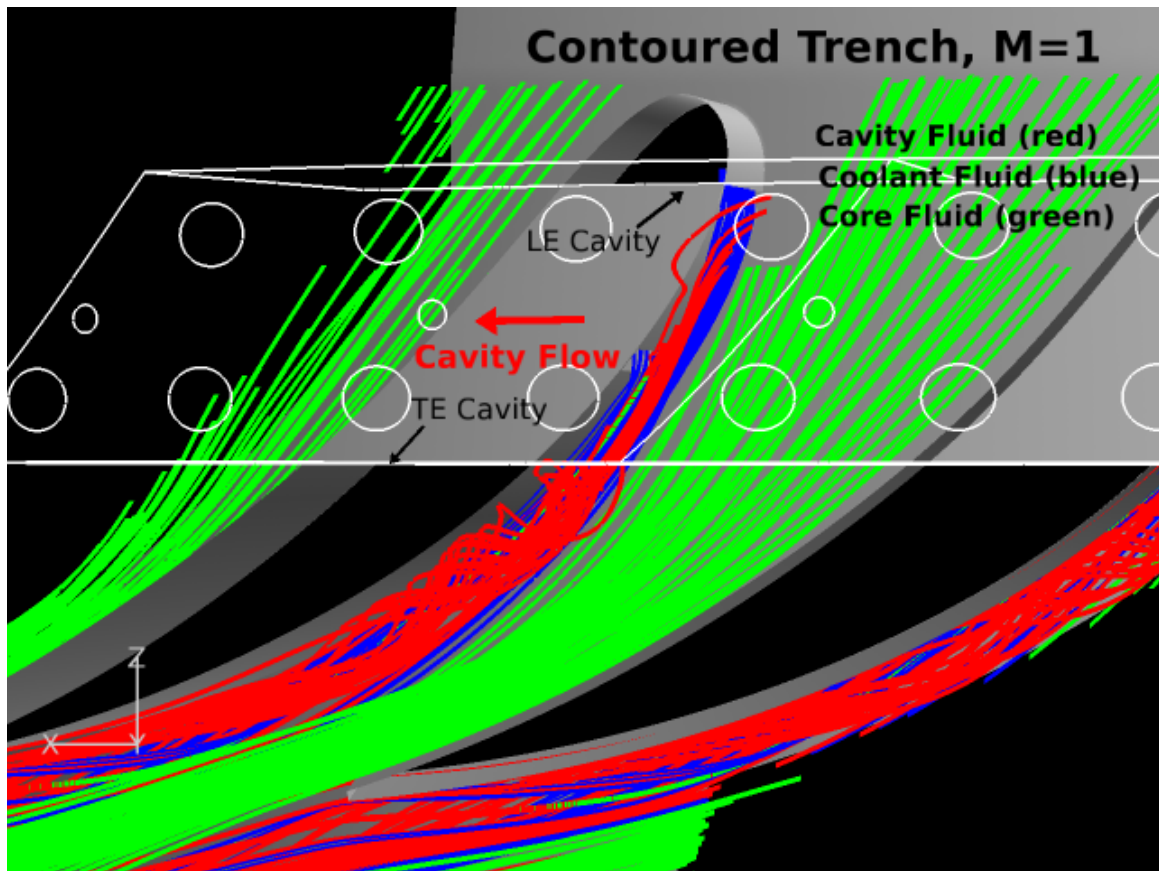


Figure B.2: Top down view of fluid interaction of cavity fluid (red streamline), coolant fluid (blue streamline) and core fluid (green streamline) for Contoured Trench design (M=1 test case)

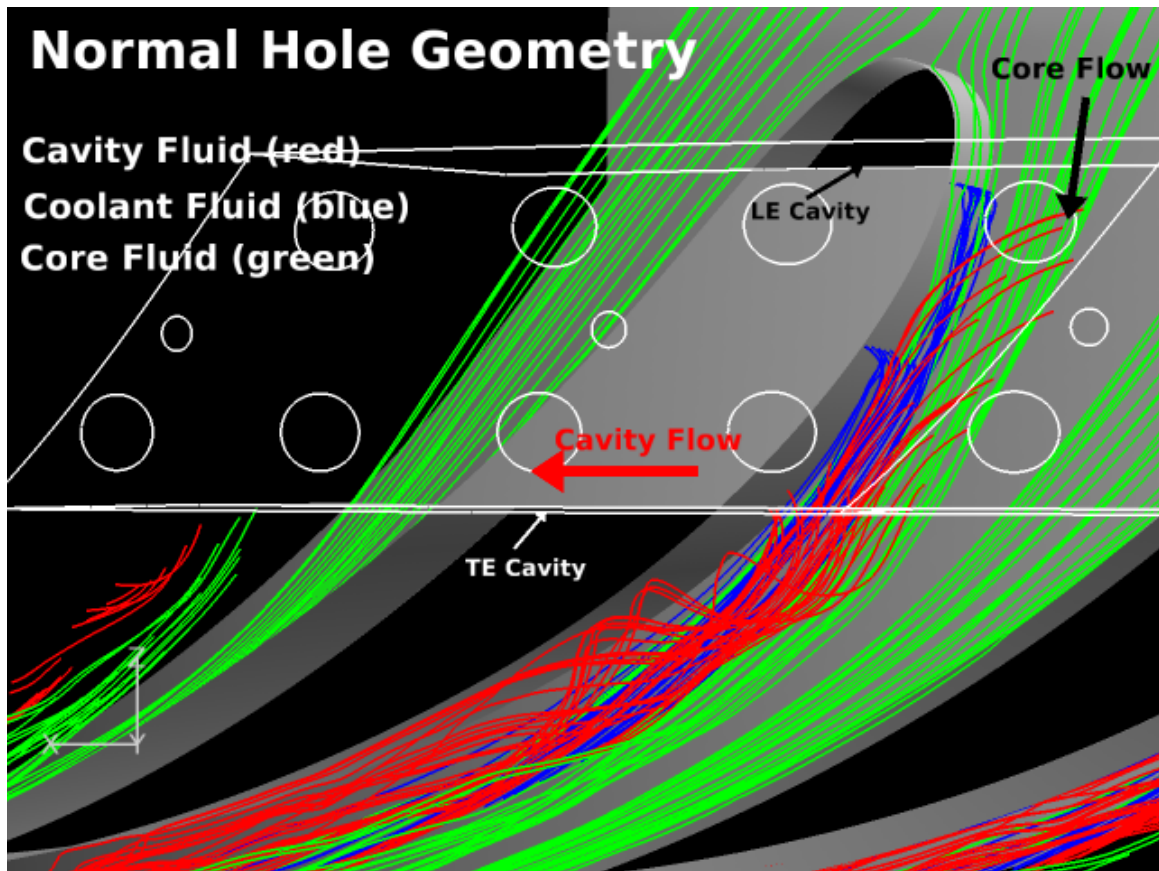


Figure B.3: Top down view of fluid interaction of cavity fluid (red streamline), coolant fluid (blue streamline) and core fluid (green streamline) for normal hole geometry design (M=1 test case)

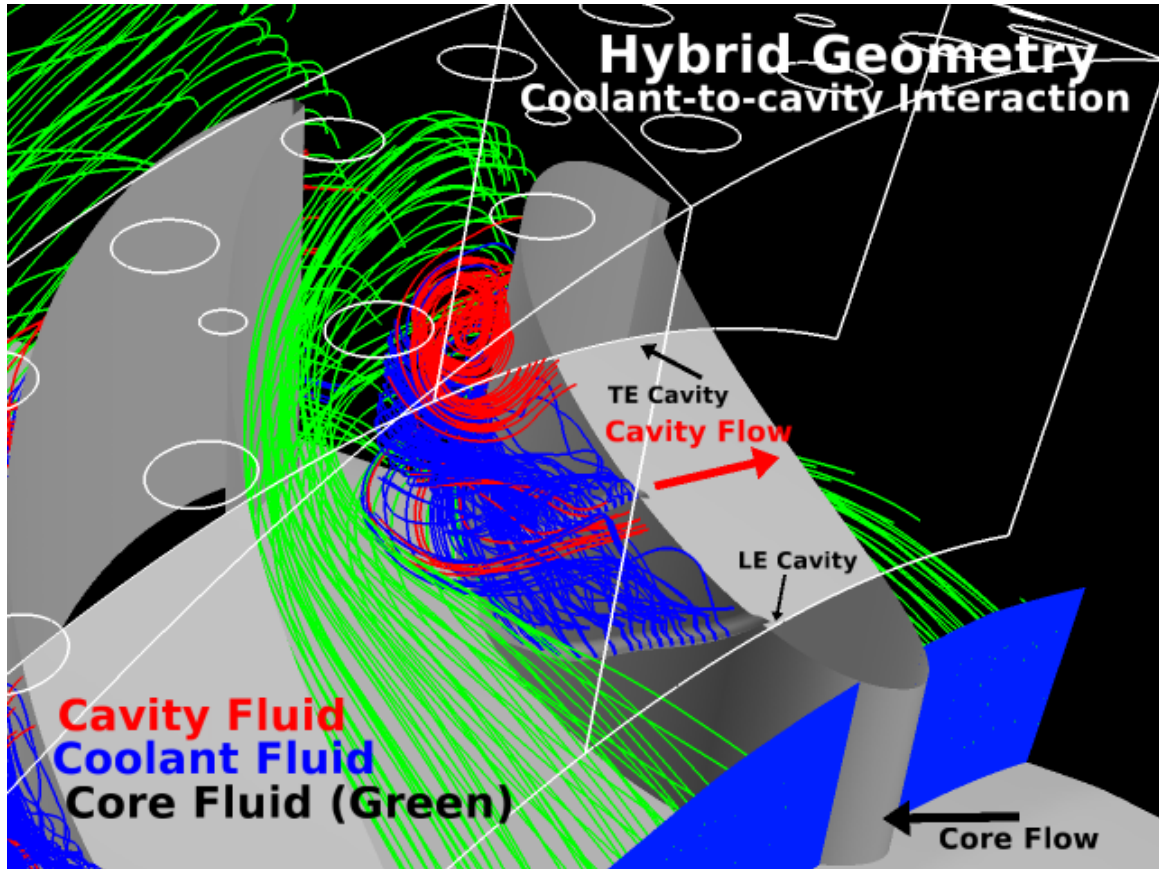


Figure B.4: Hybrid geometry fluid interaction of cavity fluid (red streamline), coolant fluid (blue streamline) and core fluid (green streamline) for $M=2$ test case

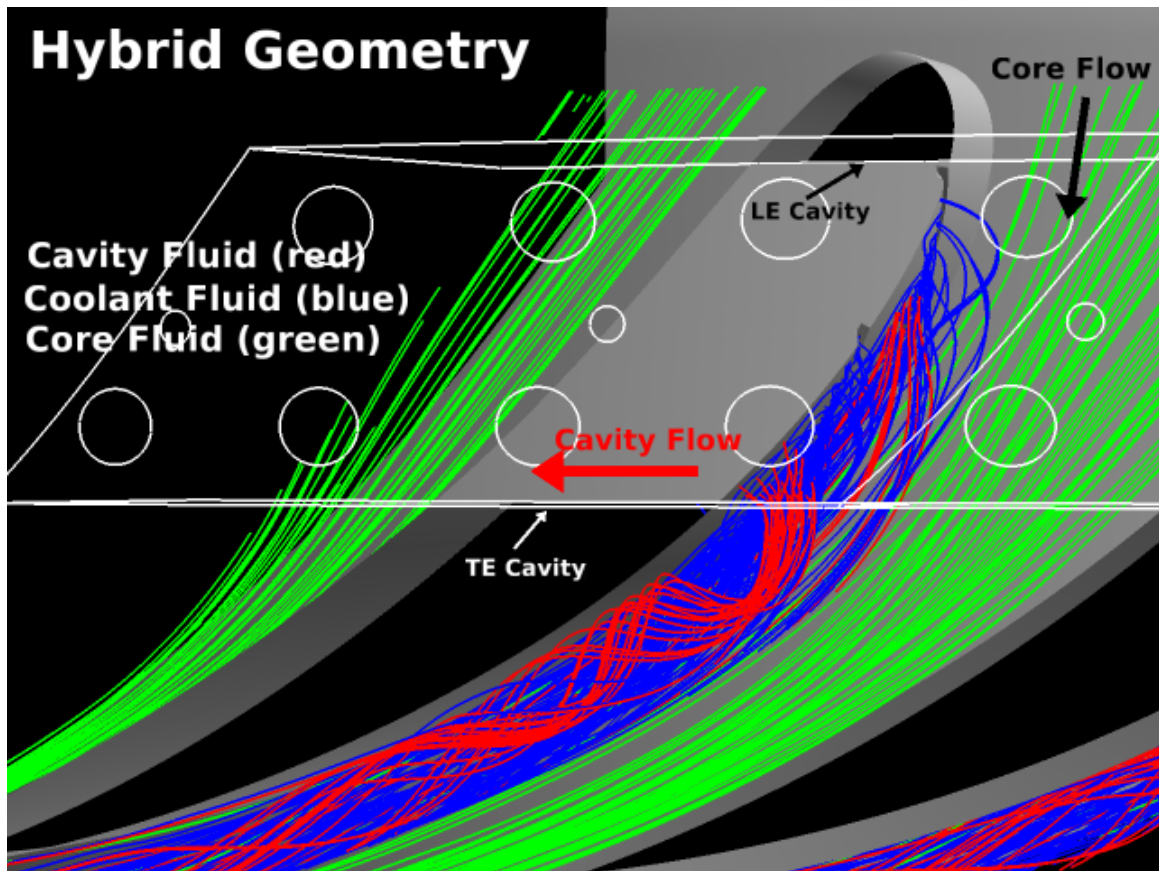


Figure B.5: Top down view of fluid interaction of cavity fluid (red streamline), coolant fluid (blue streamline) and core fluid (green streamline) for Hybrid geometry design (M=2 test case)

Bibliography

1. Anisko, Johnathan. *Numerical Investigation of Cavity-Vane Interactions within The Ultra Compact Combustor*. Master's thesis, Air Force Institute of Technology, Mar 2006.
2. Baldauf, S., M. Scheurlen, A. Schulz, and S. Wittig. "Correlation of Film-Cooling Effectiveness from Thermographic Measurements at Engine-like Conditions". *Journal of Turbomachinery*, 124:686–698, 2002.
3. Ballal, D.R. and J. Zelina. "Progress in AeroEngine Technology (1939-2003)". July 2003. AIAA-2003-4412.
4. Batell, Ryan. "Combustor Exit Discussion", September 2011. Personal Interview. September 2011.
5. Bogard, D.G. and K.A. Thole. "Gas Turbine Film Cooling". *Journal of Propulsion and Power*, December 2005.
6. Bohan, Brian T. *Analysis of Flow Migration in an Ultra-Compact Combustor*. Master's thesis, Air Force Institute of Technology, Mar 2011.
7. Bons, Jeffery, Charles MacArthur, and Richard Rivir. "The Effect of High Freestream Turbulence on Film-Cooling Effectiveness". *The American Society of Mechanical Engineers*, (94-GT-51), June 1994.
8. Bunker, R. S. "Film Cooling Effectiveness Due to Discrete Holes within a Transverse Surface Slot". *Proceedings of the 2002 IGTI Turbo Expo: International Gas Turbine Conference and Exposition*, June 2002.
9. Cohen, Henry, Gordon Frederick Crichton Rogers, and H. I. H. Saravanamuttoo. *Gas Turbine Theory*. Longman, 4th edition, 1996.
10. Dittmar, J., I. S. Jung, A. Schulz, S. Wittig, and J. S. Lee. "Film Cooling from Rows of Holes- Effect of Cooling Hole Shape and Row Arrangement on Adiabatic Effectiveness". *Annals of the New York Academy of Sciences*, 934:321–328, May 2001.
11. Evans, D. *The Impact of Heat Release in Turbine Film Cooling*. Master's thesis, The Air Force Institute of Technology, 2008.
12. Fluent[®] Inc. *ANSYS Fluent 13.0.0 Tutorial Guide*, Nov 2010.
13. Foster, N. W. and D. Lampard. "The Flow and Film Cooling Effectiveness Following Injection Through a Row of Holes". *Journal of Engineering for Power*, 102:584–588, 1980.
14. Goldstein, R., E. Eckert, V. Ericksen, and J. Ramsey. *Film Cooling Following Injection Through Inclined Circular Tubes*. Nasa cr-72612, November 1969.

15. Gritsch, M., A. Schulz, and S. Wittig. "Adiabatic Wall Effectiveness Measurements of Film-Cooling Holes With Expanded Exits". *AIAA Journal*, 1997. 97-GT-164.
16. Hartnett, J. P., R. C. Birkebak, and E. R. G. Eckert. "Velocity Distributions, Temperature Distributions, Effectiveness and Heat Transfer for Air Injected Through a Tangential Slot Into a Turbulent Boundary Layer". *Journal of Heat Transfer*, 293–306, 1961.
17. K. D. Lebay, M. D. Polanka and R. D. Branam. "Characterizing the Effect of Radial Vane Height on Flame Migration in an Ultra Compact Combustor". *Proceeding of the ASME Turbo Expo 2011*, (GT2011-459191), 2011.
18. Kirk, Daniel R. *Near-Wall Reaction Effects on Film-Cooled Surface Heat Transfer*. Master's thesis, Massachusetts Institute of Technology, Sep 2003.
19. Kohli, A. and D. Bogard. "Adiabatic Effectiveness, Thermal Fields, and Velocity Fields for Film Cooling with Large Angle Injection". *Journal of Turbomachinery*, 119:352–358, 1997.
20. Lewis, G. D. "Swirling FLOW Combustion - Fundamentals and Application". November 1973. AIAA 2003-4412.
21. Parks, Adam. *Desensitizing Flame Structure and Exhaust Emission to Flow Parameters in an Ultra-Compact Combustor*. Master's thesis, The Air Force Institute of Technology, Mar 2012.
22. Pedersen, D. R. *Effect of Density Ratio on Film Cooling Effectiveness for Injection Through a Row of Holes and for a Porous Slot*. Ph.D. thesis, University of Minnesota, Minneapolis, Minnesota, March 1972.
23. Pointwise[®] Inc. *Pointwise User Manual*, 2011.
24. Polanka, M. D., J. Zelina, W. Anderson, B. Sekar, D. Evans, C. X. Lin, and S. D. Stouffer. "Heat Release in Turbine Cooling I: Experimental and Computational Comparison of Three Geometries". *Journal of Propulsion and Power*, 27(2):257–268, Mar-Apr 2011.
25. Sinha, A. K., D. G. Bogard, and M. E. Crawford. "Film-Cooling Effectiveness Downstream of a Single Row of Holes With Variable Density Ratio". *Journal of Turbomachinery*, 113:442–450, July 1991.
26. Sirignano, W. A. and F. Liu. "Performance Increases for Gas-Turbine Engines Through Combustion Inside the Turbine". *Journal of Propulsion and Power*, 15(1), February 1999.
27. Thole, K. A., A. K. Sinha, D. G. Bogard, and M. E. Crawford. "Mean Temperature Measurements of Jets with a Crossflow for Gas Turbine Film Cooling Application". *Rotating Machinery Transport Phenomena*, 69–85, April 1992. ISORMAC-3.

28. Thornburg, H., B. Sekar, J. Zelina, and R. Greenwood. “Effect of Curved Radial Vane Cavity Arrangements on Predicted Inter-Turbine Burner (ITB) Performance”. *Proceedings of the 2007 DoD High Performance Computing Modernization Program Users Group Conference*, HPCMP-UGC '07, 110–119. IEEE Computer Society, Washington, DC, USA, 2007. ISBN 0-7695-3088-5. URL <http://dx.doi.org/10.1109/HPCMP-UGC.2007.29>.
29. Thornburg, H. J., B. Sekar, W. Anderson, M. Polanka, C. Lin, R. Holder, A. Briones, and D. Stouffer. “Design Studies of Turbine Blade Film Cooling With Unburned Fuel in Cross-Stream Flow”. HPC Insights, Fall 2009.
30. Wilson, Jacob. “2-D Heat Release Analysis of Ultra-Compact Combustor”, October 2011. Personal Interview. October 2011.
31. Zelina, J., G. J. Sturgess, and D. T. Shouse. “The Behavior of an Ultra-Compact Combustor (UCC) Based on Centrifugally-Enhanced Turbulent Burning Rates”. 2004. AIAA 2004-3541.

Vita

Captain Donald D. Johnson graduated from Captain Shreve High School in Shreveport, Louisiana. He entered undergraduate studies at Louisiana Tech University where he graduated with a Bachelor of Science degree in Mechanical Engineering in May 2007. He also commissioned into the Air Force through Air Force Reserve Officer Training Corps (ROTC) in May 2007.

He was assigned to the Materials and Manufacturing Directorate at Wright-Patterson AFB, OH. Materials and Manufacturing Directorate is part of the Air Force Research Laboratory. Duties at the Materials and Manufacturing Directorate included development and transition of low observable composite repair materials for the B-2 aircraft. In June 2009, he served as a executive officer to the deputy director of the Materials and Manufacturing Directorate.

In August of 2010 he entered the Graduate School of Engineering and Management at the Air Force Institute of Technology majoring in aeronautical engineering with concentrations in aerodynamics, rocket propulsion and computational fluid dynamics. Upon graduation he will be assigned to the 31st Test and Evaluation Squadron at Edwards AFB, CA.

Permanent address: 2950 Hobson Way
Air Force Institute of Technology
Wright-Patterson AFB, OH 45433

REPORT DOCUMENTATION PAGE			Form Approved OMB No. 0704-0188	
<p>The public reporting burden for this collection of information is estimated to average 1 hour per response, including the time for reviewing instructions, searching existing data sources, gathering and maintaining the data needed, and completing and reviewing the collection of information. Send comments regarding this burden estimate or any other aspect of this collection of information, including suggestions for reducing this burden to Department of Defense, Washington Headquarters Services, Directorate for Information Operations and Reports (0704-0188), 1215 Jefferson Davis Highway, Suite 1204, Arlington, VA 22202-4302. Respondents should be aware that notwithstanding any other provision of law, no person shall be subject to any penalty for failing to comply with a collection of information if it does not display a currently valid OMB control number. PLEASE DO NOT RETURN YOUR FORM TO THE ABOVE ADDRESS.</p>				
1. REPORT DATE (DD-MM-YYYY) 22-03-2012		2. REPORT TYPE Master's Thesis		3. DATES COVERED (From — To) 1 September 2011 – 22 March 2012
4. TITLE AND SUBTITLE Cooling Requirements for the Ultra-Compact Combustor			5a. CONTRACT NUMBER	
			5b. GRANT NUMBER	
			5c. PROGRAM ELEMENT NUMBER	
6. AUTHOR(S) Captain Donald D. Johnson, USAF			5d. PROJECT NUMBER	
			5e. TASK NUMBER	
			5f. WORK UNIT NUMBER	
7. PERFORMING ORGANIZATION NAME(S) AND ADDRESS(ES) Air Force Institute of Technology Graduate School of Engineering and Management (AFIT/ENY) 2950 Hobson Way WPAFB OH 45433-7765			8. PERFORMING ORGANIZATION REPORT NUMBER AFIT/GAE/ENY/12-M25	
9. SPONSORING / MONITORING AGENCY NAME(S) AND ADDRESS(ES) Air Force Research Laboratory Propulsion Directorate, Combustion Branch 1950 Fifth Street, Building 490 WPAFB OH 45433-7251 POC: Dr. Joseph Zelina, Phone: 937-255-7487, Email: joseph.zelina@wpafb.af.mil			10. SPONSOR/MONITOR'S ACRONYM(S) AFRL	
			11. SPONSOR/MONITOR'S REPORT NUMBER(S)	
12. DISTRIBUTION / AVAILABILITY STATEMENT APPROVED FOR PUBLIC RELEASE; DISTRIBUTION UNLIMITED				
13. SUPPLEMENTARY NOTES This material is declared a work of the U.S. Government and is not subject to copyright protection in the United States.				
14. ABSTRACT Over the past several years, AFIT and the Air Force Research Laboratory have collaboratively investigated a novel combustor system that is compact in design and could be potentially used an inter-turbine burner system. The UCC attempts to wrap the combustion section circumferentially around the axial core flow and exploits the use of high-g combustion. As a result, the combustor volume and weight is reduced by integrating of the exit compressor vane and the turbine inlet vane. This creates a new 'hybrid' vane that resides directly below the circumferential combustor. Most recently, a computational effort on understanding the fundamentals aspects of the UCC on a fighter-sized scale model reveal that high temperatures are predicted to occur on the hybrid vane. To address this issue, film-cooling application is being explored in the UCC in a computational manner. The application of normal coolant hole, contoured trench, and hybrid normal and contoured trench configurations were investigated for a blowing ratio of M=1, 1.5 and 2. Of the blowing ratios studied, secondary reactions form due to the oxygen-rich coolant air reacting with unburned fuel as it exits the circumferential cavity. Although these reactions do occur, a decrease in unburned radicals is noticed at the exit of the UCC due to enhanced completion of reactions upstream.				
15. SUBJECT TERMS Jet engines, ultra-compact combustor, film-cooling, inter-turbine burner, turbine engine				
16. SECURITY CLASSIFICATION OF:			17. LIMITATION OF ABSTRACT UU	18. NUMBER OF PAGES 138
a. REPORT U	b. ABSTRACT U	c. THIS PAGE U		
			19a. NAME OF RESPONSIBLE PERSON Dr. Marc Polanka	
			19b. TELEPHONE NUMBER (Include Area Code) (937)255-3636, ext 4714 Email: marc.polanka@afit.edu	